

ENERGY AND PARTICLE TECHNOLOGY GROUP

RESEARCH GROUP AT MECHANICAL ENGINEERING DEPARTMENT
CARLETON UNIVERSITY

Designing a Common Platform for Modelling Soot in Flames and Reactors

Supervisor: Dr. Reza Kholghy

Author:

Mo ADIB
Carleton University
mo.adib@carleton.ca

Reviewer:

Reza KHOLGHY
reza.kholghy@carleton.ca

Disclaimer: This is a student progress work, done as part of a research assistantship. Any reader should be aware that it might not be free of errors. Still, it might be useful for someone who would like learn some details similar to the ones presented in the report and in the accompanying files.

The material has gone through a review process by group's supervisor.

Last time updated on:

May 24, 2024

Contents

1	Introduction	5
1.1	Motivation	5
1.2	Background	6
1.2.1	Soot inception and surface growth	6
1.3	Coagulation and agglomeration	9
1.4	Soot maturity and its optical properties	11
1.5	Oxidation	12
1.6	Research objectives	12
2	Theoretical Model	14
2.1	Assumptions and conventions	14
2.2	Flames	15
2.3	Reactors	16
2.3.1	Constant Volume Reactor	16
2.3.2	Perfectly Stirred Reactor	17
2.3.3	Plug Flow Reactor	18
2.4	Particle Dynamics	19
2.4.1	Soot Morphology	19
2.4.2	Diffusion of soot particles	21
2.4.3	Soot Composition	21
2.4.4	Monodisperse Population Balance Model	22
2.4.4.1	Coagulation	22
2.4.4.2	Source terms	22
2.4.5	Sectional Population Balance Model	23
2.4.5.1	Coagulation	23
2.4.5.2	Source terms	25
2.5	Surface reactions model	26
2.6	PAH growth models	28
2.6.1	Irreversible Dimerization	29
2.6.2	Reactive Dimerization	30
2.6.3	Dimer Coalescence	32
2.6.4	E-Bridge Formation	34
2.7	Gas scrubbing rates	36
3	Results	37
3.1	Validation	37
3.1.1	Collision Frequency	37
3.1.2	Coagulation	38
3.1.3	Constant Volume Reactor	38
3.1.4	Plug Flow Reactor	40
3.2	Soot yield and morphology during methane pyrolysis in shock-tubes	40
3.2.1	Experimental setup and data collection	43

3.2.2	Analysis of soot morphology in methane pyrolysis shock-tube	50
3.2.3	Sensitivity of yield and morphology to inception and surface growth rate	53
A	Derivation of Transport Equations	68
A.1	Constant Volume Reactor	68
A.1.1	Continuity	68
A.1.2	Species	68
A.1.3	Energy	69
A.1.4	Soot Variables	70
A.2	Plug Flow Reactor	71
A.2.1	Continuity	71
A.2.2	Momentum	71
A.2.3	Species	72
A.2.4	Energy	72
A.3	Perfectly Stirred Reactor	73
A.3.1	Continuity	73
A.3.2	Species	74
A.3.3	Energy	74
B	Appendix: Additional Results	77
B.1	Methane pyrolysis data from Hanson Research Group	77
B.1.1	30% CH ₄ dataset	77
B.2	Methane pyrolysis data of Agafonov et al. [1]	78

Nomenclature

Acronyms

CFD	Computational Fluid Dynamics
DEM	Discrete Element Modelling
HACA	Hydrogen abstraction carbon addition
MPBM	Monodisperse Population Balance Model
SPBM	Sectional Population Balance Model

Constants

Av	Avogadro's number	$6.02214076 \times 10^{23}$	1/mol
k_B	Boltzmann constant	$1.3806488 \times 10^{-23}$	$\text{m}^2\text{kg/s}^2\text{-K}$

English symbols

C_{tot}	Totla carbon content of soot particles (per section)	mol/kg
D	Diffusion coefficient of particles	m^2/s
d	diameter	m
d_c	Collision diameter	m
d_g	Gyration diameter	m
d_m	Mobility diameter	m
d_p	Primary particle diameter	m
H_{tot}	Totla hydrogen content of soot particles (per section)	mol/kg
I	Source terms for soot variables	$\text{mol}/(\text{kg} \cdot \text{s})$
k	reaction rate constant	$\text{m}^3/(\text{mol} \cdot \text{s})$
m	mass	kg
n_p	Number of primary particles of per agglomerate	
N_{agg}	Number density of agglomerates	mol/kg
N_{pri}	Number density of primary particles	mol/kg
SF	Sectional spacing factor	—
T	Temperature	K
W	Molecular weight	kg

Greek symbols

β	Collision frequency	m^3/s
δ_a	Mean distance of particles	m
λ	Mean free path	m
λ_a	Mean stopping distance of particles	m
ν	Gas kinematic viscosity	m^2/s
ρ	Gas density	kg/m^3
ρ_{soot}	Soot density	kg/m^3
φ	Soot volume fraction	m^3/m^3

Subscripts

ads	Adsorption
agg	Agglomerate
coag	Coagulation
cont	Continuum
f	forward
fm	Free molecular
g	Gyration
grow	Surface growth
inc	Inception
m	Mobility
ox	Oxidation
pri	Primary particle
r	reverse
reac	reactive

Chapter 1

Introduction

1.1 Motivation

Carbonaceous nanoparticles, such as Carbon Black (CB) and soot, are widely encountered in nature and engineering. Every year, nearly 9.5 megatons of soot (black carbon) is emitted into the atmosphere from anthropogenic activities and natural sources such as wildfires and volcanoes [2]. The wide light absorption range of soot reduces the albedo of snow-covered area and alters the radiative forcing balance in the atmosphere making soot the third strongest contributor to climate change after methane and carbon dioxide [2]. Also, exposure to combustion-generated soot could promote respiratory and cardiovascular disease [3]. So, strict regulations are targeting combustion engines to limit environmental and health risks from soot formation [4]. Accurate and affordable models are essential for the prediction of soot composition and morphology in combustion devices and help to reduce the emissions in engines. They can also provide better understanding of soot optical properties that are major indicator of soot environmental effects.

On the other hand, CB with a similar synthesis process and structure to soot but higher elemental carbon to hydrogen ratios (>97%) [5] is commercially produced and sold in large scales. In fact, CB is the largest industrially produced nanomaterial by value and volume (~15 megatons per year with a value of \$17B) with applications as a reinforcing agent in rubber and tire industries [6] and conductive additive in lithium-ion batteries [7]. CB is primarily manufactured by the so-called furnace process where about 50% of heavy fuel oil is partially combusted to convert the rest of it into CB [8]. This process suffers from low mass yield and excessive emission, generating 4 tons of CO₂ per each ton of product on average [9]. Plasma reactor is an emerging alternative production method with distinct advantages over flame-based methods: They can achieve 100% carbon yields with no direct CO₂ emission or other pollutants [10], and the energy required for pyrolysis is supplied by an electric arc that does not depend on the feedstock composition. Controlling CB properties such as its specific surface area (or primary particle diameter), hard agglomerate size (or gyration diameter of agglomerates with primary particles connected to each other by strong chemical bonds), and composition (or particle carbon to hydrogen ratio) is important to make process economical and to achieve specific grades of CB for different target applications. However, this is a challenging task because of the complexity of CB formation and mass growth processes and its coupling with gas phase chemistry, dependence on local temperature and pressure. This requires accurate process design and optimization tools that provides insight into CB formation and evolution process, and inform manufacturer's decisions to adjust to produce CB with desired grades [11].

The term "soot" usually refers to unwanted particulate matter formed during incomplete combustion of any carbon-containing material from jet and diesel fuel to wood, heavy oil, and plastics with variable organic content and large H/C ratios [5], but this research focuses on soot particles generated under controlled laboratory conditions from fuels with known compositions. The mature soot formed in methane and ethylene premixed flame can reach 95% elemental C/H ratio [12], which is close to CB composition. The comparison of transmission electron microscopy (TEM) images of industrially produced CB [13] with soot sampled from diesel fuel [14, 15] shown in Fig.1.1 indicates that the two types of soot have similar morphologies.

cates similarity of their morphology and structure. Hereafter, soot is used to describe carbonaceous nanoparticle produced in flame/reactor during combustion/pyrolysis.

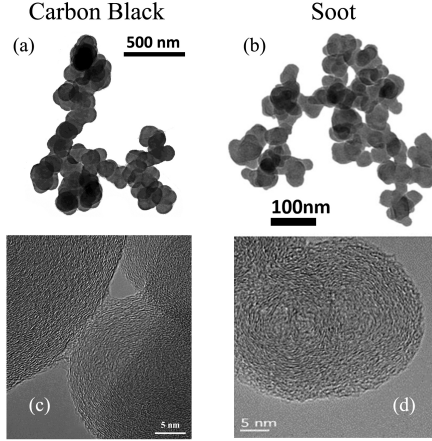


Figure 1.1: The TEM images of Carbon black (a & c) [13] and soot (b & d) [14, 15] that shows soot and CB has similar morphology and structure

1.2 Background

1.2.1 Soot inception and surface growth

The physics of soot formation involves concurrent processes with different time and length scales starting from the breakdown of hydrocarbon molecules to intermediate species and radicals that transition to first soot particles and grow via heterogeneous reactions on the surface as well as coagulation [16]. The TEM analysis of soot sampled from flames [15], reactors [17], and engines [18] with different fuels and process conditions revealed a common fractal-like morphology characterized as agglomerates of spheroidal primary particles. High resolution transmission electron microscopy (HRTEM) revealed cluster of precondensed Polycyclic Aromatic Hydrocarbons (PAHs), such as benzene, naphthalene and pyrene, in organized graphitic shell and disoriented core layers cluster soot primary particles [19]. Moreover, PAHs can resist dissociation under high flame temperatures due to the thermodynamic stability [20] supporting the widely accepted hypothesis that PAH are the main soot precursors.

However, the transition PAHs (soot precursors) to incipient soot, known *soot inception* has not been well understood at the level of pathways and elementary reactions [21] primarily due to uncertainties in PAH (precursor) chemistry. The thermodynamics of PAH growth from acetylene (C_2H_2) as the dominant hydrocarbon species in fuel pyrolysis and an intermediate of molecular growth does not experience a significant enthalpy release or entropy increase, so the path is driven by a gradual reduction in Gibbs free energy. As a result, the kinetics of PAH growth into subsequent soot particles can be highly reversible hence sensitive to local temperature, pressure and intermediate species concentration.

The growth of PAHs beyond first ring (benzene) is predominantly driven by so-called hydrogen abstraction carbon (acetylene) addition (HACA) mechanism [22] where a hydrogen radical abstracts an hydrogen atom at the edge of PAH, providing a reactive site for acetylene addition. The kinetic reversibility of HACA opens the door for competing pathways such as chain reactions of resonance-stabilized radical (RSR). Propargyl is a prominent example of these radicals, whose combination is known as a major contributor to benzene formation [23]. Built on this hypothesis, Johansson et al. [24] proposed a radical-driven growth mechanism by addition of vinyl (C_2H_3) starting from cyclopentadienyl (C_5H_5) to larger hydrocarbon radicals that can survive long enough in high temperatures to react with other radicals, PAHs and unsaturated aliphatic species, through radical

chain reactions. However, low concentrations of these radicals limit the growth rate through RSR pathways [25]. Moreover, some of the intermediate steps for radical regeneration such as formation of vinylcyclopentadienyl were shown to be kinetically unfavorable [25] compared to HACA. Regardless of their mechanistics, these sequential growth mechanisms, termed as *chemical growth* cannot account for rapid soot formation [22] and its nanostructure [26].

There is abundant but mostly indirect experimental and computational evidence pointing to a collision-based mechanism for soot inception. HRTEM images of nascent and mature soot shows a disordered PAH clusters highlighting the role of PAH collisions. The bimodality of particle size distribution (PSD) of nascent soot particles in premixed flames [27] indicates that the kinetics of inception is second order in precursor concentration [28]. The time-of-flight mass spectrometry (TOFMS) experiments in a 13 kPa acetylene-oxygen flame showed a series of peaks with a periodicity of 500 amu [29]. However, it is not how PAH clusters form and what force allows the binding occur and resist dissociation at the flames temperature (≥ 1600 T). Frenklach [22] characterized the clustering as a physical process where the sticking of PAHs upon collision forms dimer held together by Van der Waals forces without involving chemical reactions. In fact, Herdman and Miller [30] found that the binding energy of PAHs dimers due to dispersive and electrostatic forces increases linearly with molecular mass and reaches the limit of exfoliation energy for graphite. However, the entropy barrier of dimerization increases with PAH size making them unfavorable under equilibrium conditions. So, PAHs as large as circumcoronene ($C_{54}H_{18}$) can only form dimer to survive flame temperatures [21]. However, the concentration of large PAHs are too low to account for the observed number density of soot particles in flames [31]. PAH clustering can also be governed by non-equilibrium kinetics. PAH molecules can for rovibrationally excited dimer with long enough life time [32] to react with H atoms forming covalent bonds. There is also possibility for these clusters to joined by aliphatic linkages. Micro-FT-IR spectroscopy analysis by Cain et al. [33] showed the ratio of aliphatic-to-aromatic C–H bonds can exceed unity at flame temperature. Using these findings, they suggested that the aliphatic components in the form of alkyl, alkenyl can covalently bound to aromatic units in soot particles. Although such a mechanism is viable near the flame region, it cannot explain persistent soot inception in the post flame zone [34] where the H atom concentration is too low to initiate H abstraction reactions that produce those radicals.

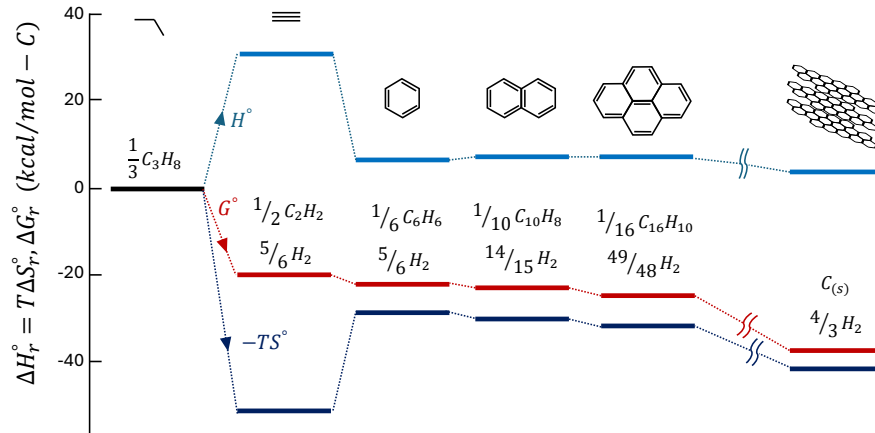


Figure 1.2: Standard enthalpy (ΔH) and entropy ($T\Delta S$) contributions to Gibbs function of reaction ΔF at 1600 K for carbon formation from propane(reprinted from ref. [21])

There are other complicating factors that hinders the fundamental understanding of soot inception such as lack of a decisive criterion to distinguish gaseous molecules from particles [16], and the overlap of inception with surface growth and agglomeration [35]. Measurement techniques have limited capability in soot detection due to short time and length scales of soot inception and surface growth ranging from pico- to milliseconds and micro- to millimeter [36]. Fig.1.3 demonstrates the length and time scales relevant to different stages of soot formation from PAH precursors to incip-

ient, nascent and mature soot in flames. Moreover, the collected data from measurements might not be **the true representative** of soot formed at the probed location of the studied process. For example, intrusive diagnostic methods based on thermophoresis or dilution have a sampling probe that can perturb flow dynamics or alter structure and composition of soot [37]. Non-intrusive techniques such as optical methods also rely on assumptions about light absorption and scattering of soot [38] and its morphology [39]. Despite the gaps in fundamental understanding of soot formation and limitations of diagnostics methods, models have been developed describe the soot inception and growth. These models have been formulated as a set of clear pathways that explain soot inception based on collisions of PAH molecules. They have to be consistent with current knowledge of soot physics, feasible to be coupled with chemistry and particle dynamics models, and able to predict soot mass, PSD and morphology observed in flames and reactors.

Soot inception was originally described as **PAH dimerization** where collision of two PAH molecules (monomers in this context) forms a dimer held together by Van der Waals forces [40]. The dimerization is a irreversible process with a efficiency that accounts for the reversibility or dissociation of dimers. The theory postulates that PAH growth continues by sequential addition of a monomer (PAH molecule) forming stacks of dimers, trimers, tetramers and so on to reach a certain mass threshold that marks the emergence of incipient soot [40], but for practical purposes, a dimer is usually considered as incipient soot. Here, we call this model *Irreversible Dimerization*. Irreversible Dimerization has been used to predict soot formation in burner-stabilized premixed [41, 42], counterflow diffusion flames [43, 44], coflow diffusion flames [45, 46]. A collision efficiency factor ranging between 10^{-6} to 1 is also employed to adjust the inception flux and PAH adsorption rates to achieve desired soot mass and size distribution. PAHs of moderate sizes such as pyrene (4 rings) to coronene (7 rings) have been considered as the starting point of inception due to their thermodynamic instability that justifies the irreversibility at high temperatures [40]. ~~Blancourt and Pitsch [47] introduced a two step~~ However, the theoretical calculations [48] and experiments [49] indicated that pyrene dimerization is highly reversible in **flame condition**.

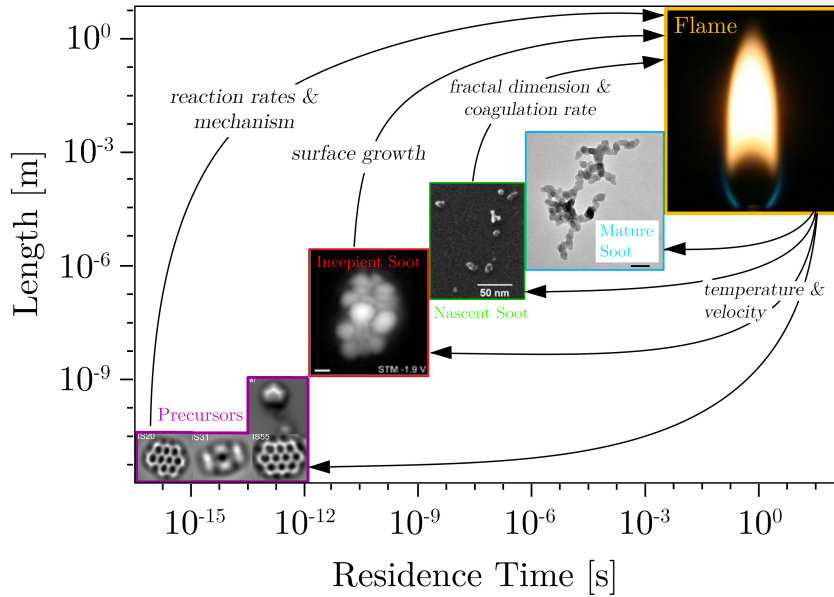


Figure 1.3: The range of time and length scales of the processes involved in soot formation from molecular reactions to particle-fluid interaction in flames

The inception rate of irreversible dimerization is mainly controlled by PAH concentration due to weak temperature dependence, so it produces new particles **in** low temperatures (even less than 500 K) [50] despite experimental evidence for termination of inception below 1200 K [51, 52]. Also, the arbitrary selection of efficiency factors alters the distribution of mass between inception of surface

growth could significantly change soot mass, PSD, and morphology **strongly** [53]. Miller [54] used equilibrium constant for PAH dimerization to calculate the net dimerization rate and demonstrated that the collision of PAHs larger than circumovalene (~ 800 amu) could last long enough to grow into incipient soot. However, the concentration of PAHs drops rapidly with size [21]. The entropy barrier of dimerization is significant for larger PAHs [55].

Eaves et al. [56] relaxed the irreversibility assumption, and developed a reversible clustering model to simulate inception using an array of PAHs from naphthalene to benzo-pyrene. Building on that work, Kholghy et al. [57] emphasized on the necessity of chemical bond formation after physical PAH clustering for accurate prediction of volume fraction, primary particle diameter and PSD in ethylene coflow diffusion flames. Later, Kholghy et al. [58] proposed the "*Reactive Dimerization*" model which starts with reversible collision of PAHs leading to physical dimers held with vdW forces that are graphitized and form chemically-bonded **dimer** that serve as soot nuclei grow via surface reactions. They also performed a systematic analysis on contribution of different PAHs, and concluded that one- and two-ring aromatics account for almost all of inception flux in the so-called "*sooting flame*" [42]. However, Frenklach and Mebel [25] pointed out that an inception model that initiated with a highly reversible step similar to Reactive Dimerization [58] cannot produce sufficient flux of particles to match measurements of the benchmark burner-stabilized stagnation flame [28]. Instead, they proposed a HACA-driven mechanism where addition of monomer molecule to its radical activated by hydrogen abstraction for a stable dimer via an E-Bridge bond formation, and this sequential process continues to form trimers, tetramers, and larger PAH clusters.

The gas-phase chemistry of aromatics can be extended to account for chemical growth of incipient soot via surface reactions [22]. This hypothesis, known as "chemical similarity" postulates that the reactions occurring on the soot surface are similar to those involving large molecules of PAHs in the gas phase. It also provides means to describe the rates of surface growth and particle oxidation in terms of elementary chemical reactions. In other words, it is assumed that the surface of soot particles is made up of lateral faces of large PAHs covered with C-H bonds. This is the basis for the hydrogen-abstraction-acetylene-addition (HACA) mechanism [40, 59] that assumes the soot surface to consist of hydrogenated sites with a predefined density. Mass growth on soot surface requires H-abstraction to form a radical site, followed by acetylene attack similar to growth of PAH molecules in the gas-phase. The reactivity of these sites changes with time and temperature [60, 61], described as soot aging. **Fr** modelling purposes, a temperature-dependent multiplier, usually represented by α , was introduced to account for these **effect**. Appel et al. [59] showed α changes with temperature and particle size. ~~However, soot mass growth without the presence of H radicals [62] indicated the incompleteness of the HACA mechanism to describe the entire process of soot surface growth.~~

Adsorption of PAHs on the surface of soot particles is also a viable growth mechanism [40], more specifically called physisorption or chemisorption depending on the mechanisms driving the adsorption process [63]. There is still debate over the stability of adsorbed PAH molecules on soot surface [64]. Following the hypothesis that PAHs are building blocks of soot particles, a mechanism similar to inception is often used to describe PAH-soot growth.

1.3 Coagulation and agglomeration

In typical soot formation processes such as flames and reactor, soot particles are formed at high concentrations (10^{12} 1/cm³), and inception and surface growth are relatively short compared to the total residence of soot particles. As a result, coagulation becomes dominant rapidly attaining both [65] self-preserving size distribution (SPSD) [66] and asymptotic fractal-like structure [67]. The evolving fractal-like structure of agglomerates quantified by their mobility diameter normalized by primary particle, d_m/d_p , and gyration, d_m/d_g , diameters can be described with power laws derived from mesoscale simulations [68]. The collision frequency of agglomerates depends on their evolving fractal-like morphology. Also, polydisperse agglomerates collide more frequently than monodisperse ones. The enhancement in their collision frequency reaches an asymptotic value of 35% [65] or 82% [69] in the free molecular or transition regimes, respectively at SPSD regardless of the polydispersity in their constituent primary particles. Particle morphology formed by inception, surface

growth and agglomeration can be tracked precisely by mesoscale simulations, such as Discrete Element Modeling (DEM) [70]. However, they are computationally expensive and interfacing them with chemical kinetics in computational fluid dynamics (CFD) simulations is not trivial [71]. This limits their application. So, sectional population balance models (SPBM) are often used to track agglomerate and primary particle size distribution [72], morphology [73], and composition [45] in complex laminar [45] and turbulent flows [74]. Using the SPBMs coupled with relations for agglomerate fractal-like structure [75] and collision frequency [36], particle size distribution, morphology and composition can be tracked accurately. However, the computational cost of SPBMs increases exponentially with the number of sections [31] and particle properties [45] tracked. Thus, one property (e.g. agglomerate mass) is typically tracked with SPBMs to reduce computational cost. This does not allow to account for agglomerate fractal-like structure [76, 77] which limits SPBM accuracy in predicting surface growth and coagulation rate of agglomerates and their size distribution.

Alternatively, particle dynamics can be tracked by the method of moments (MOM) [78] or monodisperse population balance models (MPBM) [79]. Such models only track average particle properties (e.g. moment ratios) and their accuracy could be limited if unrealistic assumptions (e.g. approximating agglomerates as monodisperse and perfect spheres) are used. However, when inception and surface growth are short [80] and high particle (number) concentrations are formed [68], they lead to rapid attainment of self-preserving size distributions (SPSD) and agglomerates having asymptotic structure [65]. In this case a MPBM or MOM can be assembled on a firm scientific basis with accuracy on par with DEM [70], SPBM [81] and experimental data [82, 83, 84]. Such models can be readily interfaced with CFD simulations [85] without significant computational cost, making them ideal for three-dimensional and even turbulent flame simulations.

The MOM tracks moments of the PSD and estimates average particle properties such as mass [86], surface area [87], the number of constituent primary particles per agglomerate, n_p [78], or even particle composition [47] using the ratio of the moments. The MOM with four equations was used to describe synthesis of optical fibers by simultaneous reaction, diffusion, coagulation and thermophoresis of SiO_2 in laminar flow reactors assuming a lognormal PSD [88]. The MOM with interpolative closure (MOMIC) was developed to predict simultaneous nucleation, surface growth and coagulation of soot agglomerates and estimate its PSD with six equations [78]. To calculate source terms of the transported moments, additional moments that are not tracked are needed preventing the closure of the system of differential equations with the MOM [86, 89]. Thus, often the PSD shape is assumed a priori [86] or extra equations are solved to estimate it [79].

The MPBMs do not have the closure problem and calculate average particle properties by tracking their total concentration, mass [79] and area [90, 91]. Kruis et al. [79] used a 2-equation MPBM (known as the semi-empirical model) to track soot concentration and mass in (non-premixed) flames assuming spherical particles. Good agreement was achieved for measured soot mass. However, the specific surface area [91] and coagulation frequency of spheres are significantly smaller compared to that of agglomerates with the same mass underestimating their oxidation rate [81] and overestimating their concentration [40]. Kruis et al. [79] proposed a 3-equation MPBM to account for the fractal-like structure of nanoparticle agglomerates during coagulation and sintering. Agglomerate volume and area were used to obtain their equivalent primary particle diameter, d_p , and n_p . Then, agglomerate collision diameter, i.e. d_g , was calculated by D_f , d_p and n_p to account for their fractal-like structure that affects their collision frequency. Tsantilis and Pratsinis [90] extended the MPBM to predict hard-(chemically-bonded) and soft- (physically-bonded) agglomerates during synthesis of SiO_2 and TiO_2 [92] nanoparticles with simultaneous reaction, surface growth, coagulation and sintering. Such a MPBM applies best at high concentrations when inception and surface growth are short [80] resulting in the dominance of coagulation where particles rapidly reach their SPSD and asymptotic fractal-like structure. This is often the case for soot emitted from a variety of combustion devices or CB reactors where inception and surface growth are limited to only a few milliseconds when temperature is very high (i.e. $T \geq 1500\text{K}$) [58].

1.4 Soot maturity and its optical properties

The maturity level of soot is described as the evolution of physical and chemical properties from incipient to graphite-like mature soot [93]. It involves the growth of the graphitic crystallite fine structure of soot within, and perpendicular to, the aromatic layers. [94, 95], known as graphitization, followed by increase in the size of the crystallite-layer planes and decrease of the interlayer spacing [19]. This process is accompanied by the pyrolytic conversion of hydrocarbon species and substituted hydrocarbons toward elemental carbon and increase in the carbon-to-hydrogen (C/H) ratio, known as carbonization. Soot maturity is closely associated with reactivity of surface sites. At early stages of formation, soot surface is considerably more reactive than that of mature graphitized mature soot [96]. Fig.1.4 compares nanostructure of nascent soot composed of disoriented PAH clusters with that of mature soot with a core-shell pattern where disordered core is surrounded by concentrically oriented graphitic layers [29]. The core-shell nanostructure of mature soot strongly depends on process conditions such as pressure, fuel identity, temperature and residence time of the particles.

Evolution of soot maturity and morphology impacts its optical properties. Incipient and nascent soot absorb shorter wave lengths ($\lambda \leq 600 \mu\text{m}$) as opposed to mature soot particles that are broad-band light absorbers [97]. Non-intrusive optical diagnostic methods such as light extinction (absorption and scattering) [98] and Laser Induced Incandescence (LII) [38] are widely utilized to measure soot volume fraction, f_v using extinction coefficient and the absorption function, $E(m)$ that depends on soot refractive index, m , soot composition and morphology [99].

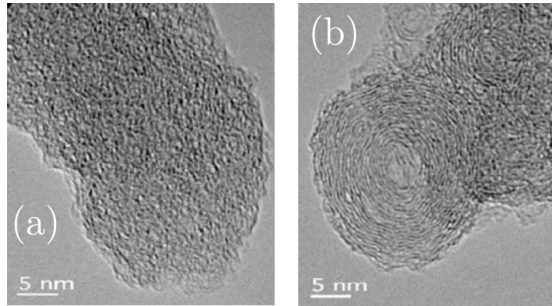


Figure 1.4: The HRTEM image of (a) a nascent soot primary particle with disordered internal nanostructure juxtaposed with that of (b) a mature soot primary particle with well-organized cluster near the shell sampled from soot generated by pyrolysis of ethanol at 1250 and 1650, respectively. Reprinted from Ref.[100]

However, the effects of soot composition, and morphology on its m , and $E(m)$ are not fully understood yet. $E(m)$ of soot at $\lambda = 1064 \text{ nm}$ measured by two-color LII measurements increases from 0.193 to 0.349, and 0.226 to 0.340 for ethylene premixed flames with equivalence ratio of $\phi=2.1$ and $\phi=2.3$, respectively when height above burner (HAB) changes from 8 to 14 mm [101]. During acetylene pyrolysis in a shock tube, $E(m)$ of soot particles increases from 0.05 to 0.25 as their primary particle diameter, d_p , grows to 20 nm within 1.6 ms [102]. Using m and $E(m)$ of mature spherical soot [103] at different HABs neglecting the impact of soot morphology and composition on m [104] can overestimate soot volume fraction by 100% [105]. So, accurate estimation of the evolving optical properties of soot is essential to close the carbon mass balance in the measurements [105], and analyze reaction kinetics for soot inception [58] surface growth [59] and oxidation [106] that are essential for development and validation of aerosol dynamics models coupled with chemistry to predict soot formation.

The dependence of soot m on its morphology and composition can be quantified by soot optical band gap, E_g [107]. The optical band gap concept was originally proposed by Tauc et al. [108] for semi-conductors and later developed for amorphous carbon [109], and it can be used to describe the crystalline character of PAH clusters in soot [109]. Incipient flame-made soot with diameters less than 20 nm exhibit quantum dot behavior [110] with $0.7 < E_g < 2 \text{ eV}$ that is larger than E_g of graphitized

soot, 0.12 eV [110]. Optical band gap of organic carbon coated on soot remains nearly constant (1.8-1.9 eV) over soot evolution [111]. In contrast, Russo et al. [112] measured soot optical band gap using ex-situ and in-situ methods and showed that E_g drops from 0.7 eV at HAB= 8 mm to 0.2 eV at HAB=14 mm in an ethylene premixed flame with $\phi=2.3$ as particles grow and become more mature by carbonization. Kelesidis and Pratsinis [113] correlated the evolving m of soot with its E_g obtained from quantum confinement theory (QCT) [110] for wavelengths of $\lambda= 532$ and 1064 nm [113] by linear interpolations between that of nascent ($E_g = 0.60$ eV [114]; $m = 1.51, 0.33i$ and $m = 1.48, 0.24i$ for $\lambda = 532$ and 1064 nm, respectively [107, 115]) and mature soot ($E_g = 0.25$ eV [114]; $m = 1.66, 0.76i$ and $m = 1.78, 0.92i$ for $\lambda = 532$ and 1064 nm, respectively [116]). The proposed relations were then used with soot morphologies obtained from Discrete Element Modeling (DEM) simulations to obtain the evolving Mass Absorption Cross-section (MAC), $E(m)$, and the absorption function ratio of soot ($E(\lambda=532\text{nm})/ E(\lambda=1024\text{nm})$) and compared with measurements [117, 118, 119]. Employing the relation in laser diagnostics to reprocess light extinction measurement data resulted in accurate prediction of f_v in moderate ($\phi=2.34$) [105] and rich ($\phi=3$) ethylene premixed flames [120], and f_v along the centerline of a coflow ethylene diffusion flame [121] which is necessary to close the carbon mass balance in soot generating processes.

1.5 Oxidation

Soot oxidation is described as the removal of soot mass by reaction of molecular oxygen (O_2), oxygen radical (O), and hydroxyl radical (OH) from soot surface. Because of its heterogeneous reaction kinetics and mechanisms, oxidation is expected to be sensitive to surface structure and composition. So, oxidation mechanisms depend on soot maturity and temperature-time history. In near stoichiometric and fuel-rich conditions, the contribution of OH radical to soot oxidation is predominant [122] compared to that of O radicals [123]. Femimore and Jones [124] investigated soot oxidation rate for low oxygen partial pressures and temperatures from 1530 to 1890K, highlighted the importance of OH as a major oxidation agent, and attributed the faster rates compared to those predicted by Lee et al. [125], to OH oxidation. One approach for describing OH oxidation is by introducing collision efficiency representing the fraction of collisions of OH with soot particles that resulted in the removal of a carbon atom [122]. Scanning Mobility Particle Sizer (SMPS) with a two-stage burner also showed a collision efficiency of 0.13 [126].

The empirical relation of Nagle and Strickland-Constable (NSC) [127] originally developed for oxidation of pyrolytic graphite have been widely used to describe soot oxidation by O_2 . It describes O_2 oxidation rate based on partial pressure of O_2 and the fraction of active edge sites to less reactive basal planes using the graphite analogy for soot. The dominance of edge sites at typical combustion conditions accounts for the relatively small reactivity of soot and basal planes become reactive at high temperature (>2500 K) [123]. O_2 oxidation kinetics was also described with a power-law kinetics Lee et al. [125], and shown first order in oxygen concentration [128]. Alternatively, soot oxidation can be explained based on chemical similarity using HACA mechanism assuming that active site are attached by O_2 and OH leading to loss of carbon and release of CO.

A different oxidation regime has been identified for soot at low temperatures ($T < 1000$ K) where O_2 diffuses and reacts with bulk soot accounting for most of soot mass consumption [83]. Internal oxidation compacts the pore network of soot resulting in hollow CB [129], diesel [130] and biodiesel [131] soot particles and increases their SSA up to a factor of four [130]. Oxidation can cause fragmentation of soot particles affecting their morphology. The increase in number concentration and the change of soot morphology in lean premixed flames [132] and in the oxidation region of diffusion flames [133] was attributed to fragmentation. Such a change in agglomerate morphology has not been observed in fuel-rich conditions, so fragmentation was linked to O_2 oxidation.

1.6 Research objectives

The purpose of this project is developing a process design tool to predict soot yield, morphology, composition and size distribution formed in industrial flames and reactors under different temper-

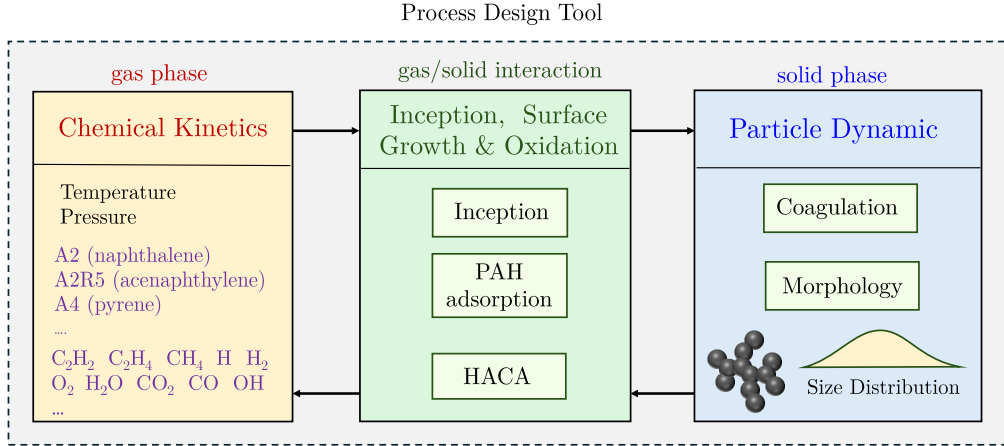


Figure 1.5: The conceptual structure of developed process design tool that account for gas mixture properties, and soot chemistry involving inception, surface growth and oxidation as well as its coagulation leading to the fractal-like morphology

atures, pressures and residence times. This tool includes a chemical kinetics unit coupled with Cantera [134] to compute thermal and physical properties of gas mixture such as temperature, pressure, density, and enthalpy based on ideal equation of state for the gas mixture. The chemistry of gas mixture is quantified using detail reaction mechanisms that enables tracking concentration of fuel (often CH_4 or C_2H_4 in the context of fundamental soot studies), intermediate species such as C_2H_2 and H_2 essential to surface growth, and PAHs such as benzene (A1), naphthalene (A2) and pyrene (A4) known as building blocks of soot. The second unit accounts for soot inception and surface growth via PAH adsorption and HACA as well as surface oxidation. It accommodates four inception models widely used in literature. The third unit deals with particle dynamics using a MPBM and SPBM to describe the coagulation of soot particles that results in their fractal-like structure with an evolving size distribution. A multi-step validation procedure is followed to assess reliability of each sub-model including collision frequency kernels for particle dynamics models, comparison of predicted agglomerate morphology with DEM results, and finally establishing energy and elemental carbon, and hydrogen balances for all combinations of particle dynamics, inception models and reactors and flames. This tool can be applied to a variety experimental targets with different temperature- and pressure-time-histories, residence times, and fuel compositions.

As the first step, methane pyrolysis in shock-tube will be simulated using a constant volume reactor. The species measurements will be used to assess the reaction mechanism and examine carbon conversion flux from fuel to smaller intermediates and larger hydrocarbons. The performance of inception models will be analyzed by comparing the predicted soot volume fraction, f_v and primary particle, d_p , with data collected from extinction and TEM measurements. A sensitivity analysis will be conducted on model parameters to identify the determining factors that control both f_v and d_p in the framework of shock-tube simulations with short residence time ≈ 2 ms and high temperatures ($\geq 2000\text{K}$). Then, the optimization of inception models will be performed by adjusting the rate constants within their physical limit (maximum collision rate of molecules) to minimize the prediction error for yield and morphology. This shows the range of inception flux that enables the model to predict soot yield and morphology represented by f_v and d_p , respectively in good agreement with measurements. Then, the optimized rates will be applied to shock-tube in a wide temperature range, and the f_v predictions will be compared with data. A similar investigation will be conducted for flow reactors using plug flow reactor model of omnisoot at lower temperatures and longer residence times and then the range of expected inception flux will be compared with those of shock-tubes.

Chapter 2

Theoretical Model

In this chapter, the mathematical basis of *omnisoot* is explained in top-to-bottom hierarchical order. The highest level is the reactors that include the transport equations of gas mixture and "soot variables" for different reactors that relies on the source terms due to soot formation. These source terms are handled by the particle dynamics model that mainly addresses particle size distribution (PSD), morphology and coagulation rate. The "PAH growth model" computes the inception and adsorption based on PAHs designated as precursors, and returns them to the particle dynamics model. Similarly, the "surface reaction" model obtains the surface growth and oxidation rate by HACA schemes and passes them to the particle dynamics model.

2.1 Assumptions and conventions

Here, the main conventions and assumptions used in the derivation of the mathematical model are listed below.

1. \dot{s}_k denotes that rate production/consumption of k_{th} species due to soot formation. It is positive when the species is released to gas mixture.
2. Each soot agglomerate consist of spherical monodisperse primary particles that are in point contact.
3. The word "*particle*" refers to soot both in spherical and agglomerate shape.
4. The density of soot is assumed constant at the value of 1800 kg/m^3 . This density represents an average between particles with large C/H ratio ($\rho = 1600 \text{ kg/m}^3$) and small C/H ratios ($\rho = 2000 \text{ kg/m}^3$) [135].
5. The incipient soot particles are 2 nm in diameter, so no particles could exist with a primary particle diameter smaller than 2 nm. The number of carbon atoms in the incipient soot particle is calculated from the mass of a sphere with the diameter of 2 nm in assuming pure carbon content.

$$d_{p,min} = 2 \text{ nm}$$
$$n_{c,min} = \frac{\pi}{6} \rho_{soot} d_{p,min}^3 \frac{1}{MW_c} \approx 378. \quad (2.1)$$

6. The calculation of PAH adsorption and soot oxidation requires "soot concentration" which is defined as **number** density of soot agglomerates per unit volume of gas. The number density of agglomerates, N_{agg} , are tracked per unit mass of gas mixture i.e. #/kg_{gas}. So, soot concentration can be calculated by multiplying agglomerate number density by gas density as:

$$[\text{soot}] = \rho \cdot N_{agg}. \quad (2.2)$$

7. The specific heat, internal energy and enthalpy of soot are approximated by those of pure graphite, and employed to close the energy balance in the system [136].
8. Soot particles and gas are in thermal equilibrium during all the studied processes, and there is no temperature gradient within each agglomerate.
9. *Soot variable* refers to the features/properties of soot particles tracked by the particle dynamics model and used in the soot transport equations.
10. *PAH growth* is a unit of the soot model with a set of pathways that determine the rate of inception and adsorption from PAHs in the gas mixture.
11. *surface reactions* is a unit of the soot model that describes the addition of acetylene to soot surface, and removal of carbon via oxidation by OH and O_2 in the HACA scheme.
12. The superscript i denotes section number of a soot variable or property derived from variables. In the case of the monodisperse model, the section number can be ignored because it is equivalent to the sectional model with one section.
13. The morphological parameters and diffusion coefficient of particles are common between particle dynamics models, so they are explained as two separate sections.

2.2 Flames

This research focuses on flames that can be described by the axisymmetric stagnation flow assumption that reduces the laminar 3D steady-state Navier-Stokes equations in the cylindrical coordinates to one-dimensional domain in r-z plane. A similar approach is applied to the energy and species conservation. The derivation of flow equations for a reacting gas is explained in detail in Section 7.2 of [137]. Here, the modified version of equations is provided that takes into account the mass and momentum of particles, the removal/release of species due to soot inception, surface growth and oxidation as well as the formation and sensible energy of soot.

Continuity:

$$\frac{\partial \rho u}{\partial z} = 2\rho V - \sum_j \dot{s}_j W_j, \quad (2.3)$$

Radial Momentum:

$$\rho u \frac{\partial V}{\partial z} + \rho V^2 = -\Lambda + \frac{\partial}{\partial z} \left(\mu \frac{\partial V}{\partial z} \right), \quad (2.4)$$

Energy:

$$[(1 - \varphi)\rho c_p + \varphi \rho_{soot} c_{p,soot}] u \frac{\partial T}{\partial z} = \frac{\partial}{\partial z} \left(K \frac{\partial T}{\partial z} \right) - \sum_k^{n_{sp}} J_k \frac{\partial h_k}{\partial z} - \sum_k^{n_{sp}} h_k W_k (\omega_k + \dot{s}_k), \quad (2.5)$$

Species:

$$\rho u \frac{\partial Y_k}{\partial z} = -\frac{\partial J_k}{\partial z} + W_j (\omega_k + \dot{s}_k), \quad (2.6)$$

where $V = v/r$ is the scaled radial velocity, and Λ is the pressure eigenvalue. J_k denotes the diffusive flux of species k that is usually calculated using mixture averaged formulation.

$$J_K^* = -\rho \frac{W_k}{W_T} D'_{km} \frac{\partial X_k}{\partial z}, \quad (2.7)$$

$$J_K = J_K^* - Y_k \sum_{l=1}^{n_{sp}} J_l^*, \quad (2.8)$$

The details of calculation of mixture-averaged diffusive fluxes can be found in the documentation of `GasTransport::getMixDiffCoeffs()`¹ in Cantera [134]. Generic soot variables are treated similar to species, and their transport equations can be written as:

$$\rho u \frac{\partial \psi}{\partial z} = - \frac{\partial}{\partial z} \left(D \frac{\partial \psi}{\partial z} \right) + S_\psi, \quad (2.9)$$

2.3 Reactors

Zero-dimensional reactors are ideal representation of reactive systems typical in industrial applications. The strong mixing in the volume/cross-section allows description of thermal/chemical/hydrodynamic properties of the mixture with a single data-point that evolves in time. This section entails the equations that describes the conservation of mass, momentum (if applicable), species, energy, and soot based on ideal gas assumption for gaseous mixture in three different types of reactors.

2.3.1 Constant Volume Reactor

This reactor assumes that the volume of the system does not change during the process. In the absence of soot, this leads to gas with constant density. However, soot formation converts part of gaseous species to solid particles thereby affecting its volume and density. Note that, continuity, species and energy transport equations only track gas mixture properties. Figure 2.1 illustrates the control volume over the gas mixture targeted by mass and energy balance equations. Any mass converted to solid soot particles leaves the control volume. Mass and energy passes through the control surface around solid particles by soot formation processes and variations in the temperature of the particles. Reactor volume is shared between gas and solid particles.

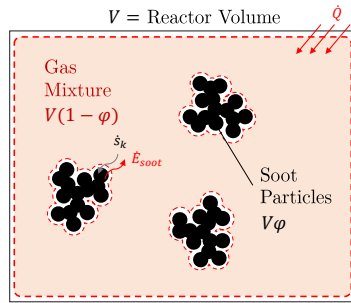


Figure 2.1: The schematics of the control volume considered for the constant volume reactor that encompasses the gas mixture and excludes the soot particles. Mass and energy are transferred between gas and soot particles.

The continuity for this reactor can be written as:

$$\frac{d}{dt}(\rho(1 - \varphi)) = (1 - \varphi) \sum_i \dot{s}_i W_i. \quad (2.10)$$

Similarly, the species equation for species k is expressed as:

$$\frac{dY_k}{dt} = \frac{\dot{m}_{in}}{\rho V (1 - \varphi)} (Y_k^* - Y_k) + \frac{1}{\rho} (\dot{\omega}_k + \dot{s}_k) W_k - \frac{1}{\rho} Y_k \sum_i \dot{s}_i W_i. \quad (2.11)$$

The energy balance for the constant volume reactor considering an external heat source of \dot{Q} can

¹https://cantera.org/documentation/docs-3.0/doxygen/html/d8/d58/classCantera_1_1GasTransport.html

be simplified to the equation that describes the temperature variations.

$$\frac{dT}{dt} = \frac{1}{\rho(1-\varphi)c_v + \rho_{soot}\varphi c_{v,soot}} \left[-(1-\varphi) \sum_k e_k (\dot{\omega}_k + \dot{s}_k) W_k + u_{soot}(1-\varphi) \sum_k \dot{s}_k W_k + \frac{\dot{Q}}{V} \right]. \quad (2.12)$$

The transport equation for a generic soot variable, ψ can be written as:

$$\frac{d\psi}{dt} = S_\psi - \frac{\psi}{\rho} \sum_i \dot{s}_i W_i. \quad (2.13)$$

2.3.2 Perfectly Stirred Reactor

In this reactor, gas enters with a mass flow rate \dot{m}_{in} , composition of Y^* and temperature of T^* , instantaneously mixes and homogeneously reacts with the mixture resident inside the reactor to reach a spatially uniform temperature and composition described by a single T , and Y . It is assumed that temperature, composition and soot properties of the outflow are the same as the reactor. Figure 2.2 illustrates the schematics of PSR. \dot{m}_{in} and \dot{m}_{out} refer to inflow and outflow gas mass flow rates, respectively. Under no-soot conditions, the inlet and outlet mass flow rates are equal, but the gas mixture loses mass by soot formation, so \dot{m}_{out} is slightly less than \dot{m}_{in} . The pressure of the reactor is assumed to stay constant during the process [137]. The nominal residence time of gas mixture in the reactor is defined as:

$$\tau = \frac{\rho V}{\dot{m}_{in}}. \quad (2.14)$$

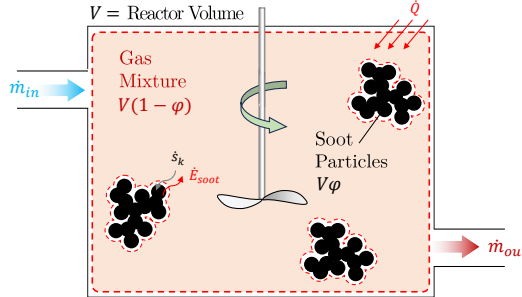


Figure 2.2: The schematics of the control volume considered for the perfectly stirred reactor that encompasses the gas mixture and excludes the soot particles. Mass and energy are transferred between gas and soot particles. The inlet flow brings species and enthalpy into the control volume and the outflow discharges them. The gas mass flow rate reduces due to soot formation.

The conservation of mass can be written for PSR by considering the mass flux of in- and outflow, and the removal of mass due to soot generation as:

$$\frac{dm}{dt} = \dot{m}_{in} - \dot{m}_{out} + (1 - \varphi) \sum_i \dot{s}_i W_i. \quad (2.15)$$

The density is not determined by solving the continuity equation, but rather from ideal gas law and assuming a constant pressure and the composition from solving the species transport equations

$$\frac{dY_k}{dt} = \frac{1}{\tau} (Y_k^* - Y_k) + \frac{1}{\rho} \left[(\dot{\omega}_k + \dot{s}_k) W_k - Y_k \sum_i \dot{s}_i W_i \right]. \quad (2.16)$$

The energy equation for this reactor is written as:

$$\frac{dT}{dt} = \frac{1}{\rho(1-\varphi)c_p + \rho_{soot}c_{p,soot}\varphi} \left[\frac{\dot{m}_{in}}{V} (h^* - h) - \frac{\dot{m}_{in}}{V} \sum_k (Y_k^* - Y_k) h_k \right. \\ \left. - (1-\varphi) \sum_k (\dot{\omega}_k + \dot{s}_k) W_k h_k + (1-\varphi) \sum_i \dot{s}_i W_i h_{soot} + \frac{\dot{Q}}{V} \right]. \quad (2.17)$$

The soot transport equations can also be expressed as:

$$\frac{d\psi}{dt} = \frac{\dot{m}_{in}}{\rho V (1-\varphi)} (\psi^* - \psi) + S_\psi - \frac{1}{\rho} \psi \sum_i \dot{s}_i W_i. \quad (2.18)$$

2.3.3 Plug Flow Reactor

The plug flow reactor (PFR) is based on a channel or duct with a constant cross-sectional area where a steady-state one-dimensional flow changes temperature, composition, and soot properties along the channel. There is no spatial gradient over the cross-section due to strong mixing, and diffusion along the channel is negligible. The pressure is assumed constant along the reactor.

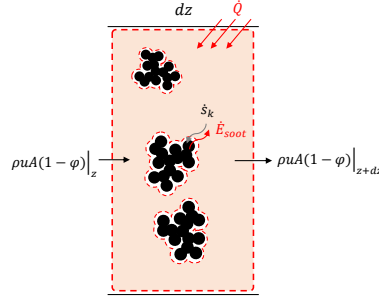


Figure 2.3: The schematics of the control volume for a differential element along PFR that includes the gas mixture and excludes the soot particles considering wall heat transfer. Mass and energy are transferred between gas and soot.

The continuity equation for PFR is written as:

$$\frac{d}{dz}(\rho u(1-\varphi)) = (1-\varphi) \sum_i \dot{s}_i W_i. \quad (2.19)$$

The momentum equation can also be established as:

$$u(1-\varphi) \sum_i \dot{s}_i W_i + \rho u(1-\varphi) \frac{du}{dz} = -\frac{d}{dz}(P(1-\varphi)) - \frac{\tau_w}{R_H}. \quad (2.20)$$

where τ_w is the wall shear stress can be determined from fraction factor, f as:

$$\tau_w = \frac{1}{2} \rho u^2 f. \quad (2.21)$$

The friction factor, f can be calculated with a good accuracy for the entire range of Reynolds number, Re , from laminar to turbulent flow using the explicit formula given by Haaland [138]:

$$\frac{1}{f^{1/2}} = -1.8 \log \left(\frac{6.9}{Re} + \left[\frac{\epsilon/D_H}{3.7} \right]^{1.11} \right), \quad (2.22)$$

where ϵ is the roughness of reactor wall. R_H and D_H are hydraulic radius and diameter, respectively that can be determined from cross-section geometry of reactor as:

$$D_H = 4R_H = \frac{4A_c}{P_c}, \quad (2.23)$$

A_c and P_c are cross-sectional area and wetted perimeter of the reactor. The species equation can be expressed as:

$$\frac{dY_k}{dz} = \frac{1}{\rho u} \left[(\dot{\omega}_k + \dot{s}_k) W_k - Y_k \sum_i \dot{s}_i W_i \right]. \quad (2.24)$$

The energy equation can be expressed as:

$$\frac{dT}{dz} = \frac{1}{\rho u(1-\varphi)c_p + \rho_{soot}u\varphi c_{p,soot}} \left[-(1-\varphi) \sum_k h_k (\dot{\omega}_k + \dot{s}_k) W_k + h_{soot}(1-\varphi) \sum_k \dot{s}_k W_k + \dot{q}' \right]. \quad (2.25)$$

The soot transport equations can also be written as:

$$\frac{d\psi}{dz} = \frac{S_\psi}{u} - \frac{\psi}{\rho u} \sum_i \dot{s}_i W_i. \quad (2.26)$$

2.4 Particle Dynamics

Population balance models rely on the Eulerian description of particles where bulk properties of particle population such as number density, mass or surface area are treated as continuous quantities and tracked by solving scalar transport equations. These methods are computationally cheaper compared with mesoscale models such as DEM, and can be easily interfaced with chemical kinetics in CFD solvers to simulate soot formation in turbulent configurations. Here, we use two particle dynamics models: a monodisperse population balance model (MPBM) based on four variables leading to 4 transport equations in total, and fixed sectional population balance model (SPBM) tracking three variables per section. The total number of transport equations in the sectional model is determined by the number of sections and number of equations solved per section. The first two/three variables in the MPBM/SPBM enables description of number, mass, and evolving fractal-like morphology of soot agglomerates that are necessary to accurately predict collision frequency of agglomerates [139] as well as oxidation and surface growth rates [81]. The last variable tracks the number of hydrogen atoms in agglomerates that allows the model to capture the soot composition, thereby its maturity [45], and surface reactivity [47]. The tracked variables are used to address particle dynamics that includes (i) reconstructing particles morphology by determining characteristic diameters from tracked soot variables, (ii) calculating collision frequency and coagulation source term, (iii) combining the contribution of inception, PAH adsorption, surface growth and oxidation into source terms. First, common features of both particle dynamics models are reviewed. As mentioned before, any parameter with superscript i denotes the section number, which can be ignored/dropped for the MPBM that only has one section. For example, d_m^i can be replaced with d_m .

2.4.1 Soot Morphology

The evolving fractal-like structure of agglomerates are quantified by their mobility diameter normalized by primary particle, d_m/d_p , and gyration, d_m/d_g , diameters can be described with power laws derived from mesoscale simulations. Incipient soot is initially a sphere formed of PAHs with constant density that grows in size by surface reactions and forms agglomerates by coagulation. The collision frequency of particles depends on their evolving fractal structure because they have larger cross-sectional area compared with mass-equivalent spheres [139]. Some simplifying assumptions are made to reconstruct the particle morphology from tracked variables. The primary particles of each agglomerate are similar enough that can be described by mean size and composition. They

also stay in point contact during surface growth and agglomeration i.e. the necking is ignored. A universal fractal dimension, $D_f = 1.9$ is used for agglomerates larger than the sphere [140]. The evolving morphology of soot agglomerates by their mobility diameter normalized by primary particle, d_m/d_p , and gyration, d_g/d_p , diameters that are related to the number of primary particles using power-laws derived from DEM simulations [68] Mobility and gyration diameters are the diameter of a sphere with the same translational and rotational properties of the agglomerate, respectively. The employed power-laws have been shown to describe the morphology of soot from premixed [82], diffusion [141] flames, and diesel engines [142]. Figure 2.4 illustrates the schematics of sample soot agglomerates with 12 primary particles and depicted d_p , d_m , and d_g .

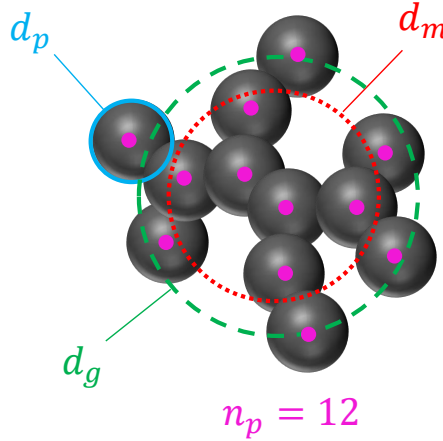


Figure 2.4: The schematics of a soot agglomerates with 12 primary particles ($n_p = 12$). Primary particle (d_p), mobility (d_m), and gyration (d_g) are shown.

n_p is the number of primary particles in each agglomerate that can be obtained by dividing the number density of primary particles by that of agglomerates of that section,

$$n_p^i = \frac{N_{pri}^i}{N_{agg}^i}. \quad (2.27)$$

Primary particle diameter, d_p , can be obtained from total carbon and number density of primary particles using

$$d_p^i = \left(\frac{6 C_{tot}^i \cdot W_{carbon}}{\pi \rho_{soot} N_{pri}^i \cdot Av} \frac{1}{N_{agg}^i} \right)^{1/3}. \quad (2.28)$$

The DEM-derived power-laws [68] relate d_m and d_g to d_p and n_p as

$$d_m^i = d_p^i \cdot n_p^{i 0.45}, \quad (2.29)$$

$$d_g^i = \begin{cases} d_m^i / (n_p^{i - 0.2} + 0.4), & \text{if } n_p^i > 1.5 \\ d_m^i / 1.29, & \text{if } n_p^i \leq 1.5 \end{cases} \quad (2.30)$$

The collision diameter, d_c^i is the maximum of d_m^i , d_g^i :

$$d_c^i = \max(d_m^i, d_g^i) \quad (2.31)$$

d_m^i , d_g^i , d_c^i are used to calculate the source terms due to the surface growth, oxidation, PAH adsorption and coagulation.

The volume equivalent diameter, d_v^i , is the diameter of the sphere with the same mass as agglomerate, and it is obtained as:

$$d_v^i = d_p^i \cdot n_p^{i/3} \quad (2.32)$$

The primary particle surface area is calculated from d_p^i assuming spherical primary particles.

$$A_p^i = \pi d_p^{i/2}, \quad (2.33)$$

A_{tot}^i (for each section) is defined as the total surface area of soot particles per unit mass of gas mixture obtained as

$$A_{tot}^i = N_{pri} A_v \cdot A_p^i. \quad (2.34)$$

2.4.2 Diffusion of soot particles

The diffusion coefficient of soot particle, D^i , is calculated as

$$D^i = \frac{k_B T}{f}, \quad (2.35)$$

where f is the friction factor of particles in gas,

$$f^i = \frac{3\pi\mu d_m^i}{C^i(d_m^i)}, \quad (2.36)$$

where C^i is the Cunningham function that corrects the friction factor given a diameter in the continuum regime for transition and free molecular regimes as:

$$C^i(d) = 1 + \frac{2\lambda}{d} \left(1.21 + 0.4 \cdot \exp\left(\frac{-0.78d}{\lambda}\right) \right), \quad (2.37)$$

where λ is the mean free path of gas given as:

$$\lambda = \frac{\mu}{\rho} \sqrt{\frac{\pi W_{gas}}{2k_B A_v T}}. \quad (2.38)$$

Note that, λ is a property of the gas mixture that does not depend on particle morphology and size section. The mean velocity, c^i and mean stop distance of particles, λ_a^i can be calculated as:

$$c^i = \sqrt{\frac{8k_B T}{\pi m_{agg}^i}}. \quad (2.39)$$

$$\lambda_a^i = \frac{8D^i}{\pi c^i}. \quad (2.40)$$

The mean distance of particles are also calculated as:

$$\delta_a^i = \frac{1}{d_c^i \lambda_a^i} \left[(d_c^i + \lambda_a^i)^3 - (d_c^{i/2} + \lambda_a^{i/2})^{3/2} \right] - d_{c,j}. \quad (2.41)$$

2.4.3 Soot Composition

The composition of soot is characterized by their elemental carbon to hydrogen ratio (C/H) is a measure of soot maturity and increases from C/H < 2 for incipient soot [143] to 2 < C/H < 10 for nascent soot [144] and C/H > 20 for mature soot [93]. The soot agglomerates are assumed to have pure carbon graphitic core [45] with all hydrogen atoms on the surface [47]. C/H ratio can be obtained from total carbon and hydrogen content as:

$$\left(\frac{C}{H}\right)^i = \frac{C_{tot}^i}{H_{tot}^i}. \quad (2.42)$$

The carbon content of each agglomerate is a predefined parameter in the SPBM, but it can be calculated by dividing C_{tot} by N_{agg} for the MPBM. The hydrogen content of each agglomerate is calculated for both particle dynamics models as:

$$H_{agg}^i = \frac{H_{tot}^i}{N_{agg}^i}. \quad (2.43)$$

2.4.4 Monodisperse Population Balance Model

The MPBM used in this research tracks the number density of primary particles (N_{pri}) and agglomerates (N_{agg}), total carbon (C_{tot}) and hydrogen (H_{tot}) content of soot particles per unit mass of gas mixture. The morphological parameters such as primary particle, mobility and gyration diameters obtained from these soot variables are the average values for the population.

2.4.4.1 Coagulation

Coagulation is the process during which solid and hard soot particles collide and attach at point of contact leading to larger agglomerates. This process conserves the soot mass and composition and number density of primary particles, so coagulation only affects N_{agg} . I_{coag}^N accounts for the decay rate of N_{agg} by the binary collision of soot particles by

$$I_{coag} = -\frac{1}{2}\beta N_{agg}^2, \quad (2.44)$$

where β is the collision frequency of agglomerates for the free molecular ($Kn > 10$) to continuum regime ($Kn < 0.1$). The value of β in the transition regime ($0.1 < Kn < 10$) can be calculated from the harmonic mean of the continuum (β_{cont}) and free molecular (β_{fm}) regime values. Additionally, an enhancement factor of %82 is applied to take into account the effect of polydispersity [69] as:

$$\beta = 1.82 \frac{\beta_{fm} \beta_{cont}}{\beta_{fm} + \beta_{cont}}, \quad (2.45)$$

$$\beta_{fm} = 4 \sqrt{\frac{\pi k_b T}{m_{agg}}} d_g^2, \quad (2.46)$$

$$\beta_{cont} = 8\pi d_c D. \quad (2.47)$$

Alternatively, β can be obtained using Fuchs interpolation [145] as:

$$\beta = \beta_{cont} \left(\frac{d_c}{d_c + 2\sqrt{2}\delta} + \frac{8D}{\sqrt{2}c_r d_c} \right)^{-1}. \quad (2.48)$$

2.4.4.2 Source terms

The source terms of tracked variables combines the effect of the inception, PAH adsorption, surface growth and oxidation and coagulation.

$$S_{N_{agg}} = \frac{I_{N,inc}}{n_{c,min}} + I_{coag}. \quad (2.49)$$

$$S_{N_{pri}} = \frac{I_{N,inc}}{n_{c,min}}. \quad (2.50)$$

$$S_{C_{tot}} = I_{C_{tot},inc} + I_{C_{tot},gr} + I_{C_{tot},ads} + I_{C_{tot},ox}. \quad (2.51)$$

$$S_{H_{tot}} = I_{H_{tot},inc} + I_{H_{tot},gr} + I_{H_{tot},ads} + I_{H_{tot},ox}. \quad (2.52)$$

The partial source terms in Equations denoted by I are determined by PAH growth and surface reaction model explained in Sections 2.6 and 2.5, respectively.

2.4.5 Sectional Population Balance Model

A SPBM with the fixed pivot is used to describe particle dynamics [146]. The mass range of particles are divided into discrete sections that include agglomerates of the same mass. Inception introduces new particles to the first section with the mass corresponding to the incipient particle. The particles of the first section can migrate to upper sections by gaining mass via surface growth and coagulation, and return to lower sections when they lose mass through oxidation. The mass of sections is determined by a geometric progression with a scale factor equal to the mass of the incipient soot particle, and a common ratio of SF, known as sectional spacing factor. The mass of section is approximated by the carbon content of agglomerates in moles as:

$$C_{agg}^i = \frac{n_{c,min}}{Av} \cdot SF^{i-1}. \quad (2.53)$$

So, the mass of hydrogen is ignored in the placement of agglomerates in the sections. The total number density of agglomerates, N_{agg}^i [mol/kg], and primary particles, N_{pri}^i [mol/kg] are tracked for each section. Morphological parameters are determined for each section according to the equations in Section 2.4.1.

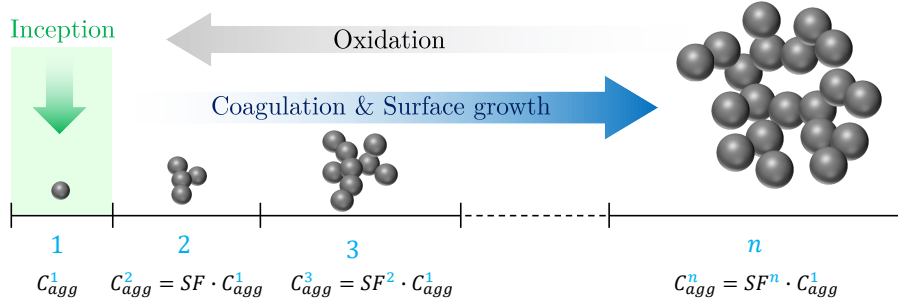


Figure 2.5: The illustration of sections of SPBM. The mass of sections grows progressively by the scale factor of SF. Inception introduces new particles to the first section that propagate to the upper section via coagulation and surface growth and return to lower sections by oxidation

2.4.5.1 Coagulation

In SPBM approach, collisions between particles from every two sections are considered. The new particles formed by coagulation are placed in an upper section with the mass equal to sum of particles involved in the collision. When the mass of yielded particle lies between two consecutive sections, the particles are divided among these sections proportional to their mass. One possible scenario is that the mass of the newly formed particle is greater than the last section, thus leaving tracked mass range. Losing mass is a potential problem with the fixed pivot sectional model, which can be avoided by selecting proper number of sections and spacing factor to ensure the last sections stay empty during the simulation.

The collision frequency between sections j and k can be obtained from the harmonic mean of the values in the continuum and free molecular regimes as:

$$\beta^{jk} = \frac{\beta_{fm}^{jk} \beta_{cont}^{jk}}{\beta_{fm}^{jk} + \beta_{cont}^{jk}}, \quad (2.54)$$

$$\beta_{fm}^{jk} = \sqrt{\frac{\pi k_b T}{2} \left(\frac{1}{m_{agg}^j} + \frac{1}{m_{agg}^k} \right) (d_c^j + d_c^k)^2}, \quad (2.55)$$

$$\beta_{cont}^{jk} = \frac{2k_B T}{3\mu} \left(\frac{C^j}{d_m^j} + \frac{C^k}{d_m^k} \right) (d_c^j + d_c^k)^2. \quad (2.56)$$

The collision frequency can also be determined from the Fuchs interpolation similar to the MPBM as:

$$\beta^{jk} = \beta_{cont}^{ij} \left[\frac{d_c^j + d_c^k}{d_c^j + d_c^k + 2 + \delta_r^{jk}} + \frac{8(D^j + D^k)}{\bar{c}_r^{jk} (d_c^j + d_c^k)} \right]^{-1}, \quad (2.57)$$

where δ_r^{jk} and \bar{c}_r^{jk} are the mean square root of mean distance and velocity of particles, respectively.

$$\delta_r^{jk} = \sqrt{\delta_a^j + \delta_a^k}, \quad (2.58)$$

$$\bar{c}_r^{jk} = \sqrt{c^j + c^k}. \quad (2.59)$$

Coagulation redistributes the total number of agglomerates and primary particles as well as hydrogen atoms among the sections. The partial coagulation source terms for N_{agg}^i , N_{pri}^i and H_{tot}^i can be calculated as:

$$I_{N_{agg}}^i = \sum_{k=1}^{n_{sec}} \sum_{j=k}^{n_{sec}} \left(1 - \frac{\delta_{jk}}{2} \right) \eta_{ijk} \beta^{jk} N_{agg}^j N_{agg}^k - N_{agg}^i \sum_{k=1}^{n_{sec}} \beta^{im} N_{agg}^m. \quad (2.60)$$

$$I_{N_{pri}}^i = \sum_{k=1}^{n_{sec}} \sum_{j=k}^{n_{sec}} \left(1 - \frac{\delta_{jk}}{2} \right) \eta_{p,ijk} \eta_{ijk} \beta^{jk} N_{agg}^j N_{agg}^k - N_{pri}^i \sum_{k=1}^{n_{sec}} \beta^{im} N_{agg}^m. \quad (2.61)$$

$$I_{H_{tot}}^i = \sum_{k=1}^{n_{sec}} \sum_{j=k}^{n_{sec}} \left(1 - \frac{\delta_{jk}}{2} \right) \eta_{h,ijk} \eta_{ijk} \beta^{jk} N_{agg}^j N_{agg}^k - H_{tot}^i \sum_{k=1}^{n_{sec}} \beta^{im} N_{agg}^m. \quad (2.62)$$

where δ_{jk} is the Kronecker delta defined as:

$$\delta_{jk} = \begin{cases} 1, & \text{if } j = k \\ 0, & \text{if } j \neq k \end{cases} \quad (2.63)$$

In Equation (2.60), η_{ijk} assigns newly formed agglomerates to the two consecutive section in order to conserves mass during coagulation [73].

$$\eta_{ijk} = \begin{cases} \frac{C_{agg}^{i+1} - C_{agg}^{jk}}{C_{agg}^{i+1} + C_{agg}^i}, & \text{if } C_{agg}^i \leq C_{agg}^{jk} < C_{agg}^{i+1} \\ \frac{C_{agg}^i - C_{agg}^{jk}}{C_{agg}^i + C_{agg}^{i-1}}, & \text{if } C_{agg}^{i-1} \leq C_{agg}^{jk} < C_{agg}^i \\ 0 & \text{else} \end{cases} \quad (2.64)$$

where $C_{agg}^{jk} = C_{agg}^j + C_{agg}^k$. Similarly, $\eta_{p,ijk}$ in Equation (2.61) and $\eta_{h,ijk}$ in Equation (2.62) adjust the number primary particles and hydrogen atoms added to consecutive sections based on their mass.

$$\eta_{p,ijk} = \frac{C_{agg}^i}{C_{agg}^{jk}} (n_p^j + n_p^k), \quad (2.65)$$

$$\eta_{h,ijk} = \frac{C_{agg}^i}{C_{agg}^{jk}} (H_{agg}^j + H_{agg}^k), \quad (2.66)$$

2.4.5.2 Source terms

The source terms are split into four part showing the contribution of different soot formation and evolution factors. The effect of surface growth and PAH adsorption are combined because they are similar mass gaining mechanisms.

$$S_{N_{agg}} = (S_{N_{agg}})_{inc} + (S_{N_{agg}})_{gr,ads} + (S_{N_{agg}})_{ox} + (S_{N_{agg}})_{coag}, \quad (2.67)$$

$$S_{N_{pri}} = (S_{N_{pri}})_{inc} + (S_{N_{pri}})_{gr,ads} + (S_{N_{pri}})_{ox} + (S_{N_{pri}})_{coag}, \quad (2.68)$$

$$S_{H_{tot}} = (S_{H_{tot}})_{inc} + (S_{H_{tot}})_{gr,ads} + (S_{H_{tot}})_{ox} + (S_{H_{tot}})_{coag}. \quad (2.69)$$

Inception introduces equal number of agglomerates and primary particles as well as hydrogen to the first section.

$$(S_{N_{agg}})_{inc} = \frac{1}{Av} \frac{I_{N,inc}}{C_{agg}^i}, \quad i = 1. \quad (2.70)$$

$$(S_{N_{pri}})_{inc} = \frac{1}{Av} \frac{I_{N,inc}}{C_{agg}^i}, \quad i = 1. \quad (2.71)$$

$$(S_{H_{tot}})_{inc} = I_{H,inc}, \quad i = 1. \quad (2.72)$$

Surface growth and PAH adsorption increase the (carbon) mass and hydrogen content of agglomerates, and transfer them to upper sections. The removal rate of agglomerates (N_{agg}^i) from the origin section due to surface growth and PAH adsorption must be equal to the addition rate of agglomerates to the target section to conserve the mass, and it is calculated by dividing the mass growth rate by the difference of the mass of the adjacent sections.

$$(S_{N_{agg}})_{gr,ads} = \frac{1}{Av} \begin{cases} -\frac{I_{C_{tot},gr}^i + I_{C_{tot},ads}^i}{C_{agg}^{i+1} - C_{agg}^i} & \text{if } i = 1 \\ \frac{I_{C_{tot},gr}^{i-1} + I_{C_{tot},ads}^{i-1}}{C_{agg}^i - C_{agg}^{i-1}} - \frac{I_{C_{tot},gr}^i + I_{C_{tot},ads}^i}{C_{agg}^{i+1} - C_{agg}^i} & \text{if } 1 < i < n_{sec} \\ \frac{I_{C_{tot},gr}^{i-1} + I_{C_{tot},ads}^{i-1}}{C_{agg}^i - C_{agg}^{i-1}} & \text{if } i = n_{sec} \end{cases} \quad (2.73)$$

As agglomerates migrate up/down through sections, they carry the number of primary particles as well as hydrogen atoms, so the transfer rate of agglomerates is multiplied by n_p^i and H_{agg}^i , respectively.

$$(S_{N_{pri}})_{gr,ads} = \frac{1}{Av} \begin{cases} -\frac{I_{C_{tot},gr}^i + I_{C_{tot},ads}^i}{C_{agg}^{i+1} - C_{agg}^i} & \text{if } i = 1 \\ \frac{I_{C_{tot},gr}^{i-1} + I_{C_{tot},ads}^{i-1}}{C_{agg}^i - C_{agg}^{i-1}} n_p^{i-1} - \frac{I_{C_{tot},gr}^i + I_{C_{tot},ads}^i}{C_{agg}^{i+1} - C_{agg}^i} n_p^i & \text{if } 1 < i < n_{sec} \\ \frac{I_{C_{tot},gr}^{i-1} + I_{C_{tot},ads}^{i-1}}{C_{agg}^i - C_{agg}^{i-1}} n_p^{i-1} & \text{if } i = n_{sec} \end{cases} \quad (2.74)$$

$$(S_{H_{tot}})_{gr,ads} = \frac{1}{Av} \begin{cases} -\frac{I_{C_{tot},gr}^i + I_{C_{tot},ads}^i}{C_{agg}^{i+1} - C_{agg}^i} H_{agg}^i + I_{H_{tot},gr}^i + I_{H_{tot},ads}^i & \text{if } i = 1 \\ \frac{I_{C_{tot},gr}^{i-1} + I_{C_{tot},ads}^{i-1}}{C_{agg}^i - C_{agg}^{i-1}} H_{agg}^{i-1} - \frac{I_{C_{tot},gr}^i + I_{C_{tot},ads}^i}{C_{agg}^{i+1} - C_{agg}^i} H_{agg}^i + I_{H_{tot},gr}^i + I_{H_{tot},ads}^i & \text{if } 1 < i < n_{sec} \\ \frac{I_{C_{tot},gr}^{i-1} + I_{C_{tot},ads}^{i-1}}{C_{agg}^i - C_{agg}^{i-1}} H_{agg}^{i-1} + I_{H_{tot},gr}^i + I_{H_{tot},ads}^i & \text{if } i = n_{sec} \end{cases} \quad (2.75)$$

Similarly, the agglomerates lose (carbon) mass by oxidation, and descend to the lower sections carrying primary particle and hydrogen.

$$(S_{N_{agg}})_{ox} = \frac{1}{Av} \begin{cases} \frac{I_{C_{tot},ox}^{i+1}}{C_{agg}^{i+1} - C_{agg}^i} - \frac{I_{C_{tot},ox}^i}{C_{agg}^i} & \text{if } i = 1 \\ \frac{I_{C_{tot},ox}^{i+1}}{C_{agg}^{i+1} - C_{agg}^i} - \frac{I_{C_{tot},ox}^i}{C_{agg}^i - C_{agg}^{i-1}} & \text{if } 1 < i < n_{sec} \\ -\frac{I_{C_{tot},ox}^i}{C_{agg}^i - C_{agg}^{i-1}} & \text{if } i = n_{sec} \end{cases} \quad (2.76)$$

$$(S_{N_{pri}})_{ox} = \frac{1}{Av} \begin{cases} \frac{I_{C_{tot},ox}^{i+1}}{C_{agg}^{i+1} - C_{agg}^i} n_p^{i+1} - \frac{I_{C_{tot},ox}^i}{C_{agg}^i} & \text{if } i = 1 \\ \frac{I_{C_{tot},ox}^{i+1}}{C_{agg}^{i+1} - C_{agg}^i} n_p^{i+1} - \frac{I_{C_{tot},ox}^i}{C_{agg}^i - C_{agg}^{i-1}} n_p^i & \text{if } 1 < i < n_{sec} \\ -\frac{I_{C_{tot},ox}^i}{C_{agg}^i - C_{agg}^{i-1}} n_p^i & \text{if } i = n_{sec} \end{cases} \quad (2.77)$$

$$(S_{H_{tot}})_{ox} = \frac{1}{Av} \begin{cases} \frac{I_{C_{tot},ox}^{i+1}}{C_{agg}^{i+1} - C_{agg}^i} H_{agg}^{i+1} - \frac{I_{C_{tot},ox}^i}{C_{agg}^i} H_{agg}^i + I_{H_{tot},ox}^i & \text{if } i = 1 \\ \frac{I_{C_{tot},ox}^{i+1}}{C_{agg}^{i+1} - C_{agg}^i} H_{agg}^{i+1} - \frac{I_{C_{tot},ox}^i}{C_{agg}^i - C_{agg}^{i-1}} H_{agg}^i + I_{H_{tot},ox}^i & \text{if } 1 < i < n_{sec} \\ -\frac{I_{C_{tot},ox}^i}{C_{agg}^i - C_{agg}^{i-1}} H_{agg}^i + I_{H_{tot},ox}^i & \text{if } i = n_{sec} \end{cases} \quad (2.78)$$

2.5 Surface reactions model

The heterogeneous surface reactions are described by hydrogen-abstraction-acetylene-addition (HACA) mechanism [40, 59]. The soot growth in HACA scheme is based on a sequential process similar to PAH growth. The hydrogenated arm-chair sites ($C_{soot} - H$) on the edge of aromatic rings are dehydrogenated (C_{soot}°) that can form bond with C_2H_2 adding an additional aromatic ring with hydrogenated site. These sites can also be attacked by O_2 or OH . The elementary reactions that describe this sequential process are listed in Table 2.1. The rate of mass growth by HACA is obtained from reaction of C_2H_2 with dehydrogenated sites as:

$$\omega_{gr}^i = \alpha^i k_{f4} [C_2H_2] [C_{soot}^\circ]. \quad (2.79)$$

where k_{f4} denotes the forward rate of 4th reaction in Table 2.1, and $[C_{soot}^\circ]$ is obtained by multiplying the surface density of dehydrogenated sites, χ_{soot}° with total surface area of soot (per unit of mass of gas mixture) as:

$$[C_{soot}^i] = \frac{\rho}{Av} A_{tot}^i \cdot \chi_{soot}^i. \quad (2.80)$$

χ_{soot}^i is calculated by assuming the steady-state for $[C_{soot}^i]$ in the system of reactions in Table 2.1:

$$\chi_{soot}^i = \frac{k_{f1}[H] + k_{f2}[OH]}{k_{r1}[H_2] + k_{r2}[H_2O] + k_{f3}[H] + k_{f4}[C_2H_2] + k_{f5}[O_2] + k_{f1}[H] + k_{f2}[OH]} \chi_{soot_{CH}}, \quad (2.81)$$

where $\chi_{soot_{CH}}$ is the surface density of hydrogenated sites estimated based on the assumption that soot surface is covered with stacks of benzene rings [59]. Considering the stack spacing of 3.15 Å and 2 C–H bonds per benzene ring length, the surface density of hydrogenated sites, χ_{soot-H} , is calculated to be $0.23\text{site}/\text{\AA}^2 = 2.3 \times 10^{19}\text{site}/\text{m}^2$, which give the maximum theoretical limit of the reaction sites.

In Equation (2.79), α is the surface reactivity factor between 0 and 1 that represents the decline of reaction sites from the theoretical limit due to particle aging, growth and maturity [147, 148], and it has been observed to depend on temperature time history [149, 61]. The value of α has been described using constant target-specific values as well as empirical equations based on particle size and flame temperature. Blanquart and Pitsch [87] related α to the number of surface hydrogen atoms on the soot particles. A detailed review of these can be found in the chapter 4 of [150]. Here, the empirical equations proposed by Appel et al. [59] is used to calculate α :

$$\alpha^i = \tanh \left(\frac{12.56 - 0.00563 \cdot T}{\log_{10} \left(\frac{\rho_{soot} \cdot Av}{W_{carbon}} \frac{\pi}{6} d_p^3 \right)} - 1.38 + 0.00068 \cdot T \right). \quad (2.82)$$

The contribution of HACA to growth source terms can be computed from HACA rate considering the number of carbon atoms in C_2H_2 and number of arm-chair and zig-zag hydrogenated sites on soot particle [47] using

$$I_{C_{tot},gr}^i = 2\omega_{gr}^i / \rho, \quad (2.83)$$

$$I_{H_{tot},gr}^i = 0.25\omega_{gr}^i / \rho. \quad (2.84)$$

The rate change of C_2H_2 concentration due to mass growth is written as:

$$\left(\frac{d[C_2H_2]}{dt} \right)_{gr} = - \sum_{i=1}^{n_{sec}} \omega_{gr}^i. \quad (2.85)$$

The rate of release of H radicals into the gas mixture due to surface growth is:

$$\left(\frac{d[H]}{dt} \right)_{gr} = 1.75 \sum_{i=1}^{n_{sec}} \omega_{gr}^i. \quad (2.86)$$

The carbons on the surface of soot are oxidized via reaction with O_2 and OH which decreases total carbon of soot and releases CO and H_2 to gas mixture. The oxidation process is described by HACA mechanism. O_2 and OH oxidation rates are calculated as

$$\omega_{ox,O_2}^i = \alpha^i k_{f5}[O_2][C_{soot}^i], \quad (2.87)$$

$$\omega_{ox,OH}^i = \alpha^i k_{f6}[OH]N_{agg}^i \rho. \quad (2.88)$$

The oxidation source term is calculated considering the number of carbon atoms removed from soot through each oxidation pathway by

$$I_{C_{tot},ox}^i = -(2\omega_{ox,O_2}^i + \omega_{ox,OH}^i) / \rho, \quad (2.89)$$

We assume that oxidation does not change the number of surface hydrogen atoms. The rate change of concentration of CO , H and OH by oxidation is calculates as:

Table 2.1: Rate coefficients for the various surface reactions in Arrhenius form $k = AT^n \cdot e^{-E/RT}$

No.	Reaction		A $\left[\frac{\text{m}^3}{\text{mol} \cdot \text{s}} \right]$	n	$\frac{E}{R} [\text{K}]$
(R 2.1)	$\text{C}_{\text{soot}-\text{H}} + \text{H} \rightleftharpoons \text{C}_{\text{soot}^\circ} + \text{H}_2$	f	4.17×10^7	0	6542.52
		r	3.9×10^6	0	5535.98
(R 2.2)	$\text{C}_{\text{soot}-\text{H}} + \text{OH} \rightleftharpoons \text{C}_{\text{soot}^\circ} + \text{H}_2\text{O}$	f	10^4	0.734	719.68
		r	3.68×10^2	1.139	8605.94
(R 2.3)	$\text{C}_{\text{soot}^\circ} + \text{H} \longrightarrow \text{C}_{\text{soot}} + \text{H}_2\text{O}$	f	10^4	0.734	719.68
(R 2.4)	$\text{C}_{\text{soot}^\circ} + \text{C}_2\text{H}_2 \longrightarrow \text{C}_{\text{soot}-\text{H}}$	f	80	1.56	1912.43
(R 2.5)	$\text{C}_{\text{soot}^\circ} + \text{O}_2 \longrightarrow 2 \text{CO}$	f	2.2×10^6	0	3774.53
(R 2.6)	$\text{C}_{\text{soot}-\text{H}} + \text{OH} \longrightarrow \text{CO} + \frac{1}{2} \text{H}_2$	f	1.3×10^7	0	0

$$\left(\frac{d[\text{CO}]}{dt} \right)_{ox} = \sum_{i=1}^{n_{sec}} \omega_{ox,O_2}^i. \quad (2.90)$$

$$\left(\frac{d[\text{O}_2]}{dt} \right)_{ox} = - \sum_{i=1}^{n_{sec}} \omega_{ox,O_2}^i. \quad (2.91)$$

$$\left(\frac{d[\text{OH}]}{dt} \right)_{ox} = - \sum_{i=1}^{n_{sec}} \omega_{ox,OH}^i. \quad (2.92)$$

$$\left(\frac{d[\text{H}_2]}{dt} \right)_{ox} = \frac{1}{2} \sum_{i=1}^{n_{sec}} \omega_{ox,OH}^i. \quad (2.93)$$

2.6 PAH growth models

Here, four different PAH growth models are used to describe the conversion of PAHs to incipient particles and their adsorption on existing agglomerates. All models are collision-based consisting of different pathways with single- or multi-step reactions. The collision frequency of gaseous species including PAH molecules and polymers depend on their mass and diameter, and it is obtained as:

$$\beta_{dim_{jk}} = 2.2 \cdot d_r^2 \sqrt{\frac{8\pi k_B T}{m_r}} \quad (2.94)$$

where d_r and m_r are reduced diameter and mass for two PAH molecule, respectively.

$$d_r = 2 \frac{d_{PAH_k} \cdot d_{PAH_j}}{d_{PAH_k} + d_{PAH_j}} \quad (2.95)$$

$$m_r = \frac{m_{PAH_k} \cdot m_{PAH_j}}{m_{PAH_k} + m_{PAH_j}} \quad (2.96)$$

The mass of each PAH molecule is obtained from its molecular weight as:

$$m_{PAH_j} = \frac{W_{PAH_j}}{Av} \quad (2.97)$$

The diameter of PAH is calculated from the mass and the density.

$$d_{PAH_j} = \left(\frac{6 \cdot m_{PAH_j}}{\pi \cdot \rho_{PAH_j}} \right)^{1/3} \quad (2.98)$$

The density of a PAH molecule is estimated using the relation proposed by Johansson et al. [151].

$$\rho_{PAH_j} = 171943.5197 \frac{W_C n_{C,PAH_j} + W_H n_{H,PAH_j}}{n_{C,PAH_j} + n_{H,PAH_j}} \quad (2.99)$$

The collision frequency of PAH_j and soot agglomerates in each section can be determined for the entire regime by harmonic mean of the collision frequency in the free molecular and continuum regimes as:

$$\beta_{ads_j}^i = \frac{\beta_{fm,ads}^i \cdot \beta_{cont,ads}^i}{\beta_{fm,ads}^i + \beta_{cont,ads}^i} \quad (2.100)$$

$$\beta_{fm,ads_j}^i = 2.2 \sqrt{\frac{\pi k_B T}{2} \left(\frac{1}{m_{agg}^i} + \frac{1}{m_{PAH_j}} \right) (d_g^i + d_{PAH_j})^2} \quad (2.101)$$

$$\beta_{cont,ad_{j,s}}^i = \frac{2k_B T}{3\mu} \left[\frac{C^i(d_m)}{d_g^i} + \frac{C^i(d_{PAH_j})}{d_{PAH_j}} \right] (d_g + d_{PAH_j}) \quad (2.102)$$

2.6.1 Irreversible Dimerization

The irreversible dimerization is based on the collision-based clustering/polymerization PAHs that form dimers, trimers, and tetramers until the polymer mass reaches a threshold that can be considered a solid particle. For practical purposes, dimer is usually considered as a incipient particle that grows by surface growth and coagulation. A single-step irreversible collision of two similar PAHs forms a new dimer as:



Similarly, the adsorption of each PAH molecule on soot particles is described by the irreversible collision of soot and PAH_j as:



The forward rate of dimerization, k_{f,dim_j} and adsorption, k_{f,ads_j} in Reactions (R 2.7) and (R 2.8) are calculated from Equations (2.94) and (2.100), respectively.

$$k_{f,dim_j} = \gamma_{inc} \cdot \beta_{jk,PAH} \cdot Av, \quad (2.103)$$

$$k_{f,ads_j}^i = \gamma_{ads_j} \cdot \beta_{j,ads}^i \cdot Av, \quad (2.104)$$

where γ_{inc} and γ_{ads} are collision efficiencies for dimerization and adsorption, respectively. Their value vary in $[10^{-7}, 1]$ range, and usually selected to match the predicted soot mass with the experimental data. Here, $\gamma_{inc} = 10^{-4}$ and $\gamma_{ads} = 10^{-3}$. The rate of dimerization and adsorption from PAH_j are calculated accordingly as:

$$w_{dim_j} = k_{f,dim_j} [PAH_j][PAH_j] \quad (2.105)$$

The partial source terms for inception are calculated as:

$$I_{N,inc} = \frac{1}{\rho} \sum_{j=1}^{n_{PAH}} w_{dim_j} 2n_{PAH_j,C} \quad (2.106)$$

$$I_{C_{tot},inc} = \frac{1}{\rho} \sum_{j=1}^{n_{PAH}} w_{dim_j} 2n_{PAH_j,C} \quad (2.107)$$

$$I_{H_{tot},inc} = \frac{1}{\rho} \sum_{j=1}^{n_{PAH}} w_{dim_j} 2n_{PAH_j,H} \quad (2.108)$$

The rate of PAH adsorption for each section is obtained as:

$$w_{ads_j}^i = k_{f,ads_j}^i [Soot][PAH_j] \quad (2.109)$$

The contribution of PAH adsorption to the source terms are expressed as:

$$I_{C_{tot},ads}^i = \frac{1}{\rho} \sum_{j=1}^{n_{PAH}} w_{ads_j}^i n_{PAH,C} \quad (2.110)$$

$$I_{H_{tot},ads}^i = \frac{1}{\rho} \sum_{j=1}^{n_{PAH}} w_{dim_j}^i (n_{PAH,H} - 2) \quad (2.111)$$

Each PAH molecule loses one H atom becoming a radical that forms bonds with a dehydrogenated site on soot surface, so two H atoms are released during the process that is taken into account in Equation (2.111).

The formation of a dimer consumes two PAH molecules, and during adsorption one PAH molecule is removed from the gas mixture, so the total rate of PAH_i removal by the irreversible dimerization is obtained as:

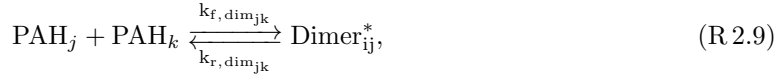
$$\left(\frac{d[PAH_j]}{dt} \right)_{inc} = -2w_{dim_j} - \sum_{i=1}^{n_{sec}} w_{ads_j}^i. \quad (2.112)$$

During the adsorption process one H₂ is released to the gas mixture.

$$\left(\frac{d[H_2]}{dt} \right)_{inc} = \sum_{i=1}^{n_{sec}} w_{ads_j}^i. \quad (2.113)$$

2.6.2 Reactive Dimerization

The design of this approach is similar to irreversible dimerization with two main differences: The first step of dimerization and adsorption is reversible forming physically bonded dimers followed by a irreversible carbonization that leads to chemical bond formation in dimers [58]. This approach allows formation of homo- and heterodimers. The dimerization of PAH_j and PAH_k is described as:



where Dimer_{jk}^{*} and Dimer_{jk} physically and chemically bonded dimers, respectively, from PAH_j and PAH_k. The forward rate of physical dimerization, k_{f,dim_{jk}} is calculated from Equation (2.94) as:

$$k_{f,dim_{jk}} = p'' \cdot \beta_{jk,PAH} \cdot Av, \quad (2.114)$$

where p'' = 0.1 accounts for the probability of PAH-PAH collisions in "FACE" configuration that results in successful van der Waals formation [152]. The reverse rate of physical dimerization, k_{r,dim_{jk}} is obtained from the dimerization equilibrium constant [54] as:

$$\log_{10} K_{eq} = a \frac{\epsilon_{jk}}{RT} + b, \quad (2.115)$$

$$k_{r,dim_{jk}} = k_{f,dim_{jk}} 10^{-b} e^{-a\epsilon_{jk}\ln(10)/(RT)}, \quad (2.116)$$

$$\epsilon_{jk} = cW_{jk} - d, \quad (2.117)$$

$$W_{jk} = \frac{W_j \cdot W_k}{W_j + W_k}, \quad (2.118)$$

where a = 0.115 (obtained from pyrere dimerization data [49]) and b=1.8 [58], c=933420 j/kg, and d=34053 j/mol [58].

The rate of chemical bond formation, k_{reac} is defined in the Arrhenius form [50] as

$$k_{reac} = 5 \times 10^6 \cdot e^{(-96232/RT)}. \quad (2.119)$$

Assuming a steady state condition for the physical dimers, $\partial[\text{Dimer}_{jk}^*]/\partial t = 0$, the rate of formation of the chemically-bonded dimer can be obtained as

$$\omega_{dim_{jk}} = k_{reac} \frac{k_{f,dim_{jk}} [\text{PAH}_j][\text{PAH}_k]}{k_{r,dim_{jk}} + k_{c,dim}}. \quad (2.120)$$

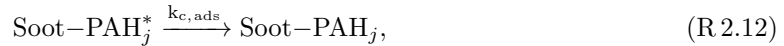
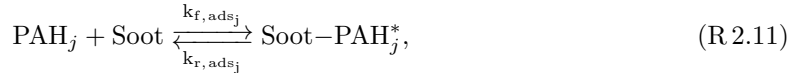
The contribution of dimer formation to partial source terms is expressed by looping over all combinations of PAHs as:

$$I_{N,inc} = \frac{1}{\rho} \sum_{j=1}^{n_{PAH}} \sum_{k=j}^{n_{PAH}} \omega_{dim_{kj}} (n_{PAH_{j,C}} + n_{PAH_{k,C}}), \quad (2.121)$$

$$I_{C_{tot},inc} = \frac{1}{\rho} \sum_{j=1}^{n_{PAH}} \sum_{k=j}^{n_{PAH}} \omega_{dim_{kj}} (n_{PAH_{j,C}} + n_{PAH_{k,C}}), \quad (2.122)$$

$$I_{H_{tot},inc} = \frac{1}{\rho} \sum_{j=1}^{n_{PAH}} \sum_{k=j}^{n_{PAH}} \omega_{dim_{kj}} (n_{PAH_{j,H}} + n_{PAH_{k,H}}), \quad (2.123)$$

Similarly, PAH adsorption is described by a two-step process where the collision of PAH_j with soot agglomerates leads to physically bonded Soot – PAH^* that is carbonized and forms chemically-bonded Soot – PAH added to soot surface.



The forward rate of PAH-soot collision is calculated from Equation (2.100), and the reverse rate is determined same as inception (Equation(2.116)).

$$k_{f,ads}^i = \beta_{jk,ads}^i \cdot Av, \quad (2.124)$$

$$k_{r,ads}^i = k_{f,ads}^i \cdot 10^{-b} e^{-a\epsilon_{soot,j}\ln(10)/(RT)}, \quad (2.125)$$

$$\epsilon_{soot,j} = cW_{soot,j} - d, \quad (2.126)$$

a, b, c, d values are the same as inception. Computing $\epsilon_{soot,j}$ also requires "equivalent soot molecular weight", W_{soot} for section i, which is estimated from carbon mass of each agglomerate as:

$$MW_{soot}^i = \frac{C_{tot}^i W_{carbon}}{N_{agg}^i} \quad (2.127)$$

The rate constant of carbonization of Soot – PAH_j^{*} is defined as in the Arrhenius form similar to inception (Equation (??)). The prefactor is adjusted based on matching the numerical PSD [50] with measurements in the ethylene pyrolysis in flow reactor [153].

$$k_{c,dim} = 2 \times 10^{10} \cdot e^{(-96232/RT)}. \quad (2.128)$$

The total adsorption rate can be calculated assuming a steady-state concentration for physically adsorbed PAH on soot, $\partial[\text{Soot} - \text{PAH}^*]/\partial t = 0$, similar to inception rate (Equation (??)) as

$$\omega_{ads_j}^i = k_{c,ads} \frac{k_{f,ads_j} [\text{Soot}][\text{PAH}_j]}{k_{r,ads_j} + k_{c,ads_j}}, \quad (2.129)$$

The contribution of PAH adsorption rate to partial source terms can be expressed as:

$$I_{C_{tot},ads}^i = \frac{1}{\rho} \sum_{i=1}^{n_{PAH}} \omega_{ads_j}^i n_{C,PAH_j}, \quad (2.130)$$

$$I_{C_{tot},ads}^i = \frac{1}{\rho} \sum_{i=1}^{n_{PAH}} \omega_{ads_j}^i (n_{H,PAH_j} - 2). \quad (2.131)$$

The rate of removal of PAH from gas mixture due to adsorption is given as

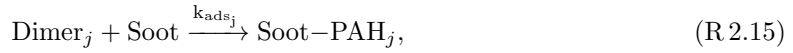
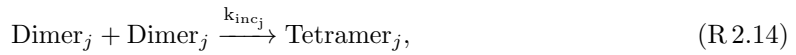
$$\left(\frac{d[\text{PAH}_j]}{dt} \right)_{inc} = - \sum_{k=1}^{n_{PAH}} w_{dim_{jk}} - \sum_{i=1}^{n_{sec}} w_{ads_j}^i. \quad (2.132)$$

During the adsorption process one H₂ is released to the gas mixture.

$$\left(\frac{d[\text{H}_2]}{dt} \right)_{inc} = \sum_{i=1}^{n_{sec}} w_{ads_j}^i. \quad (2.133)$$

2.6.3 Dimer Coalescence

Dimer coalescence model is a multi-step irreversible model proposed by Blanquart and Pitsch [87] where self-collision of PAH molecules form dimers that are intermediate state between gaseous PAH molecules and solid soot particles. The self-coalescence of dimers forms incipient soot particles. Alternatively, dimers can adsorb on the surface of existing soot particles and contribute to their surface growth. The equations are based on implementation of Dimer Coalescence by Sun et al. [154] for a sectional model.



where the rate constant of dimerization, k_{dim_j} and inception k_{inc_j} are calculated from collision rate of PAHs in Equation (2.100).

$$k_{dim_j} = \gamma_{dim_j} \cdot \beta_{jj,PAH} \cdot Av, \quad (2.134)$$

$$k_{inc_j} = \beta_{jj,dimer} \cdot Av, \quad (2.135)$$

where γ_{dim_j} is the dimerization efficiency that is assumed to scale with fourth power of PAH molecular weight [47] as:

Table 2.2: The dimerization efficiency, γ_{dim_j} , for different PAH in dimer coalescence model[47]

Species name	Chemical formula	W [kg/mol]	γ_{dim_j}
Naphthalene	C ₁₀ H ₈	0.128	0.002
Acenaphthylene	C ₁₂ H ₈	0.152	0.004
Biphenyl	C ₁₂ H ₁₀	0.154	0.0085
Phenanthrene	C ₁₄ H ₁₀	0.178	0.015
Acephenanthrylene	C ₁₆ H ₁₀	0.202	0.025
Pyrene	C ₁₆ H ₁₀	0.202	0.025
Fluoranthene	C ₁₆ H ₁₀	0.202	0.025
Cyclopenta[cd]pyrene	C ₁₈ H ₁₀	0.226	0.039

$$\gamma_{\text{dim}_j} = C_{N,j} \cdot W_{PAH_j}^4, \quad (2.136)$$

Blanquart and Pitsch [87] estimated the constant $C_{N,j}$ by comparing the profiles of several PAH species with experimental measurements in a single premixed benzene flame [155], and provided a efficiency values for various PAHs that are listed in Table 2.2. The rate dimer of coalescence is expressed as:

$$w_{\text{dim}_j} = k_{inc_j} [\text{Dimer}_j][\text{Dimer}_j] \quad (2.137)$$

Similarly, the rate of adsorption of dimers on soot particles is obtained as:

$$w_{ads_j}^i = k_{ads_j}^i [\text{Soot}]^i [\text{Dimer}_j] \quad (2.138)$$

Assuming fast dimer consumption leads to the steady-state concentration of the dimer that can be determined by solving a quadratic equation as:

$$a_{inc_j} [\text{dimer}]^2 + b_{ads_j} [\text{dimer}] = \omega_{\text{dim},j} \quad (2.139)$$

$$[\text{Dimer}_j] = \begin{cases} \frac{-b_{ads_j} + \sqrt{\Delta_j}}{2a_{inc_j}}, & \text{if } \Delta_j \geq 0 \\ 0 & \text{if } \Delta_j < 0 \end{cases} \quad (2.140)$$

$$\Delta_j = b_{ads_j}^2 - 4a_{inc_j}\omega_{\text{dim},j} \quad (2.141)$$

where $a_{inc_j} = k_{inc_j}$ and b_{ads_j} is calculated by summing the adsorption rate of dimer for all sections and dividing it by the dimer concentration.

$$b_{ads_j} = \sum_{i=1}^{n_{sec}} k_{ads_j}^i [\text{Soot}]^i \quad (2.142)$$

After determining the concentration of each dimer, the contribution of inception and PAH adsorption to source terms of tracked soot variables can be calculated similar to previous inception models.

$$I_{N,inc} = \frac{1}{\rho} \sum_{j=1}^{n_{PAH}} 4\omega_{inc_j} n_{PAH_j,C}, \quad (2.143)$$

$$I_{C_{tot},inc} = \frac{1}{\rho} \sum_{j=1}^{n_{PAH}} 4\omega_{inc_j} n_{PAH_j,C}, \quad (2.144)$$

$$I_{H_{tot},inc} = \frac{1}{\rho} \sum_{j=1}^{n_{PAH}} 4\omega_{inc_j} (n_{PAH_j,H} - 2), \quad (2.145)$$

$$I_{C_{tot},ads}^i = \frac{1}{\rho} \sum_{i=1}^{n_{PAH}} 2\omega_{ads_j}^i n_{C,PAH_j}, \quad (2.146)$$

$$I_{C_{tot},ads}^i = \frac{1}{\rho} \sum_{i=1}^{n_{PAH}} 2\omega_{ads_j}^i (n_{H,PAH_j} - 2). \quad (2.147)$$

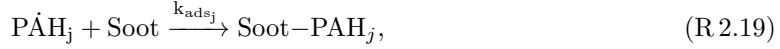
The rate of removal of PAHs and release of H₂ due to inception and PAH adsorption is calculated as:

$$\left(\frac{d[\text{PAH}_j]}{dt} \right)_{inc} = -4 \sum_{k=1}^{n_{PAH}} w_{inc_j} - 2 \sum_{i=1}^{n_{sec}} w_{ads_j}^i. \quad (2.148)$$

$$\left(\frac{d[\text{H}_2]}{dt} \right)_{inc} = 2 \sum_{i=1}^{n_{sec}} w_{ads_j}^i. \quad (2.149)$$

2.6.4 E-Bridge Formation

The E-Bridge Formation was originally proposed by Frenklach and Mebel [25] to describe soot inception using a HACA-like scheme that starts with dehydrogenation of PAH monomers, often pyrene, which forms the monomer radicals and continues with sequential addition of the radicals to PAHs that form dimers, trimers and larger polymers until the PAH structure reaches the mass threshold and the clustering process becomes irreversible. Here, a modified version of EBridge formation model is used where dimers are considered as incipient soot, and monomer radical are adsorbed on soot agglomerates. This PAH growth model is described using the following set of pathways:



The rate constants of Reactions (R 2.16)&(R 2.17) are listed in Table 2.3 while those of dimer production and adsorption are calculated based on Equations (2.94)&(2.100), respectively. For both steps, it is assumed the all collisions are successful i.e. 100% collision efficiency for radical-monomer and radical-soot.

$$k_{inc_j} = \beta_{jj,PAH} \cdot Av, \quad (2.150)$$

$$k_{ads_j}^i = \beta_{ads_j}^i \cdot Av, \quad (2.151)$$

The rate of dimer formation and adsorption is calculated as:

$$w_{dim_j} = k_{inc_j} [\text{PAH}_j][\dot{\text{PAH}}_j] \quad (2.152)$$

$$w_{ads_j}^i = k_{ads_j}^i [\text{Soot}]^i [\dot{\text{PAH}}_j] \quad (2.153)$$

Table 2.3: Rate coefficients for the monomer de-/hydrogenation reaction of E-bridge formation in Arrhenius form $k = AT^n \cdot e^{-E/RT}$ [25]

Reaction	A	$\left[\frac{\text{m}^3}{\text{mol} \cdot \text{s}} \right]$	n	$\frac{E}{R} [\text{K}]$
(R 2.16)	f	$98 \times n_{C,\text{PAH}_j}$	1.8	7,563.519
	r	1.6×10^{-2}	2.63	2145.346
(R 2.17)	f	4.8658×10^7	0.13	0.0

The calculations of rate of inception and PAH adsorption from PAH_j requires the concentration of corresponding monomer radical that can be determined by applying the steady-state assumption for $\dot{\text{PAH}}_j$.

$$\frac{d[\dot{\text{PAH}}_j]}{dt} = 0$$

$$k_{f,d_j}[\text{PAH}_j][\text{H}] - k_{r,d_j}[\dot{\text{PAH}}_j][\text{H}_2] - k_{f,h_j}[\dot{\text{PAH}}_j][\text{H}] - k_{inc_j}[\dot{\text{PAH}}_j]^2 - \sum_{i=1}^{n_{sec}} k_{ads_j}^i [\dot{\text{PAH}}_j][\text{Soot}]^i = 0$$

The above equations can be rearranged as a quadratic equation similar to the dimer coalescence.

$$a_{inc_j}[\dot{\text{PAH}}_j]^2 + b_{ads_j}[\dot{\text{PAH}}_j] + c_j = 0, \quad (2.154)$$

$$a_{inc_j} = k_{f,d_j} \quad (2.155)$$

$$b_{ads_j} = k_{r,d_j}[\text{H}_2] + k_{f,h_j}[\text{H}] + \sum_{i=1}^{n_{sec}} k_{ads_j}^i [\text{Soot}]^i \quad (2.156)$$

$$c_{inc_j} = k_{f,d_j}[\text{PAH}_j][\text{H}] \quad (2.157)$$

Finally, solving the quadratic equation for each PAH results in concentration of the radical using the following equation as:

$$[\dot{\text{PAH}}_j] = \begin{cases} \frac{-b_{ads_j} + \sqrt{\Delta_j}}{2a_{inc_j}}, & \text{if } \Delta_j \geq 0 \\ 0 & \text{if } \Delta_j < 0 \end{cases} \quad (2.158)$$

$$\Delta_j = b_{ads_j}^2 - 4a_{inc_j}c_j \quad (2.159)$$

The contribution of inception and adsorption to the partial source terms for E-Bridge formation can be written as:

$$I_{N,inc} = \frac{1}{\rho} \sum_{j=1}^{n_{PAH}} 2\omega_{inc_j} n_{PAH_j,C}, \quad (2.160)$$

$$I_{C_{tot},inc} = \frac{1}{\rho} \sum_{j=1}^{n_{PAH}} 2\omega_{inc_j} n_{PAH_j,C}, \quad (2.161)$$

$$I_{H_{tot},inc} = \frac{1}{\rho} \sum_{j=1}^{n_{PAH}} 2\omega_{inc_j} (n_{PAH_j,H} - 2), \quad (2.162)$$

$$I_{C_{tot},ads}^i = \frac{1}{\rho} \sum_{j=1}^{n_{PAH}} \omega_{ads_j}^i n_{C,PAH_j}, \quad (2.163)$$

$$I_{C_{tot},ads}^i = \frac{1}{\rho} \sum_{i=1}^{n_{PAH}} \omega_{ads_j}^i (n_{H,PAH_j} - 2). \quad (2.164)$$

The rate of removal of each PAH involved in soot inception and PAH adsorption and release of H₂ to the gas mixture can be expressed as:

$$\left(\frac{d[\text{PAH}_j]}{dt} \right)_{inc} = -2 \sum_{k=1}^{n_{PAH}} w_{inc_j} - \sum_{i=1}^{n_{sec}} w_{ads_j}^i. \quad (2.165)$$

$$\left(\frac{d[\text{H}_2]}{dt} \right)_{inc} = \sum_{i=1}^{n_{sec}} w_{ads_j}^i. \quad (2.166)$$

2.7 Gas scrubbing rates

The rate of production/destruction of species involved in soot formation must be taken into account to preserve the mass and energy balance in reactive system. In order to do that, the production rate of gaseous species calculated by Cantera must be corrected for the rate of release/consumption due to PAH growth and surface reaction models. PAHs participate in inception and PAH adsorption processes.

$$\left(\frac{d[\text{PAH}_j]}{dt} \right)_{tot} = \left(\frac{d[\text{PAH}_j]}{dt} \right)_{gas} + \left(\frac{d[\text{PAH}_j]}{dt} \right)_{inc} + \left(\frac{d[\text{PAH}_j]}{dt} \right)_{ads}. \quad (2.167)$$

H₂ is released to the gas mixture due to inception, PAH adsorption as well as oxidation.

$$\left(\frac{d[\text{H}_2]}{dt} \right)_{tot} = \left(\frac{d[\text{H}_2]}{dt} \right)_{gas} + \left(\frac{d[\text{H}_2]}{dt} \right)_{inc} + \left(\frac{d[\text{H}_2]}{dt} \right)_{ads} + \left(\frac{d[\text{H}_2]}{dt} \right)_{ox}. \quad (2.168)$$

Surface growth consumes C₂H₂ and adds H₂ to the gas mixture.

$$\left(\frac{d[\text{C}_2\text{H}_2]}{dt} \right)_{tot} = \left(\frac{d[\text{C}_2\text{H}_2]}{dt} \right)_{gas} + \left(\frac{d[\text{C}_2\text{H}_2]}{dt} \right)_{gr}. \quad (2.169)$$

$$\left(\frac{d[\text{H}]}{dt} \right)_{tot} = \left(\frac{d[\text{H}]}{dt} \right)_{gas} + \left(\frac{d[\text{H}]}{dt} \right)_{gr}. \quad (2.170)$$

Oxidation uses O₂ and OH to remove carbon from soot particles and generates H₂ and CO.

$$\left(\frac{d[\text{CO}]}{dt} \right)_{tot} = \left(\frac{d[\text{CO}]}{dt} \right)_{gas} + \left(\frac{d[\text{CO}]}{dt} \right)_{ox}. \quad (2.171)$$

$$\left(\frac{d[\text{O}_2]}{dt} \right)_{tot} = \left(\frac{d[\text{O}_2]}{dt} \right)_{gas} + \left(\frac{d[\text{O}_2]}{dt} \right)_{ox}. \quad (2.172)$$

$$\left(\frac{d[\text{OH}]}{dt} \right)_{tot} = \left(\frac{d[\text{OH}]}{dt} \right)_{gas} + \left(\frac{d[\text{OH}]}{dt} \right)_{ox}. \quad (2.173)$$

Chapter 3

Results

3.1 Validation

3.1.1 Collision Frequency

The collision frequency function determines the rate at which two particles collide resulting in the reduction of total number of particles and increase in their average size. In the absence of strong flow shear or external forces, Brownian motion is the main driving force for particle coagulation. As explained in Sections 2.4.4.1 & 2.4.5.1, omnisoot employs harmonic mean and Fuchs interpolations to calculate collision frequency of agglomerates from free-molecular to continuum regimes based on gas mean free path, and particle morphology.

The test case for validation of collision frequency is based on DEM simulation of 2000 monodisperse spherical particles with the density of 2200 kg/m^3 in a cubic cell with the constant temperature of 298 K and pressure of 1 atm [156]. Figure 3.1 depicts the collision frequency plotted against Knudsen number ($\text{Kn} = 2\lambda/d_m$) obtained by omnisoot using harmonic mean (red solid line) and Fuchs interpolation (green dashed line) and DEM results of Goudeli et al. [156]. The Fuchs interpretation perfectly matches DEM data over the free-molecular ($\text{Kn} < 10$) to the continuum ($\text{Kn} > 10$) range. However, harmonic mean slightly underpredicts the collision frequency in the transition regime ($0.1 \leq \text{Kn} \leq 10$) with relative errors less than 16%.

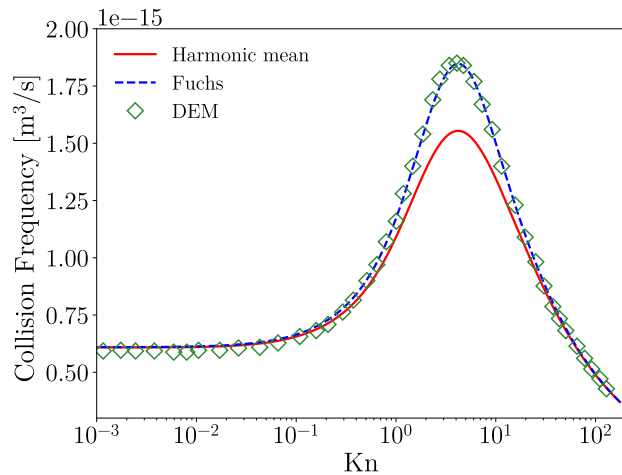


Figure 3.1: The comparison of collision frequency, β , obtained by omnisoot using harmonic mean (red solid line) and Fuchs interpolation (green dashed line) with DEM results (symbols) [156]

3.1.2 Coagulation

This test case was designed and conducted to validate the coagulation sub-unit of both particle dynamics models, MPBM and SPBM, by comparing the results of omnisoott with those of DEM [157]. The constant volume reactor was used for this test case, but it will be applicable to other reactors and flame models as long as the particle residence time matches with the values obtained by DEM. An adiabatic reactor with the volume of 1m^3 is initialized with 2.6261×10^{18} spherical particles that are 2 nm in diameter. The initial conditions are indicated in Table 3.1. The particles are allowed to coagulate in the free molecular regime and grow in size while inception, PAH adsorption and surface growth are disabled. Figure 3.3 demonstrates the number density of agglomerates (N_{agg}) and primary particles (N_{pri}), and mobility (d_m) and gyration (d_m) diameters of particle obtained by omnisoott that are in good agreement with DEM results. N_{pri} is conserved during coagulation resulting in identical flat lines for both particle dynamics models, but N_{agg} declines over time with the higher decay rate for SPBM because it accounts for the polydispersity of agglomerates that results in larger collision frequency compared to MPBM. Stronger collision rate leads to agglomerates with larger the mobility and gyrations diameters.

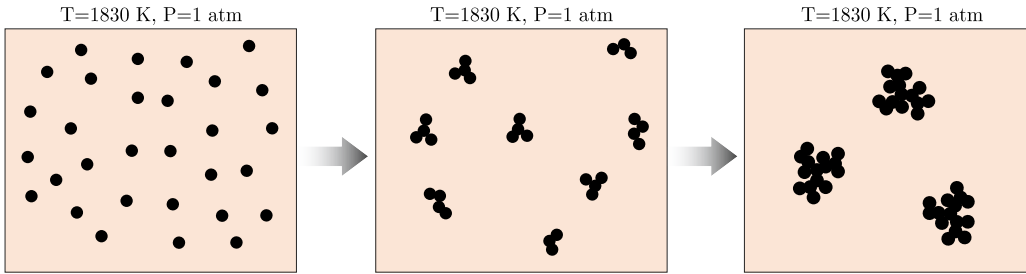


Figure 3.2: The schematic of agglomeration process in the coagulation test cases where initially spherical particle collide and form agglomerate

MPBM model does resolve PSD based on the assumption that at high concentrations particles reach their SPSD, and their evolution can be described by tracking average properties. In contrast, SPBM tracks the number concentration of particles in fixed size sections that can be used to construct PSD and calculate mean and spread of size distribution of particle during coagulation. The left pane of Figure 3.4 shows the standard deviation of mobility diameter, σ_g in a close agreement with DEM results. Initially, σ_g is 1 indicating a monodisperse population at the beginning of the simulation, and it finally reaches 2.03 that is the signature standard deviation of the free molecular regime [158]. The right pane of Figure 3.4 demonstrates the evolution of non-dimensional PSD from $t=1\text{ ms}$ to 677 ms . The PSD is shown in terms of the normalized concentration, $\Psi = \bar{v}n_{\text{agg}}(v, t)/N_{\text{agg},\text{inf}}$ and dimensionless volume, $\eta = v/\bar{v}$, where $n_{\text{agg}}(v, t)$ is the size distribution function of agglomerate, v particle volume, \bar{v} mean particle volume, $N_{\text{agg},\text{inf}}$ total number concentration of agglomerates. For short residence times, $t \approx 4\text{ ms}$, the PSD resembles a half bell curve because the majority of particles has sizes close to $d_0 = 2\text{nm}$ with the average volume close to the minimum volume, so particle with $\eta \approx 1$ has the largest concentration. As particles growth by coagulation, the PSD rapidly transitions to a full bell-curve ($t \geq 22\text{ms}$) and does not change for longer residence times, $t \geq 447\text{ms}$ marking the attainment of SPSD. This confirms the ability of SPBM in omnisoott to capture SPSD for soot agglomerates as a signature of Brownian-driven particle coagulation.

3.1.3 Constant Volume Reactor

The pyrolysis of 30% CH_4 diluted in N_2 with the initial temperature and pressure of 2455 K and 3.47 atm, respectively, was simulated using the constant volume reactor model in the residence time of 40 ms. The simulation was performed for 8 cases. The combination of available PAH growth and particle dynamics models leads to eight different cases that were simulated to ensure the conservation of mass and energy. Here, we focus on the total elemental balance of carbon and

Table 3.1: The simulations conditions of the coagulation test case [157]

Property	Value
Composition	CH ₄ :0.425, O ₂ :0.435, N ₂ :0.14
T	1830 K
P	1 atm
N _{agg} ¹	3.514×10^{-5} mol/kg
N _{pri} ¹	3.514×10^{-5} mol/kg
d _p ¹	2 nm

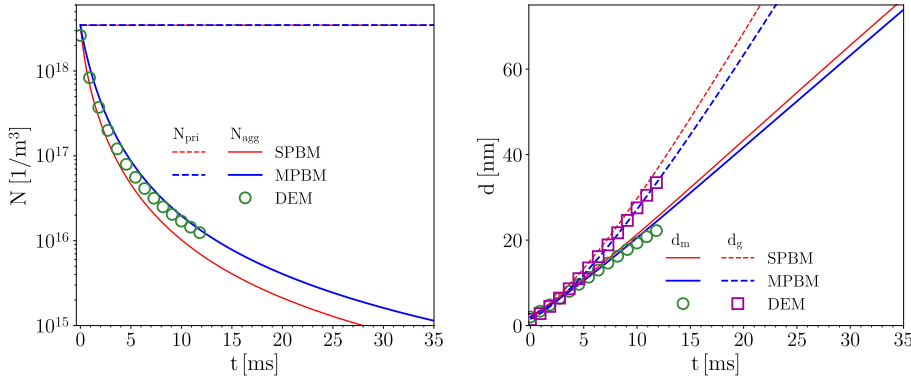
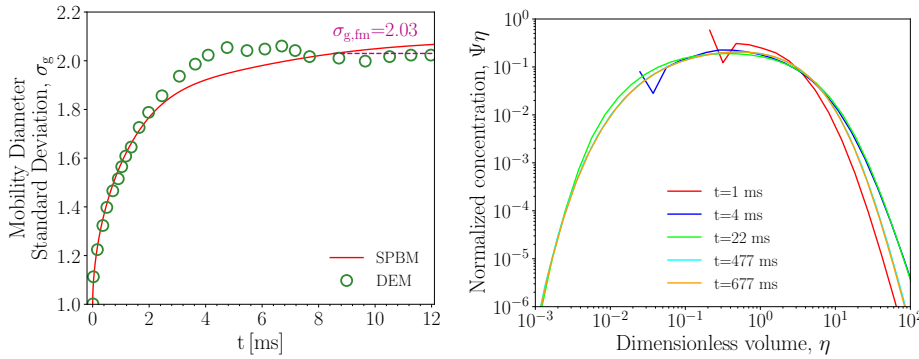


Figure 3.3: The total number concentration of agglomerates and primary particles (left pane), and mobility and gyration diameter (right pane) obtained with omnisoot using MPBM and SPBM that are in close agreement with the DEM results [157] indicating the validation of coagulation sub-model

Figure 3.4: The standard deviation of mobility diameter, σ_g obtained with SPBM in close agreement with DEM results [157] (left pane) that reaches $\sigma_{g,\text{fm}} = 2.03$ characteristic of the free molecular regime [158]; the particle size distribution (normalized number concentration of agglomerates is plotted against non-dimensional volume in the right pane) at different residence times that overlaps after initial transient phase marking the attainment of self-preserving size distribution

hydrogen because they are involved in soot processes. Figure 3.5 demonstrates the relative error of total carbon, hydrogen and energy of system for different PAH growth and particle dynamics models in the constant volume that falls below 10^{-10} for all parameters confirming the validity of model in satisfying the mass and energy balance in the constant volume reactor using all models.

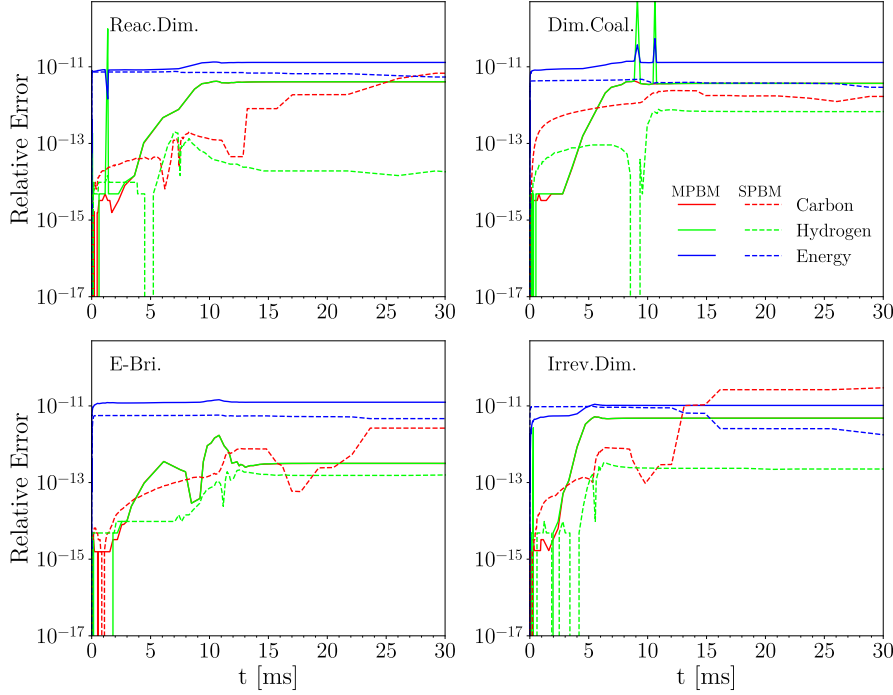


Figure 3.5: The relative error of total carbon (red line) and hydrogen (green line), and total internal energy residual of gas and soot (blue line) plotted against residence time during pyrolysis of 30% $\text{CH}_4\text{-N}_2$ at 2455 K and 3.47 atm in the constant volume reactor simulated using reactive dimerization, dimer coalescence, e-bridge formation and irreversible dimerization along with MPBM (solid line) and SPBM (dashed line)

3.1.4 Plug Flow Reactor

Methane pyrolysis in an adiabatic flow reactor is used to check elemental carbon and hydrogen, and energy balance in the PFR model. The inlet flow enters the reactor at the composition of 30% CH_4 diluted in N_2 , and $T=2100$ K and $P=1$ atm. Figure 3.6 shows the residual of total elemental carbon and hydrogen, and energy up to 40 cm of the reactor length using all PAH growth and particle dynamics model. The fluctuations in residuals start at the beginning of the reactor by pyrolysis of CH_4 leading to the formation of intermediate species such as C_2H_2 and PAHs. This initiates soot inception of surface growth affecting the gas chemistry and energy that ends near $x=10$ cm, and then the coagulation of particles is dominant with no affect on mass and energy of particles.

3.2 Soot yield and morphology during methane pyrolysis in shock-tubes

In this section, we focus on simulation of soot formation in shock-tubes using the constant volume reactor of omnisoott, and compare species mole fraction and soot yield and morphology with benchmark measurements. Methane (CH_4) pyrolysis in plasma reactors is an emerging alternative production method with distinct advantages over flame-based methods [159] in terms of emissions and process

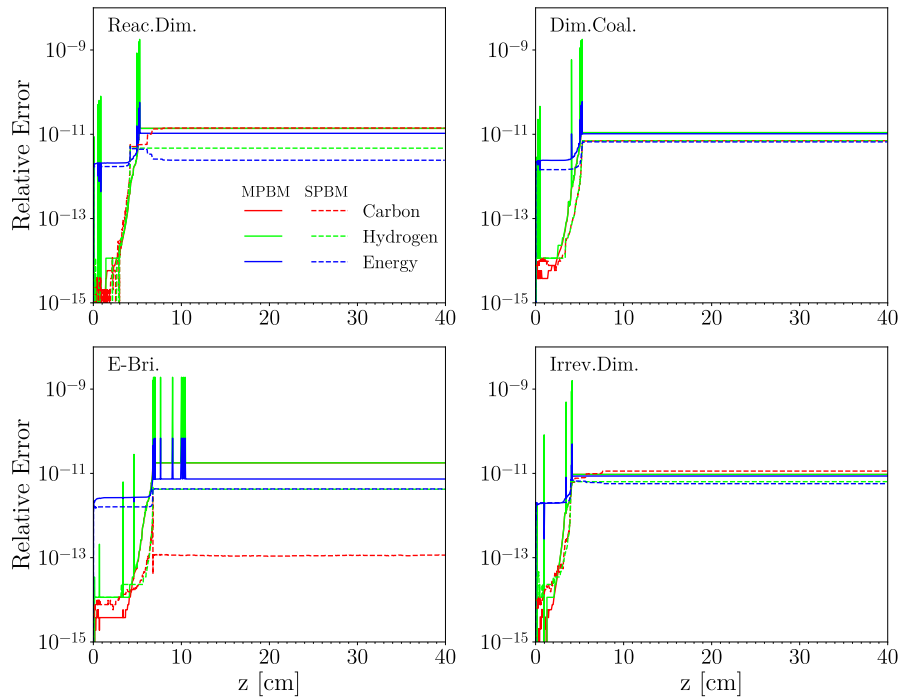


Figure 3.6: The relative error of total carbon (red line) and hydrogen (green line) mass, and total internal energy residual of gas and soot (blue line) plotted against reactor length (cm) in the adiabatic flow reactor during pyrolysis of 30% $\text{CH}_4\text{-N}_2$ at 2100 K and 1 atm simulated using reactive dimerization , dimer coalescence, e-bridge formation and irreversible dimerization along with MPBM (solid line) and SPBM (dashed line)

control [10]. Achieving specific grades of CB for different target applications requires a good control over CB properties such as its morphology (quantified by primary particle, d_p and mobility diameter, d_m), composition (elemental carbon to hydrogen ratio), specific surface area (inversely proportional to d_p) and internal nanostructure (composed of aligned graphitic shell and disordered core). However, this is challenging because of the complexity of CB inception and mass growth processes and its coupling with gas phase chemistry, dependence on local temperature and pressure, and short time scales of CB inception and growth [36]. Therefore, robust particle dynamics models coupled with detailed chemical mechanisms are essential to better understand methane-to-CB conversion process under different feedstock compositions, and temperature and pressure time-histories.

While methane combustion has been extensively studied [160] due to the need for a detailed chemical description of natural gas combustion, the formation of carbonaceous particles such as soot and CB from methane pyrolysis are not well understood yet. Significant differences exist between reaction mechanisms in prediction of CH₄ and intermediate species such as C₂H₂, and C₂H₄ in flame and reactors [160]. These uncertainties are amplified for polycyclic aromatic hydrocarbons (PAH) that are known as main precursors because of their low concentrations and complexity of pathways. Moreover, the exact pathways of CB inception and surface growth have not been identified yet. Methane flames have been studied to estimate the inception mass flux at low-pressure with equivalence ratio of 1.95 in a near-sooting condition [42]. Similarly, methane flames have been used to study the effect of H₂ on addition on inception flux, and pressure on particle morphology [161]. Although flame data is available, there is a lack of such datasets in shock tubes. Kinetic studies and measurements of soot inception and growth have certain advantages in shock tubes over flames due to the uniform and instant heating of the mixture behind the reflected shock to the desired temperature and pressure as well as the absence of complicating factors such as diffusion and mixing. The shock-wave propagation and reflection creates nearly isothermal and isobaric conditions create an ideal environment for kinetic studies of pyrolysis, pathways and soot inception and growth. However, these conditions are limited to short residence times usually 1-3 ms, so they can only be used to study early stages of soot formation such as inception and surface growth, and not for processes occurring at longer residence times such as coagulation, graphitization and carbonization.

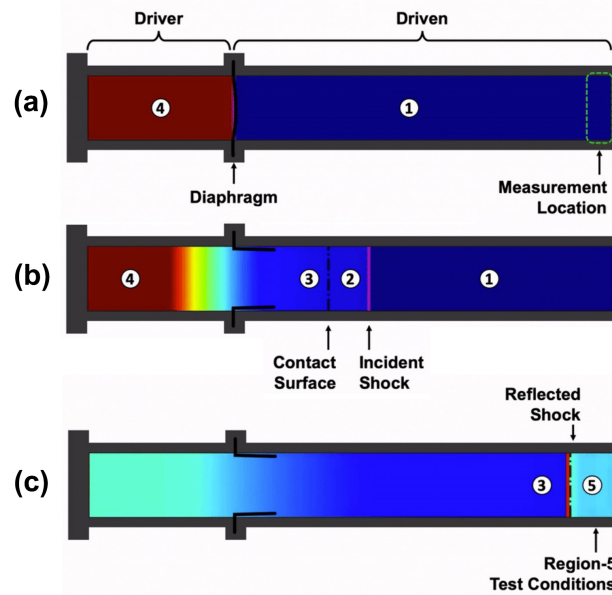


Figure 3.7: Different stages of shock wave propagation during shock-tube test from (a) before rupture of diaphragm leading to (b) propagation of incident shock towards the end of shock-tube and (c) its reflection from the end wall that increases pressure and temperature of test gas (Reprinted from Ref. [162])

Different stages of shock-wave propagation is illustrated in Fig.3.7. A shock tube consists of a driver and a driven section separated by a single-use diaphragm in between. The driver section contains usually an inert gas with a low molecular weight such as He, and the driven section is filled with the studied test gas. The driver section is pressurized to the desired pressure until the rupture of the diaphragm that puts the two gas regions with a large pressure difference in direct contact. This creates a shock wave that propagates through the driven section causing a pressure and temperature jump in the test gas.

After reaching the end wall, the shock wave reflects back towards the driver end of the shock tube resulting in a secondary compression and heating of the mixture, and ultimately stagnating the test gas. In nearly $10 \mu\text{s}$, this shock-heating process can bring the test gas from room-temperature to temperatures upwards of 10,000 K, and pressures more than 1000 atm.

The passage of reflected shock, referred to as region 5 with T_5 and P_5 , is reference for calculation of residence time and the starting point for simulations. The delay in appearance of soot (often quantified by a threshold for LII or extinction signals) is known as induction time, τ_{ind} . There has been a lot of research in the literature focused on induction time (similarly on ignition delay time) in shock tubes [163], but it is not the focus of this work. Instead, we mainly focus on species concentrations and soot characteristics during the pyrolysis of methane, at atmospheric and higher pressure which can be used for the design and optimization of carbon black in plasma reactors [159].

3.2.1 Experimental setup and data collection

The experiments on CH_4 pyrolysis were conducted by Hanson Research Group at Stanford University. The data has not been published yet (at the time of writing the document) and were provided through the collaboration with Monolith Materials and Stanford University.

Mole fraction time histories of methane (CH_4), acetylene (C_2H_2), and ethylene (C_2H_4) were captured using continuous wave (CW) laser absorption at $3.365 \mu\text{m}$, $2.998 \mu\text{m}$, and $10.532 \mu\text{m}$, respectively [164, 165, 166]. Soot volume fraction was measured using laser light extinction at $\lambda=633 \text{ nm}$ and 1064 nm with absorption function $E(m)$ of 0.174 and 0.203 [167], respectively. Additionally, soot samples were collected onto imaging stubs mounted in the shock-tube end-wall. A schematic of the experimental setup for laser diagnostics in the shock tube is shown in Fig. 3.8. Samples were extracted from the interior surface of the shock tube endwall after each experiment to allow for imaging and analysis of the particulates. TEM images were recorded with a FEI Tecnai G2 F20 X-TWIN microscope and Gatan SC200 camera for the test case of $P_5=4.5 \text{ atm}$ and $T_5=2217 \text{ K}$.

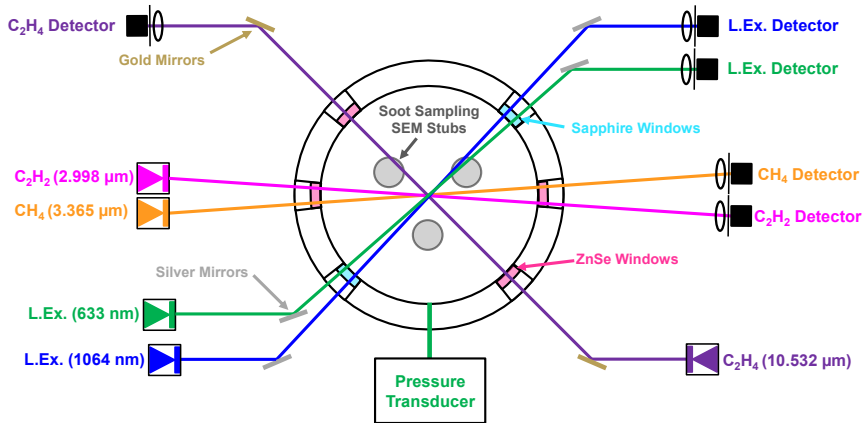


Figure 3.8: Layout of the laser diagnostics and shock-tube setup. Spatial and spectral filtering is employed to ensure high-quality absorbance measurements to infer species mole fractions and soot volume fraction. Soot samples are collected at the shock-tube endwall. All lasers are aligned in a plane 1 cm from the endwall

The first data set includes eight measurements with the fuel loading of 30% $\text{CH}_4\text{-Ar}$ at $P=4\pm0.5$

Table 3.2: The pressure, temperature and composition of simulation data points for 10% CH₄

	Datapoints							
	(1)	(2)	(3)	(4)	(5)	(6)	(7)	(8)
T [K]	1861	1917	2030	2155	2184	2313	2375	2455
P [atm]	4.12	3.74	3.56	3.93	3.62	3.58	3.75	3.47
Composition	CH ₄ : 0.3, Ar: 0.7							

atm in the temperature range of 1800-2500 K. Table 3.2 lists the process conditions including pressure, temperature and composition of all data points of 30% CH₄ pyrolysis.

The time history of CH₄, C₂H₄ and C₂H₂ mole fraction as well as soot yield and volume fraction were reported up to 0.5 ms. The constant volume reactor was used with all PAH growth and particle dynamics models. First, the performance of reaction mechanisms are assessed by comparing the mole fraction of species captured by laser diagnostics, CH₄, C₂H₄, and C₂H₂ with model predictions using Caltech [169], KAUST [160] and ABF [59] mechanisms. The analysis of simulation results showed that soot formation had negligible impact on temperature and the mole fraction of measured species (see Figs. B.1-B.3).

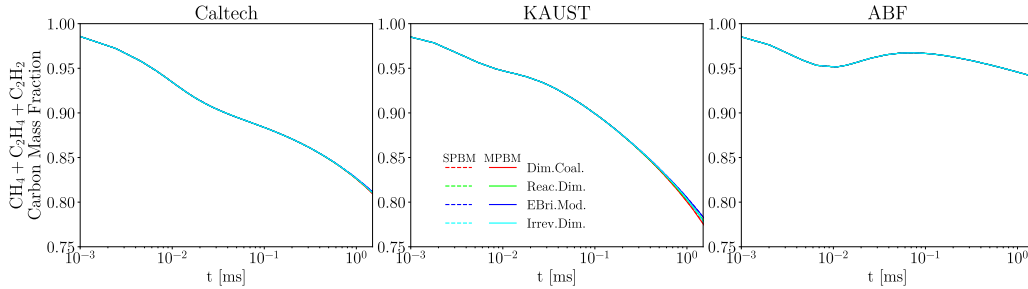


Figure 3.9: The time history of carbon mass fraction of CH₄, C₂H₄, and C₂H₂ of 30% CH₄ pyrolysis at T=2184 K and P=3.62 atm using Caltech, KAUST, and ABF mechanism and different PAH growth and particle dynamics models

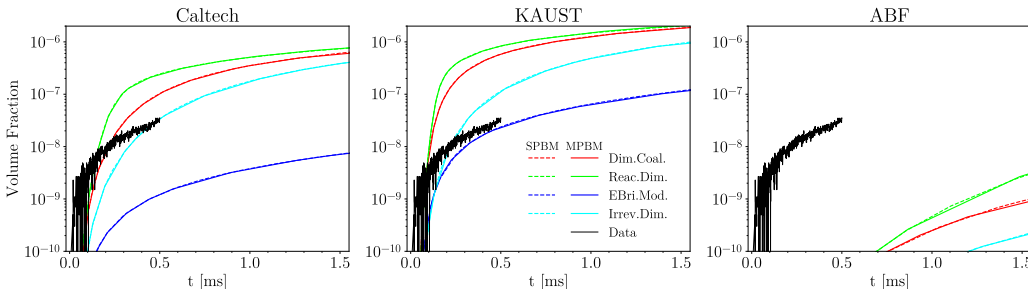


Figure 3.10: The time history of soot volume fraction of 30% CH₄ pyrolysis at T=2184 K and P=3.62 atm using Caltech, KAUST, and ABF mechanism and different PAH growth and particle dynamics models

Fig. 3.11 shows that the time variation of soot volume fraction in the temperature range of 1800-2500 K. The measurement data was not available (or too noisy) below T=2155 K due to lack of enough soot particle leading to weak extinction signal. In all cases with higher temperatures, EBridge Formation predicts the lowest volume fraction that interestingly are in close agreement

with the data. Reactive Dimerization and Dimer Coalescence yields the largest f_v nearly two orders of magnitude higher than the measurements that start with a rapid increase indicating a stronger inception rate leading to larger number concentration of particles that provide more surface area for surface growth via HACA. Shock tube temperature increases f_v with all PAH growth models over the 1.5 ms. Moreover, high temperature accelerates soot formation, which can be examined by comparing f_v at early stages of simulation. For example, no soot appears before $t=0.25$ ms i.e. $f_v < 10^{-10}$ at $T=1861$ K, but f_v approaches 10^{-6} at $T=2455$ K.

Fig.3.12 shows the time history of primary particle diameter, d_p at different temperatures. As expected, EBridge Formation and Irreversible Dimerization has the lowest d_p due to low soot mass growth rate leading to small f_v values. Although Dimer Coalescence and Reactive Dimerization generate close volume fraction values corresponding to similar soot mass, the latter predicts larger d_p indicating a lower number of N_{pri} . In other words, RD has lower inception rates and a stronger PAH adsorption rate compared to DC. The d_p by RD exhibits a noticeable sensitivity to particle dynamics model that grows with temperature. Both model predict the initial rapid rise in d_p . While MPBM predicts a gradual increase to final value, d_p by SPBM decreases for $T>2000$ K due to stronger inception rate by SPBM that generates particle with $d_p=2$ nm bringing down the average d_p .

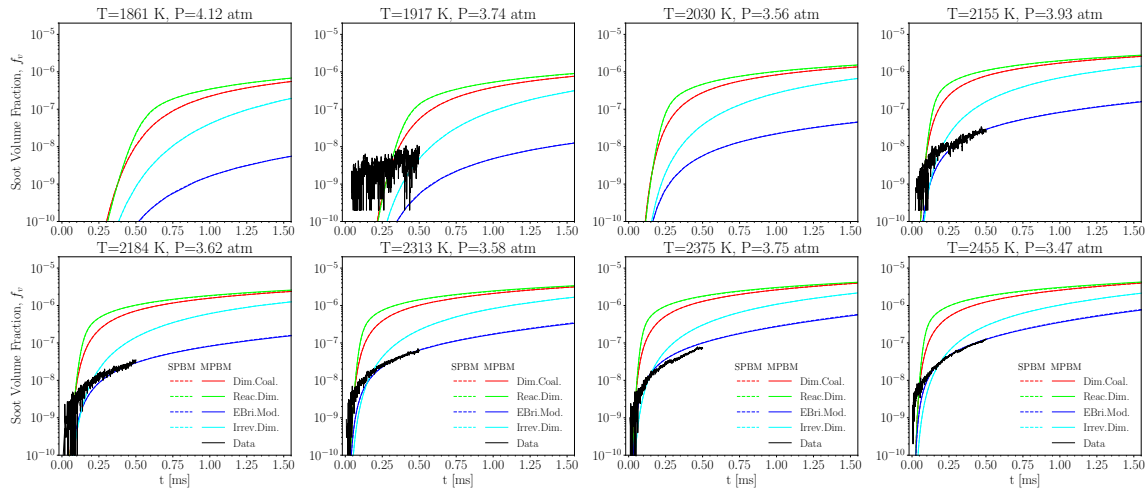


Figure 3.11: The time history of soot volume fraction of 30% CH_4 pyrolysis in the temperature range of 1800-2500 K and $P=4\pm0.5$ atm using KAUST mechanism and different PAH growth and particle dynamics models

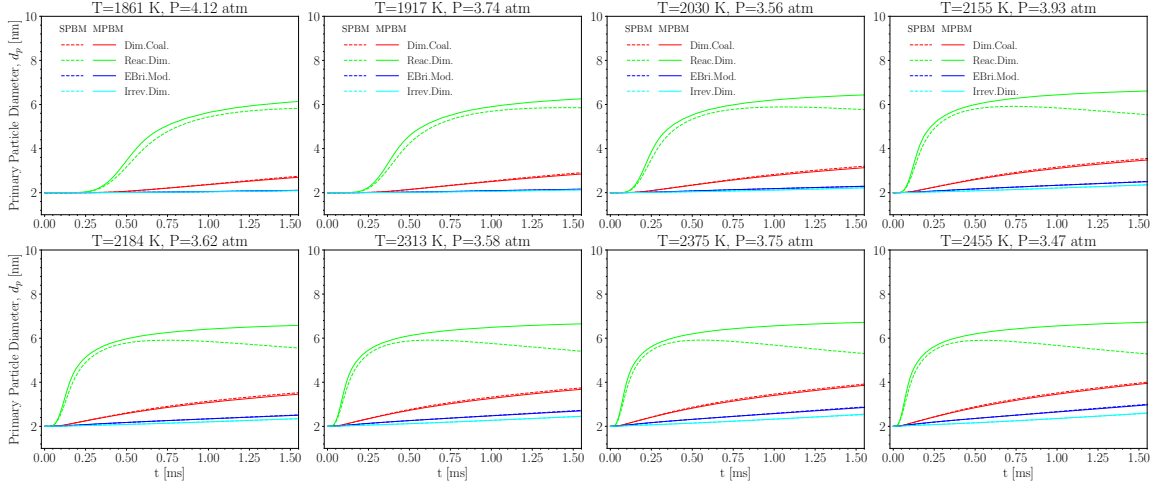
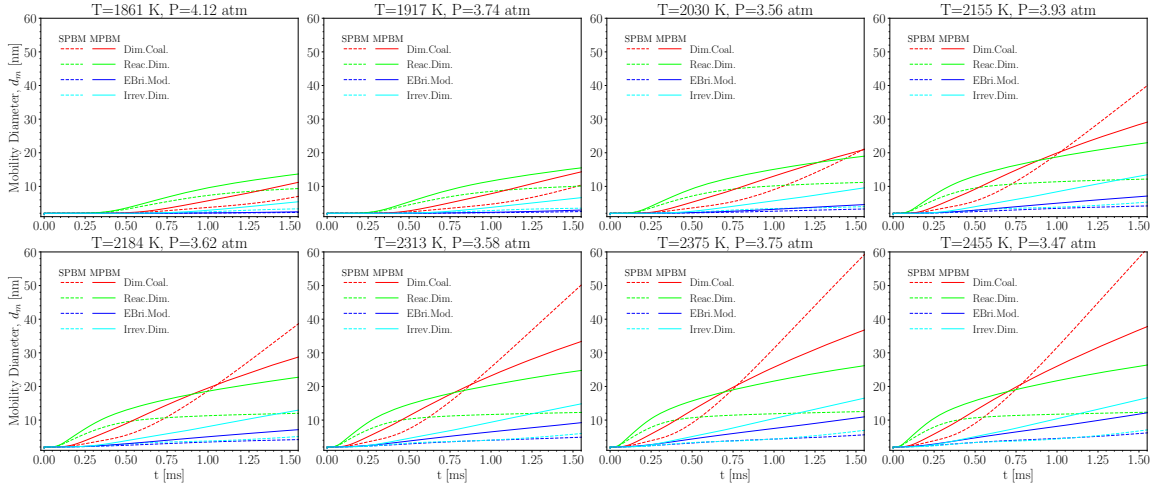
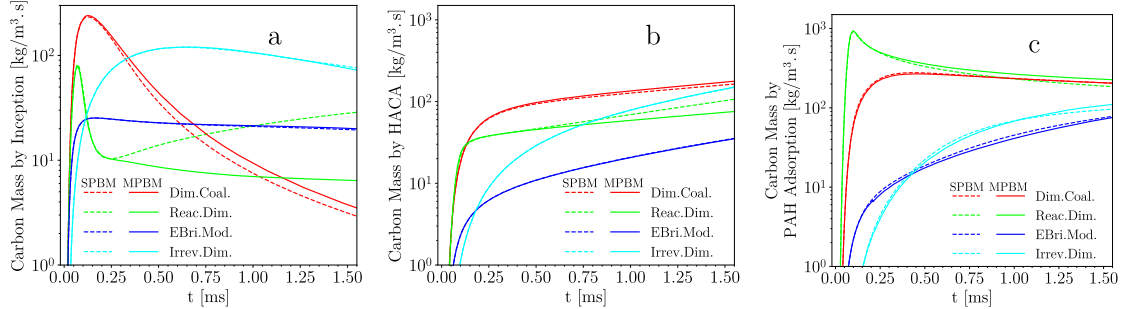


Figure 3.12: The time history of primary particle diameter, d_p of 30% CH_4 pyrolysis in the temperature range of 1800–2500 K and $P=4\pm0.5$ atm using KAUST mechanism and different PAH growth and particle dynamics models

Fig. 3.13 shows time histories d_m at different shock tube temperature. Similar to d_p , d_m increases over time and with shock tube temperature. The rise in d_m occurs faster. Initially, the generated agglomerates are small ($n_p \approx 1$), and d_m is close to d_p , so RD yield the highest d_m , but DC takes over and exceeds RD. Additionally, d_m predicted by MPBM is larger in the beginning of the simulation, but d_m predicted by SPBM rises faster at longer residence times. Fig. 3.14 shows the carbon mass growth rate by inception, HACA and PAH adsorption at $T=2455$ K and $P=3.47$ atm that explains the difference in the behavior of PAH growth and particle dynamics model in prediction of soot mass and morphology. The inception rate of RD (Fig. 3.14-a) rapidly rises reaching its peak values and quickly drops until $t=0.25$ ms when a bifurcation occurs. While the inception rate by MPBM gradually decreases, SPBM predicts an increasing rate of production of new particles leading to a smaller d_p . DC reaches the inception peak higher than other PAH growth models before $t=0.25$ ms creating more particles that causes larger d_m after coagulation becomes dominant. Such a high number concentration also leads to large HACA growth rates evident in Fig. 3.14-b. RD has the highest PAH adsorption rate with a peak near $t=0.1$ ms as opposed to other PAH growth models that causes the rapid drop in inception rate and higher soot mass gain rates leading to larger volume fraction (Fig. 3.10).

Table 3.3: The pressure, temperature and composition of simulation data points for 10% CH₄

	Datapoints							
	(1)	(2)	(3)	(4)	(5)	(6)	(7)	(8)
T [K]	1927	2074	2030	2348	1897	2085	2277	2406
P [atm]	1.37	1.27	1.22	1.13	4.49	4.85	4.43	3.89
Composition	CH ₄ : 0.1, CO ₂ : 0.01, Ar: 0.7							

Figure 3.13: The time history of mobility diameter, d_m of 30% CH₄ pyrolysis in the temperature range of 1800-2500 K and $P=4\pm 0.5$ atm using KAUST mechanism and different PAH growth and particle dynamics modelsFigure 3.14: The time history of carbon mass gained by inception(a), HACA (b), and PAH adsorption (c) of pyrolysis of 30% CH₄ at T=2455 K and P=3.47 atm using KAUST mechanism and different PAH growth and particle dynamics models

Now, we will examine the data from Stanford's group experiments on 10% CH₄ pyrolysis at $P=1\pm 0.5$ atm and 4 ± 0.5 atm in the temperature range of 1900-2500 K.

First, the mechanism comparison is conducted by simulating 10% CH₄ pyrolysis in a constant volume reactor. As shown before in Figs. B.2 and B.3, the particle dynamics and PAH growth models has minimal effect on the prediction of major small hydrocarbons. So, the mechanism comparison is only based on the combination of MPBM and RD to avoid clutter in graphs, and it is focused on two data points, T=2188 K, P=1.22 atm and T=2217 K, P=4.43 atm, each being

representative of atmospheric and high pressure cases, respectively. Fig. 3.15 shows CH₄ mole fraction for these data points predicted using KAUST, Caltech, and ABF mechanisms and compared with measurements. Similar to 30% CH₄ data set, KAUST and Caltech yield larger CH₄ conversion corresponding to a lower mole fraction. However, KAUST predictions are in close agreement for both data points, but ABF underestimates CH₄ conversion. As shown in Fig. 3.16, all mechanisms exhibit a similar behavior underestimating C₂H₂ mole fraction in the high pressure, but overestimating it for the atmospheric case. Fig. 3.17 compares soot volume fraction predicted by different mechanisms with light extinction measurements. As expected, ABF significantly underpredicts f_v due to low production rate of soot precursors (PAHs). Temperature analysis is not done for 10% CH₄ due to lack of measurements. KAUST mechanism is used for soot analysis as it predicts species and soot volume fraction close to the measurements.

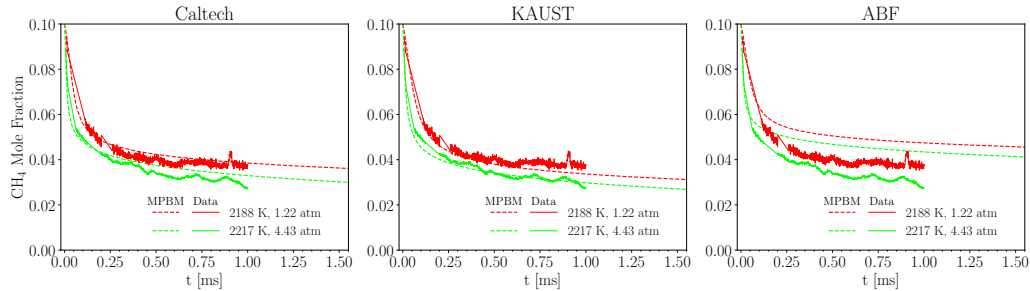


Figure 3.15: The time history of CH₄ mole fraction during 10% CH₄ pyrolysis at T=2188 K, P=1.22 atm (red line) and T=2217 K, P=4.43 atm (green line) using Caltech, KAUST, and ABF mechanism with MPBM and Reactive Dimerization

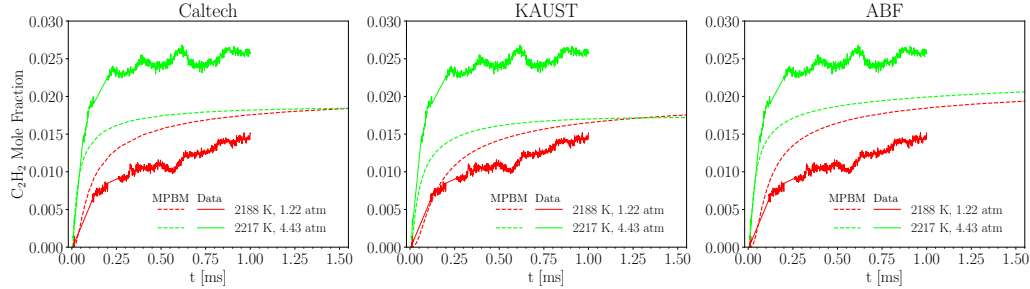


Figure 3.16: The time history of C₂H₂ mole fraction during 10% CH₄ pyrolysis at T=2188 K, P=1.22 atm (red line) and T=2217 K, P=4.43 atm (green line) using Caltech, KAUST, and ABF mechanism with MPBM and Reactive Dimerization

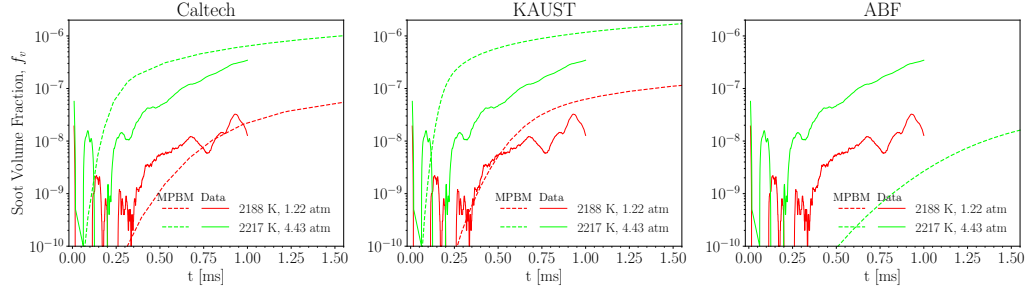


Figure 3.17: The time history of soot volume fraction, f_v of 10% CH_4 pyrolysis at $T=2188\text{ K}$, $P=1.22\text{ atm}$ (red line) and $T=2217\text{ K}$, $P=4.43\text{ atm}$ (green line) using Caltech, KAUST, and ABF mechanism with MPBM and Reactive Dimerization

Fig. 3.18 shows the evolution of soot volume fraction, f_v over simulation time in the temperature range (increasing from left to right) and (near) atmospheric and 4 atm pressure using KAUST mechanism. The upper and bottom rows correspond to 1 and 4 atm cases, and each column contains cases with similar temperatures. As expected, f_v is not affected by particle dynamics model, but it increases with shock tube temperature. The time of $f_v = 10^{-10}$ is shorter for 4 atm cases in each temperature indicating that pressure accelerates the soot formation. EF yields the most accurate f_v prediction compared with the data in 2000–2500 K of 4 atm cases. The final f_v predicted by increases by two orders of magnitude in 1900–2500 range at both pressures indicating more sensitivity of its inception rate to temperature.

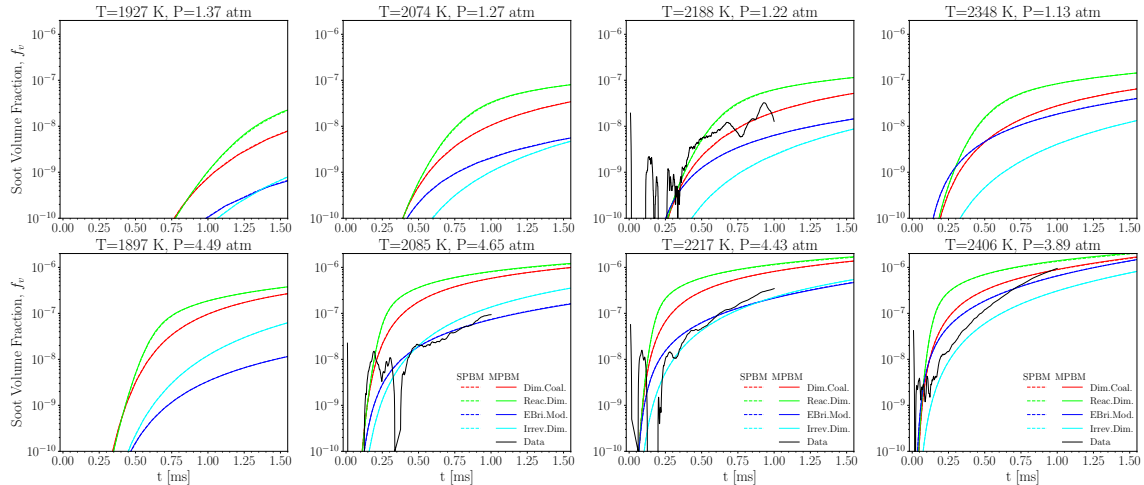


Figure 3.18: The time history of soot volume fraction of 10% CH_4 pyrolysis in the temperature range of 1900–2500 K (increasing from left to right) and $P=1\pm0.5$ (bottom row) and 4 ± 0.5 atm (upper row) using KAUST mechanism and different PAH growth and particle dynamics models

Figs. 3.19 and 3.20 show time history of d_p and d_m , respectively. The largest d_p is predicted by RD in all cases with final values near 6 nm, which is close to d_p of 10% CH_4 . However, d_m significantly decreased when feed-stock mole fraction is lowered from %30 to %10. Overall, the d_p increases slightly with both temperature and pressure. RD has the largest d_m in the entire temperature range of atmospheric cases, but at 4 atm d_m by DC quickly increases and exceed RD due to stronger inception rate leading to larger coagulation rate and agglomerates.

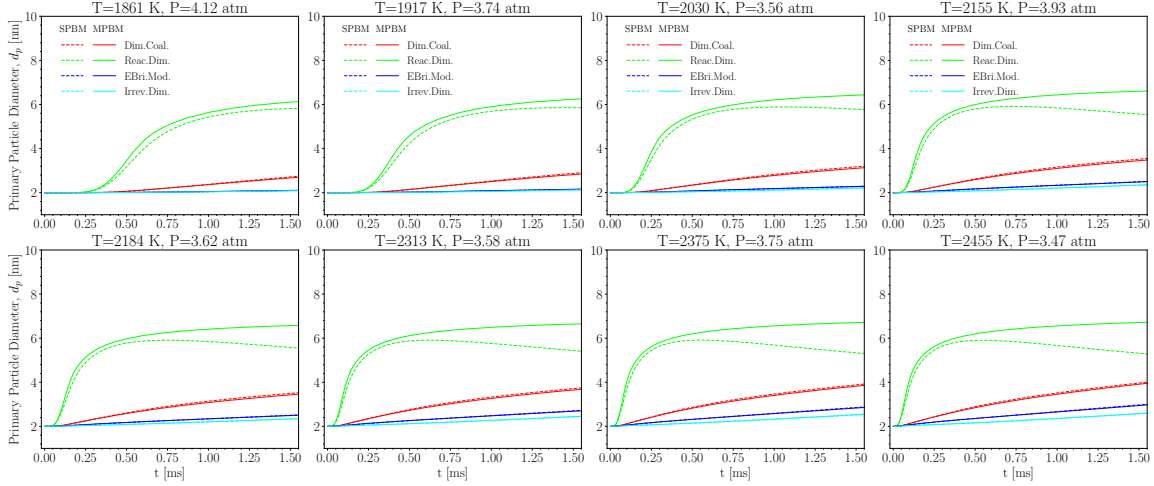


Figure 3.19: The time history of primary particle diameter, d_p of 30% CH_4 pyrolysis in the temperature range of 1800-2500 K and $P=1\pm 0.5$ and 4 ± 0.5 atm using KAUST mechanism and different PAH growth and particle dynamics models

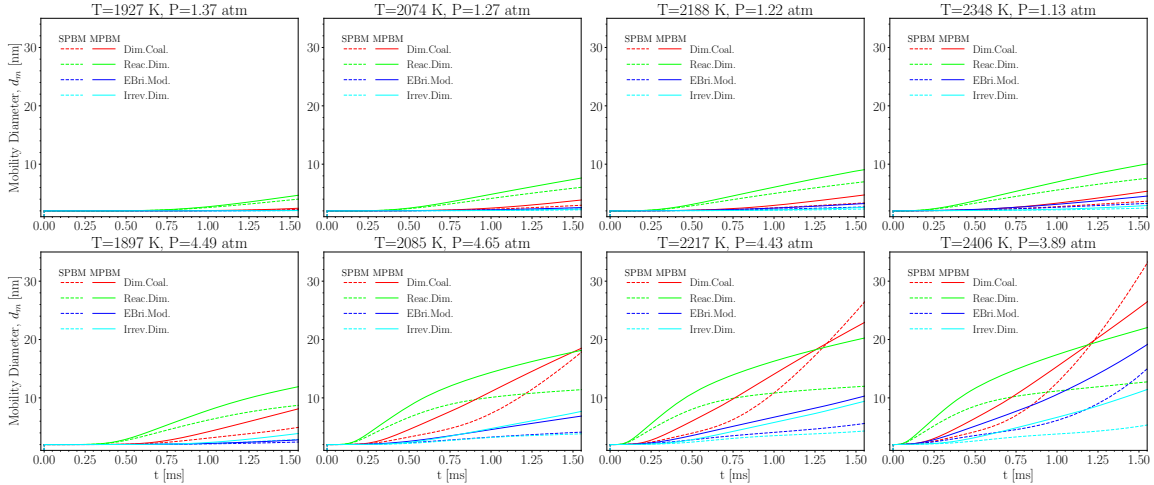


Figure 3.20: The time history of mobility diameter, d_m of 30% CH_4 pyrolysis in the temperature range of 1800-2500 K and $P=1\pm 0.5$ and 4 ± 0.5 atm using KAUST mechanism and different PAH growth and particle dynamics models

3.2.2 Analysis of soot morphology in methane pyrolysis shock-tube

The TEM images of 10% CH_4 at $T=2230$ K and $P=4.5$ atm data point provided by Stanford group are used to evaluate the performance of omnisoot in the prediction of d_p and d_m and compare the effect of different PAH growth and particle dynamics model on morphology. Soot particles are sampled from the end pipe wall and analyzed using a **** Transmission Electron Microscopy model **** over **** TEM grid. As reported by Stanford team, the expansion wave traverses the shock tube around 2 ms reducing the temperature to nearly **** K freezing the chemical reactions that contribute to the surface growth, but the coagulation might continue until the collection of particles leading to larger agglomerates. As a result, d_p estimated from the TEM images closely represents d_p of agglomerates at the end of process, but TEM-based d_m could be larger the actual values due to post expansion wave growth of particles. *atems* package [170] was used for characterizing soot aggregates in TEM images with different methods for evaluating the aggregate projected area,

perimeter, and primary particle diameter. It creates a binary map from the raw TEM image where white and black pixels represent the agglomerates and background, respectively, and feeds the map to a agglomerate segmentation algorithm to detect individual agglomerates. Fig.3.21 shows a sample from TEM images and segmented agglomerates from generated map.

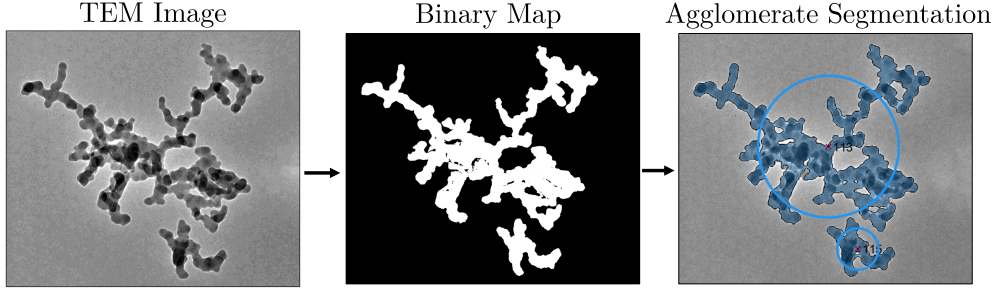


Figure 3.21: A TEM image provided by Stanford group (left pane) with the generated binary map (middle pane) and detected agglomerates using the segmentation algorithm (right pane)

We applied K-means clustering (KMC) [170] and otsu thresholding [171] to the same TEM images and compared the segmented agglomerates. A sample is shown in Fig.3.22 where KMC detected more agglomerates in the TEM image, but segments part of the background as agglomerates or divides a single agglomerate into multiple ones. On the other hand, otsu thresholding misses most of agglomerates in the TEM image. Here, the K-means clustering [170] is used and 171 agglomerates were detected. d_m was calculated from the diameter of equivalent projected area, A_a of each agglomerate. The pair correlation method (PCM) [171] was applied to compute the projected primary particle area, A_p and the mean d_p assuming that primary particle are almost uniform in size within each agglomerate. The number of primary particle per agglomerate is calculated as $n_p = A_a/A_p$ resulting in 6554 primary particles. The mean d_p of the entire samples is calculated as

$$\bar{d}_p = \frac{\sum_{\text{Aggs}} n_p d_p}{\sum_{\text{Aggs}} n_p} \quad (3.1)$$

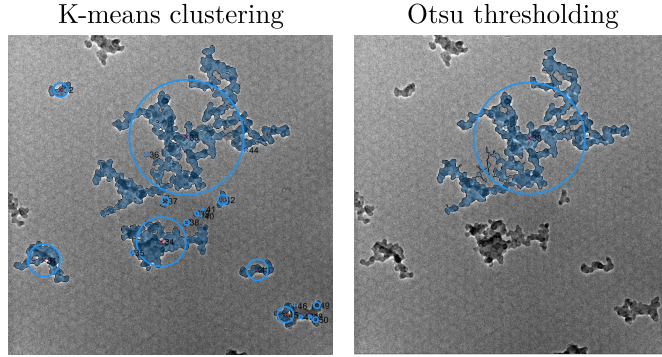


Figure 3.22: Agglomerates in single TEM image segmented by K-means clustering (left pane) and otsu thresholding (right pane)

Table 3.22 reports the arithmetic mean and median of mobility and primary particle diameter detected by atems from TEM images. The computed d_m and d_p will be compared with soot sampled from various sources. Soot morphology is mainly governed by coagulation leading to self-similar structures in which d_m scales with d_p and n_p . Olfert and Rogak [172] analyzed soot particles from flares [173], inverted burners [174], compression ignition engines [175] and other sources to support

Table 3.4: The morphological characteristics of agglomerates quantified by atems using KMC and PCM

Property	Arithmetic mean	Median
d_m [nm]	97	69
d_p [nm]	22	18

the external mixing hypothesis and related agglomerate size characterized by d_m to d_p using the following power-law:

$$d_p = d_{p,100} \left(\frac{d_m}{100\text{nm}} \right)^{D_{\text{TEM}}}, \quad (3.2)$$

where $d_{p,100}$ is the average primary particle diameter for a 100 nm aggregate, and D_{TEM} is the exponent. Both quantities were obtained by fitting Eq. (3.2) to soot sampled from different sources. the left pane of Fig 3.23 demonstrates the scatter plot of d_p against d_m is compared with power-law curves of Eq. (3.2) using two sets of prefactor and exponent values, i) $D_{\text{TEM}}=0.32$, $d_{p,100}=20.6$ nm, and ii) $D_{\text{TEM}}=0.39$, $d_{p,100}=20.2$ nm taken from average values reported in summary of fit parameters in Table 1 of Olfert and Rogak [172]. The power-law show a good agreement with quantities that d_p and d_m computed by atems can be good representative of soot agglomerates with minimal agglomerate overlap.

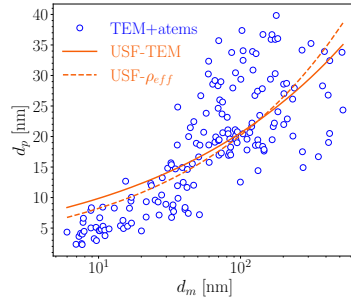


Figure 3.23: The d_m as a function of d_p from TEM image obtained by atems [170] (symbols) compared with the power law in Eq. (3.2)

Fig. 3.24 compares f_v from extinction measurement, d_p and d_m computed from TEM images with model predictions using KAUST mechanism, Monodisperse and different PAH growth models. The horizontal error bars denotes the uncertainty in residence time that TEM measurements correspond to. As reported by Stanford group, the expansion wave propagates near $t=2$ ms stopping the growth of d_p . Although the predicted soot mass, represented by volume fraction, is close even greater than measurements, but d_p is underpredicted by all PAH growth models. RD yields the largest d_p near 7 nm that is lower than d_p from TEM measurements by a factor of 3.

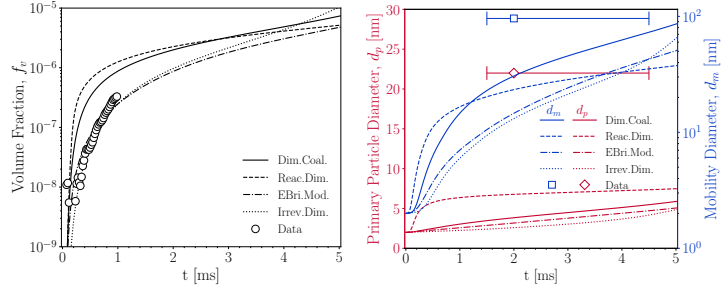


Figure 3.24: The volume fraction, f_v (left pane) and mobility, d_m (blue lines in right pane) and primary particle diameter, d_p (red lines in right pane) predicted by KAUST mechanism, MPBM, and different PAH growth models at $T=2230$ K, $P=4.5$ atm that corresponds to shock-tube conditions of TEM measurement

3.2.3 Sensitivity of yield and morphology to inception and surface growth rate

The underprediction of d_p by the model despite producing enough or even more soot carbon mass compared with the measurement motivated performing a sensitivity analysis for soot yield and morphology, especially because of uncertainties in inception and surface growth pathways and reaction rates associated with the PAH growth models integrated in omnisoot. It should be noted that this section is not aimed at a systematic sensitivity analysis with respect to all reaction rates, but rather to determine which sub-model has the dominant effect on yield and morphology that can be modified within the physical constraints to tailor these quantities to the desired values.

First, we examine the effect of HACA rates on yield and morphology of soot generated during 10% CH₄ at $T=2230$ K and $P=4.5$ atm in the Stanford shock-tube. To this purpose, the surface reactivity, α , in HACA formulation is modified by introducing a damping factor, ζ in Eq. (2.79) as:

$$\alpha^i = \tanh \left(\frac{12.56 - 0.00563 \cdot \zeta T}{\log_{10} \left(\frac{\rho_{soot} \cdot A_v}{W_{carbon}} \frac{\pi}{6} d_p^{i,3} \right)} - 1.38 + 0.00068 \cdot \zeta T \right). \quad (3.3)$$

Note that, there are many adjustable parameters in HACA scheme such as rate constants. ζ to modify α is intentionally chosen for a number of reasons. First, α was initially introduced as a tuning parameter as a function of local temperature and primary particle diameter to control surface growth rate, and it has been usually adjusted specifically for each flame [176, 132] to match the predicted volume fraction with the measurements. Second, the global empirical relation of Appel et al. [59] (used omnisoot to quantify α) developed by fitting parameters of α to minimize the prediction error of volume fraction for various premixed flames, and shock tubes generally have larger temperature ranges compared with premixed flames, which could excessively reduce surface reactivity and HACA growth rates. Finally, larger volume fractions (in the order of few ppm) were underpredicted by the global α relation (Fig. 9 of [59]). So, the low values of α in the shock tube at $T=2230$ K corresponding to process conditions of TEM measurements can contribute to underprediction of surface growth rates and d_p . We introduce ζ to reduce the damping effect of temperature on surface reactivity. Fig. 3.25 demonstrates the variation of α with temperature for $\zeta=0.6, 0.8, 1$ and primary particle diameter 2 and 6 nm. α decreases with temperature, and it is inversely proportional to ζ .

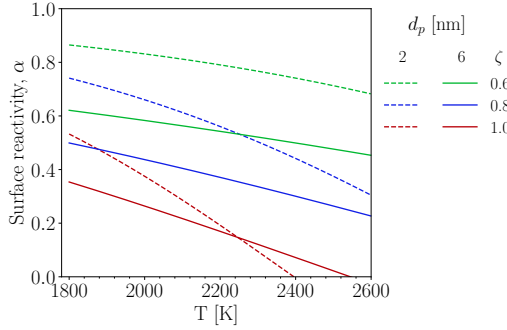


Figure 3.25: The variation of surface reactivity, α , as a function of temperature for different values of ζ and primary particle size of 2 nm (dashed lines) and 6 nm (solid lines)

A series of simulation were performed to study the damping effect of temperature on soot mass and morphology by varying ζ from 1 to 0.8 and 0.6. Note that, ζ of 1 represent the original α formulation. The reaction mechanism and particle dynamic model were set to KAUST and MPBM, respectively, but all PAH growth were used in the simulations. Fig. 3.26 and 3.27 depicts the volume fraction and soot carbon yield, respectively. As expected, both quantities increases by reducing ζ . The difference due to three *zeta* values become significant only after $t=1.5$ ms, so it does not change the agreement with measurements available up to 1 ms. The final SY at the end of 5 ms increases by a factor of 1.3 to 2 depending on the PAH growth model by varying ζ from 1 to 0.6. Additionally, soot yield for DC, EF, and ID models levels off towards the end of simulation indicating the maximum yield.

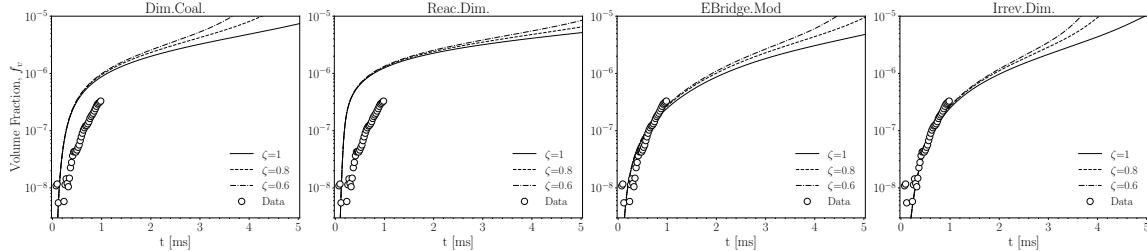


Figure 3.26: The effect of reducing ζ leading to larger HACA rates on soot volume fraction, f_v using KAUST and MPBM and different PAH growth model

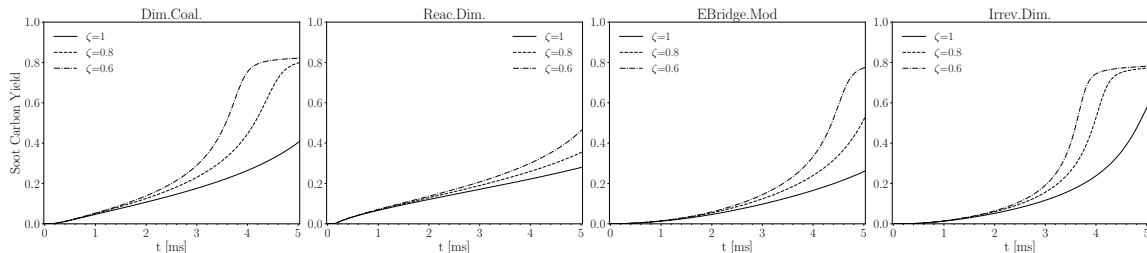


Figure 3.27: The effect of reducing ζ leading to larger HACA rates on soot carbon yield using KAUST and MPBM and different PAH growth model

Fig.3.28 demonstrates changes of d_p and d_m due to ζ values using different PAH growth models. Reducing ζ to 0.6 increases d_p to a maximum of 2 nm. d_p predicted by DC, EF, and ID model reaches its maximum indicating that smaller ζ values (higher HACA rate) will not change the maximum

d_p . The simulations using different ζ values highlight relatively low sensitivity of d_p with respect to surface reactivity in 10% CH₄ pyrolysis in shock tube described using a constant volume reactor.

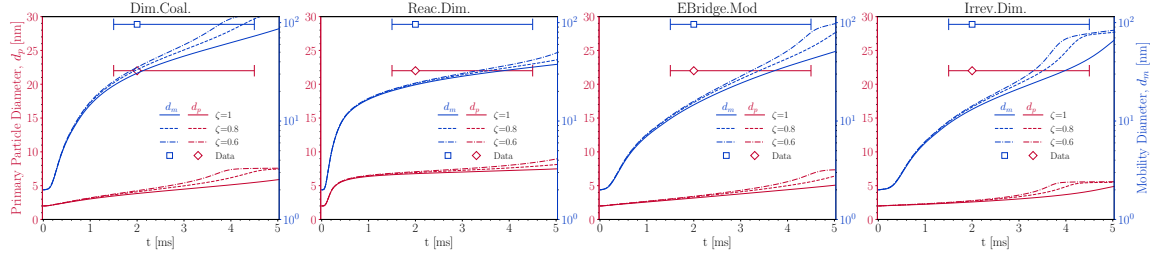


Figure 3.28: The effect of reducing ζ leading to larger HACA rates on mobility, d_m and primary particle diameter, d_p using KAUST and MPBM and different PAH growth model

Bibliography

- [1] GL Agafonov, IV Bilera, PA Vlasov, IV Zhil'tsova, Yu A Kolbanovskii, VN Smirnov, and AM Tereza. Unified kinetic model of soot formation in the pyrolysis and oxidation of aliphatic and aromatic hydrocarbons in shock waves. *Kinetics and Catalysis*, 57:557–572, 2016.
- [2] Gunnar Myhre, Drew Shindell, and Julia Pongratz. Anthropogenic and natural radiative forcing. 2014.
- [3] World Health Organization et al. Health effects of particulate matter: Policy implications for countries in eastern europe, caucasus and central asia. 2013.
- [4] U.S. EPA. Integrated science assessment (isa) for particulate matter (final report, dec 2019). 2019.
- [5] Ann Y Watson and Peter A Valberg. Carbon black and soot: two different substances. *AIHAJ-American Industrial Hygiene Association*, 62(2):218–228, 2001.
- [6] International Carbon Black Association et al. Carbon black user's guide. *available at www.carbon-black.org*, 2016.
- [7] Verónica Palomares, Aintzane Goñi, Izaskun Gil De Muro, Iratxe De Meatza, Miguel Ben-goechea, Igor Cantero, and Teófilo Rojo. Conductive additive content balance in li-ion battery cathodes: Commercial carbon blacks vs. in situ carbon from lifepo₄/c composites. *J. Power Sources*, 195:7661–7668, 2010. ISSN 0378-7753.
- [8] Sotiris E Pratsinis. History of manufacture of fine particles in high-temperature aerosol reactors. *Aerosol science and technology: History and reviews*, pages 475–507, 2011.
- [9] Roop Chand Bansal, Meng-Jiao Wang, and JB Donnet. Carbon black. *Science and Technology*, 133, 1993.
- [10] Wonihl Cho, Seung-Ho Lee, Woo-Sung Ju, Youngsoon Baek, and Joong Kee Lee. Conversion of natural gas to hydrogen and carbon black by plasma and application of plasma carbon black. *Catalysis Today*, 98(4):633–638, 2004.
- [11] Soo-Jin Park, Min-Kang Seo, and Changwoon Nah. Influence of surface characteristics of carbon blacks on cure and mechanical behaviors of rubber matrix compoundings. *Journal of colloid and interface science*, 291(1):229–235, 2005.
- [12] C Russo, A Tregrossi, and A Ciajolo. Dehydrogenation and growth of soot in premixed flames. *Proceedings of the Combustion Institute*, 35(2):1803–1809, 2015.
- [13] Madhu Singh and Randy L Vander Wal. Nanostructure quantification of carbon blacks. *C*, 5 (1):2, 2018.
- [14] Randy L Vander Wal, Aleksey Yezerets, Neal W Currier, Do Heui Kim, and Chong Min Wang. Hrtem study of diesel soot collected from diesel particulate filters. *Carbon*, 45(1):70–77, 2007.

- [15] Magín Lapuerta, Javier Barba, Anton D Sediako, Mohammad Reza Kholghy, and Murray J Thomson. Morphological analysis of soot agglomerates from biodiesel surrogates in a coflow burner. *Journal of Aerosol Science*, 111:65–74, 2017.
- [16] Andrea D’Anna. Combustion-formed nanoparticles. *Proceedings of the Combustion Institute*, 32(1):593–613, 2009.
- [17] Kiminori Ono, Kazuki Dewa, Yoshiya Matsukawa, Yasuhiro Saito, Yohsuke Matsushita, Hideyuki Aoki, Koki Era, Takayuki Aoki, and Togo Yamaguchi. Experimental evidence for the sintering of primary soot particles. *Journal of Aerosol Science*, 105:1–9, 2017.
- [18] Jiangjun Wei, Yang Zeng, Mingzhang Pan, Yuan Zhuang, Liang Qiu, Taotao Zhou, and Yongqiang Liu. Morphology analysis of soot particles from a modern diesel engine fueled with different types of oxygenated fuels. *Fuel*, 267:117248, 2020.
- [19] M Alfè, B Apicella, Rouzaud Barbella, J-N Rouzaud, A Tregrossi, and A Ciajolo. Structure–property relationship in nanostructures of young and mature soot in premixed flames. *Proceedings of the Combustion Institute*, 32(1):697–704, 2009.
- [20] Stephen E Stein and A Fahr. High-temperature stabilities of hydrocarbons. *The Journal of Physical Chemistry*, 89(17):3714–3725, 1985.
- [21] Hai Wang. Formation of nascent soot and other condensed-phase materials in flames. *Proc Combust Inst.*, 33:41–67, 2011. ISSN 15407489.
- [22] Michael Frenklach. Reaction mechanism of soot formation in flames. *Physical chemistry chemical Physics*, 4(11):2028–2037, 2002.
- [23] Askar Fahr and SE Stein. Reactions of vinyl and phenyl radicals with ethyne, ethene and benzene. In *Symposium (International) on Combustion*, volume 22, pages 1023–1029. Elsevier, 1989.
- [24] KO Johansson, MP Head-Gordon, PE Schrader, KR Wilson, and HA Michelsen. Resonance-stabilized hydrocarbon-radical chain reactions may explain soot inception and growth. *Science*, 361(6406):997–1000, 2018.
- [25] Michael Frenklach and Alexander M Mebel. On the mechanism of soot nucleation. *Physical Chemistry Chemical Physics*, 22(9):5314–5331, 2020.
- [26] Michael Frenklach and Lawrence B Ebert. Comment on the proposed role of spheroidal carbon clusters in soot formation. *The Journal of Physical Chemistry*, 92(2):561–563, 1988.
- [27] Bin Zhao, Zhiwei Yang, Murray V Johnston, Hai Wang, Anthony S Wexler, Michael Balthasar, and Markus Kraft. Measurement and numerical simulation of soot particle size distribution functions in a laminar premixed ethylene-oxygen-argon flame. *Combustion and Flame*, 133 (1-2):173–188, 2003.
- [28] Aamir D Abid, Joaquin Camacho, David A Sheen, and Hai Wang. Quantitative measurement of soot particle size distribution in premixed flames—the burner-stabilized stagnation flame approach. *Combustion and Flame*, 156(10):1862–1870, 2009.
- [29] Joachim Happold, Horst-Henning Grotheer, and Manfred Aigner. Soot precursors consisting of stacked pericondensed pahs. *Combustion generated fine carbonaceous particles*, pages 275–285, 2009.
- [30] Jennifer D Herdman and J Houston Miller. Intermolecular potential calculations for polynuclear aromatic hydrocarbon clusters. *The Journal of Physical Chemistry A*, 112(28):6249–6256, 2008.

- [31] Tim S Totton, Alston J Misquitta, and Markus Kraft. A quantitative study of the clustering of polycyclic aromatic hydrocarbons at high temperatures. *Physical chemistry chemical physics*, 14(12):4081–4094, 2012.
- [32] David Wong, R Whitesides, CA Schuetz, and M Frenklach. Molecular dynamics simulations of pah dimerization. *Combustion Generated Fine Carbonaceous Particles*, pages 247–257, 2009.
- [33] Jeremy P Cain, Joaquin Camacho, Denis J Phares, Hai Wang, and Alexander Laskin. Evidence of aliphatics in nascent soot particles in premixed ethylene flames. *Proceedings of the Combustion Institute*, 33(1):533–540, 2011.
- [34] Bin Zhao, Zhiwei Yang, Zhigang Li, Murray V Johnston, and Hai Wang. Particle size distribution function of incipient soot in laminar premixed ethylene flames: effect of flame temperature. *Proceedings of the Combustion Institute*, 30(1):1441–1448, 2005.
- [35] Jacob W Martin, Maurin Salamanca, and Markus Kraft. Soot inception: Carbonaceous nanoparticle formation in flames. *Progress in Energy and Combustion Science*, 88:100956, 2022.
- [36] Angela Violi, Gregory A Voth, and Adel F Sarofim. The relative roles of acetylene and aromatic precursors during soot particle inception. *Proceedings of the Combustion Institute*, 30(1):1343–1351, 2005.
- [37] Mohammad Reza Kholghy, Yashar Afarin, Anton D Sediako, Javier Barba, Magín Lapuerta, Carson Chu, Jason Weingarten, Bobby Borshanpour, Victor Chernov, and Murray J Thomson. Comparison of multiple diagnostic techniques to study soot formation and morphology in a diffusion flame. *Combustion and Flame*, 176:567–583, 2017.
- [38] Christopher R Shaddix and Kermit C Smyth. Laser-induced incandescence measurements of soot production in steady and flickering methane, propane, and ethylene diffusion flames. *Combustion and flame*, 107(4):418–452, 1996.
- [39] Nimeti Doner and Fengshan Liu. Impact of morphology on the radiative properties of fractal soot aggregates. *Journal of Quantitative Spectroscopy and Radiative Transfer*, 187:10–19, 2017.
- [40] Michael Frenklach and Hai Wang. Detailed modeling of soot particle nucleation and growth. In *Symposium (International) on Combustion*, volume 23, pages 1559–1566. Elsevier, 1991.
- [41] Steffen Salenbauch, Alberto Cuoci, Alessio Frassoldati, Chiara Saggese, Tiziano Faravelli, and Christian Hasse. Modeling soot formation in premixed flames using an extended conditional quadrature method of moments. *Combustion and Flame*, 162(6):2529–2543, 2015.
- [42] Pascale Desgroux, Alessandro Faccinetto, Xavier Mercier, Thomas Mouton, Damien Aubagnac Karkar, and Abderrahman El Bakali. Comparative study of the soot formation process in a “nucleation” and a “sooting” low pressure premixed methane flame. *Combustion and Flame*, 184:153–166, 2017.
- [43] Yu Wang, Abhijeet Raj, and Suk Ho Chung. Soot modeling of counterflow diffusion flames of ethylene-based binary mixture fuels. *Combustion and Flame*, 162(3):586–596, 2015.
- [44] Lei Xu, Fuwu Yan, Mengxiang Zhou, and Yu Wang. An experimental and modeling study on sooting characteristics of laminar counterflow diffusion flames with partial premixing. *Energy*, 218:119479, 2021.
- [45] Mohammad Reza Kholghy, Armin Veshkini, and Murray John Thomson. The core–shell internal nanostructure of soot—a criterion to model soot maturity. *Carbon*, 100:508–536, 2016.
- [46] Armin Veshkini, Seth B Dworkin, and Murray J Thomson. Understanding soot particle size evolution in laminar ethylene/air diffusion flames using novel soot coalescence models. *Combustion Theory and Modelling*, 20(4):707–734, 2016.

- [47] G Blanquart and H Pitsch. Analyzing the effects of temperature on soot formation with a joint volume-surface-hydrogen model. *Combustion and Flame*, 156(8):1614–1626, 2009.
- [48] J Houston Miller, Kermit C Smyth, and W Gary Mallard. Calculations of the dimerization of aromatic hydrocarbons: Implications for soot formation. In *Symposium (International) on Combustion*, volume 20, pages 1139–1147. Elsevier, 1985.
- [49] Hassan Sabbah, Ludovic Biennier, Stephen J Klippenstein, Ian R Sims, and Bertrand R Rowe. Exploring the role of pahs in the formation of soot: Pyrene dimerization. *The Journal of Physical Chemistry Letters*, 1(19):2962–2967, 2010.
- [50] Ali Naseri, M Reza Kholghy, Neil A Juan, and Murray J Thomson. Simulating yield and morphology of carbonaceous nanoparticles during fuel pyrolysis in laminar flow reactors enabled by reactive inception and aromatic adsorption. *Combustion and Flame*, 237:111721, 2022.
- [51] Nazly E Sanchez, Alicia Callejas, Angela Millera, Rafael Bilbao, and Maria U Alzueta. Polycyclic aromatic hydrocarbon (pah) and soot formation in the pyrolysis of acetylene and ethylene: effect of the reaction temperature. *Energy & fuels*, 26(8):4823–4829, 2012.
- [52] Sanghwan Cho, Seunghoon Lee, Wonnam Lee, and Sunho Park. Synthesis of primary-particle-size-tuned soot particles by controlled pyrolysis of hydrocarbon fuels. *Energy & Fuels*, 30(8):6614–6619, 2016.
- [53] Meghdad Saffaripour, Armin Veshkini, Mohammadreza Kholghy, and Murray J Thomson. Experimental investigation and detailed modeling of soot aggregate formation and size distribution in laminar coflow diffusion flames of jet a-1, a synthetic kerosene, and n-decane. *Combustion and Flame*, 161(3):848–863, 2014.
- [54] J Houston Miller. The kinetics of polynuclear aromatic hydrocarbon agglomeration in flames. In *Symposium (International) on Combustion*, volume 23, pages 91–98. Elsevier, 1991.
- [55] Anna Giordana, Andrea Maranzana, and Glauco Tonachini. Theoretical investigation of soot nanoparticle inception via polycyclic aromatic hydrocarbon coagulation (condensation): Energetic, structural, and electronic features. *The Journal of Physical Chemistry C*, 115(5):1732–1739, 2011.
- [56] NA Eaves, SB Dworkin, and MJ Thomson. The importance of reversibility in modeling soot nucleation and condensation processes. *Proceedings of the Combustion Institute*, 35(2):1787–1794, 2015.
- [57] Mohammad Reza Kholghy, Nick Anthony Eaves, Armin Veshkini, and Murray John Thomson. The role of reactive pah dimerization in reducing soot nucleation reversibility. *Proceedings of the Combustion Institute*, 37(1):1003–1011, 2019.
- [58] Mohammad R Kholghy, Georgios A Kelesidis, and Sotiris E Pratsinis. Reactive polycyclic aromatic hydrocarbon dimerization drives soot nucleation. *Physical Chemistry Chemical Physics*, 20(16):10926–10938, 2018.
- [59] Jörg Appel, Henning Bockhorn, and Michael Frenklach. Kinetic modeling of soot formation with detailed chemistry and physics: laminar premixed flames of c2 hydrocarbons. *Combustion and flame*, 121(1-2):122–136, 2000.
- [60] IT Woods and BS Haynes. Soot surface growth at active sites. *Combustion and flame*, 85 (3-4):523–525, 1991.
- [61] Cameron J Dasch. The decay of soot surface growth reactivity and its importance in total soot formation. *Combustion and flame*, 61(3):219–225, 1985.

- [62] Jasdeep Singh, Robert IA Patterson, Markus Kraft, and Hai Wang. Numerical simulation and sensitivity analysis of detailed soot particle size distribution in laminar premixed ethylene flames. *Combustion and Flame*, 145(1-2):117–127, 2006.
- [63] Hope A Michelsen, Meredith B Colket, Per-Erik Bengtsson, Andrea D’anna, Pascale Desgroux, Brian S Haynes, J Houston Miller, Graham J Nathan, Heinz Pitsch, and Hai Wang. A review of terminology used to describe soot formation and evolution under combustion and pyrolytic conditions. *ACS nano*, 14(10):12470–12490, 2020.
- [64] OI Obolensky, VV Semenikhina, AV Solov’Yov, and W Greiner. Interplay of electrostatic and van der waals forces in coronene dimer. *International Journal of Quantum Chemistry*, 107(6):1335–1343, 2007.
- [65] Eirini Goudeli, Maximilian L Eggersdorfer, and Sotiris E Pratsinis. Coagulation of agglomerates consisting of polydisperse primary particles. *Langmuir*, 32:9276–9285, 2016. ISSN 0743-7463.
- [66] FS Lai, SK Friedlander, J Pich, and GM Hidy. The self-preserving particle size distribution for brownian coagulation in the free-molecule regime. *Journal of Colloid and Interface Science*, 39(2):395–405, 1972.
- [67] Raymond D Mountain, George W Mulholland, and Howard Baum. Simulation of aerosol agglomeration in the free molecular and continuum flow regimes. *Journal of Colloid and Interface Science*, 114(1):67–81, 1986.
- [68] Georgios A. Kelesidis, Eirini Goudeli, and Sotiris E. Pratsinis. Morphology and mobility diameter of carbonaceous aerosols during agglomeration and surface growth. *Carbon*, 121:527–535, 9 2017. ISSN 00086223.
- [69] Georgios A Kelesidis and Eirini Goudeli. Self-preserving size distribution and collision frequency of flame-made nanoparticles in the transition regime. *Proceedings of the Combustion Institute*, 38(1):1233–1240, 2021.
- [70] Georgios A. Kelesidis, Eirini Goudeli, and Sotiris E. Pratsinis. Flame synthesis of functional nanostructured materials and devices: Surface growth and aggregation. *Proc Combust Inst* ., 36:29–50, 2017. ISSN 15407489.
- [71] Georgios A Kelesidis and Sotiris E Pratsinis. A perspective on gas-phase synthesis of nanomaterials: Process design, impact and outlook. *Chemical Engineering Journal*, 421:129884, 2021.
- [72] Yun Xiong and Sotiris E Pratsinis. Formation of agglomerate particles by coagulation and sintering—part i. a two-dimensional solution of the population balance equation. *J. Aerosol Sci.*, 24:283–300, 1993. ISSN 0021-8502.
- [73] SH Park, SN Rogak, WK Bushe, JZ Wen, and MJ Thomson. An aerosol model to predict size and structure of soot particles. *Combustion Theory and Modelling*, 9(3):499–513, 2005.
- [74] MA Schiener and RP Lindstedt. Transported probability density function based modelling of soot particle size distributions in non-premixed turbulent jet flames. *Proceedings of the Combustion Institute*, 37(1):1049–1056, 2019.
- [75] Themis Matsoukas and Sheldon K Friedlander. Dynamics of aerosol agglomerate formation. *Journal of Colloid and Interface Science*, 146(2):495–506, 1991.
- [76] MD Smooke, MB Long, BC Connelly, MB Colket, and RJ Hall. Soot formation in laminar diffusion flames. *Combustion and Flame*, 143(4):613–628, 2005.

- [77] Damien Aubagnac-Karkar, Abderrahman El Bakali, and Pascale Desgroux. Soot particles inception and pah condensation modelling applied in a soot model utilizing a sectional method. *Combustion and Flame*, 189:190–206, 2018.
- [78] Andrei Kazakov and Michael Frenklach. Dynamic modeling of soot particle coagulation and aggregation: Implementation with the method of moments and application to high-pressure laminar premixed flames. *Combustion and flame*, 114(3-4):484–501, 1998.
- [79] F Einar Kruis, Karl A Kusters, Sotiris E Pratsinis, and Brian Scarlett. A simple model for the evolution of the characteristics of aggregate particles undergoing coagulation and sintering. *Aerosol science and technology*, 19(4):514–526, 1993.
- [80] Patrick T Spicer, Olivier Chaoul, Stavros Tsantilis, and Sotiris E Pratsinis. Titania formation by $TiCl_4$ gas phase oxidation, surface growth and coagulation. *J. Aerosol Sci.*, 33:17–34, 2002. ISSN 0021-8502.
- [81] Georgios A Kelesidis and Sotiris E Pratsinis. Estimating the internal and surface oxidation of soot agglomerates. *Combustion and Flame*, 209:493–499, 2019.
- [82] Aamir D Abid, Nicholas Heinz, Erik D Tolmachoff, Denis J Phares, Charles S Campbell, and Hai Wang. On evolution of particle size distribution functions of incipient soot in premixed ethylene–oxygen–argon flames. *Combustion and Flame*, 154(4):775–788, 2008.
- [83] X Ma, CD Zangmeister, and MR Zachariah. Soot oxidation kinetics: a comparison study of two tandem ion-mobility methods. *The Journal of Physical Chemistry C*, 117(20):10723–10729, 2013.
- [84] Joaquin Camacho, Changran Liu, Chen Gu, He Lin, Zhen Huang, Quanxi Tang, Xiaoqing You, Chiara Saggese, Yang Li, Heejung Jung, et al. Mobility size and mass of nascent soot particles in a benchmark premixed ethylene flame. *Combustion and Flame*, 162(10):3810–3822, 2015.
- [85] Arto J Gröhn, Sotiris E Pratsinis, and Karsten Wegner. Fluid-particle dynamics during combustion spray aerosol synthesis of ZrO_2 . *Chemical Engineering Journal*, 191:491–502, 2012.
- [86] Sotiris E Pratsinis. Simultaneous nucleation, condensation, and coagulation in aerosol reactors. *Journal of colloid and interface science*, 124(2):416–427, 1988.
- [87] Guillaume Blanquart and Heinz Pitsch. A joint volume-surface-hydrogen multi-variate model for soot formation. *Combustion generated fine carbonaceous particles*, pages 437–463, 2009.
- [88] Kyo-Seon Kim and Sotiris E Pratsinis. Manufacture of optical waveguide preforms by modified chemical vapor deposition. *AIChE journal*, 34(6):912–921, 1988.
- [89] Michael Frenklach and Stephen J Harris. Aerosol dynamics modeling using the method of moments. *Journal of colloid and interface science*, 118(1):252–261, 1987.
- [90] Stavros Tsantilis and Sotiris E Pratsinis. Soft-and hard-agglomerate aerosols made at high temperatures. *Langmuir*, 20(14):5933–5939, 2004.
- [91] Peter R Lindstedt. Simplified soot nucleation and surface growth steps for non-premixed flames. In *Soot formation in combustion: mechanisms and models*, pages 417–441. Springer, 1994.
- [92] Robert N Grass, Stavros Tsantilis, and Sotiris E Pratsinis. Design of high-temperature, gas-phase synthesis of hard or soft TiO_2 agglomerates. *AIChE Journal*, 52(4):1318–1325, 2006.
- [93] Hope A Michelsen. Probing soot formation, chemical and physical evolution, and oxidation: A review of in situ diagnostic techniques and needs. *Proceedings of the Combustion Institute*, 36(1):717–735, 2017.

- [94] Rosalind E Franklin. Crystallite growth in graphitizing and non-graphitizing carbons. *Proceedings of the Royal Society of London. Series A. Mathematical and Physical Sciences*, 209 (1097):196–218, 1951.
- [95] Brian S Haynes and H Gg Wagner. Soot formation. *Progress in energy and combustion science*, 7(4):229–273, 1981.
- [96] Joaquin Camacho, Yujie Tao, and Hai Wang. Kinetics of nascent soot oxidation by molecular oxygen in a flow reactor. *Proceedings of the Combustion Institute*, 35(2):1887–1894, 2015.
- [97] Robert H Hurt, Gregory P Crawford, and Hong-Shig Shim. Equilibrium nanostructure of primary soot particles. *Proceedings of the Combustion Institute*, 28(2):2539–2546, 2000.
- [98] Charles S McEnally, Ümit Ö Köylü, Lisa D Pfefferle, and Daniel E Rosner. Soot volume fraction and temperature measurements in laminar nonpremixed flames using thermocouples. *Combustion and Flame*, 109(4):701–720, 1997.
- [99] Pascale Desgroux, Xavier Mercier, and Kevin A Thomson. Study of the formation of soot and its precursors in flames using optical diagnostics. *Proceedings of the Combustion Institute*, 34 (1):1713–1738, 2013.
- [100] Randy L Vander Wal and Aaron J Tomasek. Soot nanostructure: dependence upon synthesis conditions. *Combustion and Flame*, 136(1-2):129–140, 2004.
- [101] Nils-Erik Olofsson, Johan Simonsson, Sandra Török, Henrik Bladh, and Per-Erik Bengtsson. Evolution of properties for aging soot in premixed flat flames studied by laser-induced incandescence and elastic light scattering. *Applied Physics B*, 119:669–683, 2015.
- [102] A Eremin, E Gurentsov, E Popova, and K Priemchenko. Size dependence of complex refractive index function of growing nanoparticles. *Applied Physics B*, 104:285–295, 2011.
- [103] WH Dalzell and AF Sarofim. Optical constants of soot and their application to heat-flux calculations. 1969.
- [104] Jochen Zerbs, Klaus Peter Geigle, Oliver Lammel, Joachim Hader, Ronnie Stirn, Redjem Hadef, and Wolfgang Meier. The influence of wavelength in extinction measurements and beam steering in laser-induced incandescence measurements in sooting flames. *Applied Physics B*, 96:683–694, 2009.
- [105] Georgios A Kelesidis and Sotiris E Pratsinis. Determination of the volume fraction of soot accounting for its composition and morphology. *Proceedings of the Combustion Institute*, 38 (1):1189–1196, 2021.
- [106] Karthik V Puduppakkam, Abhijit U Modak, Chitralkumar V Naik, Joaquin Camacho, Hai Wang, and Ellen Meeks. A soot chemistry model that captures fuel effects. In *Turbo Expo: Power for Land, Sea, and Air*, volume 45691, page V04BT04A055. American Society of Mechanical Engineers, 2014.
- [107] Tami C Bond and Robert W Bergstrom. Light absorption by carbonaceous particles: An investigative review. *Aerosol science and technology*, 40(1):27–67, 2006.
- [108] J Tauc, Radu Grigorovici, and Anina Vancu. Optical properties and electronic structure of amorphous germanium. *physica status solidi (b)*, 15(2):627–637, 1966.
- [109] J Robertson and EP O’reilly. Electronic and atomic structure of amorphous carbon. *Physical Review B*, 35(6):2946, 1987.
- [110] Changran Liu, Ajay V Singh, Chiara Saggese, Quanxi Tang, Dongping Chen, Kevin Wan, Marianna Vinciguerra, Mario Commodo, Gianluigi De Falco, Patrizia Minutolo, et al. Flame-formed carbon nanoparticles exhibit quantum dot behaviors. *Proceedings of the National Academy of Sciences*, 116(26):12692–12697, 2019.

- [111] Kim Cuong Le, Carmela Russo, Sandra Török, Barbara Apicella, Antonio Tregrossi, Per-Erik Bengtsson, and Anna Ciajolo. Soot optical band gap evaluated through in-situ and ex-situ measurements as tracer of soot evolution in premixed flames: Soot optical band gap evaluated through in-situ and ex-situ measurements as tracer of soot evolution in premixed flames. 2019.
- [112] Carmela Russo, Barbara Apicella, Antonio Tregrossi, Anna Ciajolo, Kim Cuong Le, Sandra Török, and Per-Erik Bengtsson. Optical band gap analysis of soot and organic carbon in premixed ethylene flames: comparison of in-situ and ex-situ absorption measurements. *Carbon*, 158:89–96, 2020.
- [113] Georgios A Kelesidis and Sotiris E Pratsinis. Soot light absorption and refractive index during agglomeration and surface growth. *Proceedings of the Combustion Institute*, 37(1):1177–1184, 2019.
- [114] P Minutolo, G Gambi, and A D'alessio. The optical band gap model in the interpretation of the uv-visible absorption spectra of rich premixed flames. In *Symposium (International) on Combustion*, volume 26, pages 951–957. Elsevier, 1996.
- [115] F Moulin, Michel Devel, and S Picaud. Optical properties of soot nanoparticles. *Journal of Quantitative Spectroscopy and Radiative Transfer*, 109(10):1791–1801, 2008.
- [116] Jérôme Yon, A Bescond, and Franklin Liu. On the radiative properties of soot aggregates part 1: Necking and overlapping. *Journal of Quantitative Spectroscopy and Radiative Transfer*, 162:197–206, 2015.
- [117] Salma Bejaoui, Sébastien Batut, Eric Therssen, Nathalie Lamoureux, Pascale Desgroux, and Fengshan Liu. Measurements and modeling of laser-induced incandescence of soot at different heights in a flat premixed flame. *Applied Physics B*, 118:449–469, 2015.
- [118] Hope A Michelsen, Paul E Schrader, and Fabien Goulay. Wavelength and temperature dependences of the absorption and scattering cross sections of soot. *Carbon*, 48(8):2175–2191, 2010.
- [119] G Cléon, T Amodeo, A Faccinetto, and P Desgroux. Laser induced incandescence determination of the ratio of the soot absorption functions at 532 nm and 1064 nm in the nucleation zone of a low pressure premixed sooting flame. *Applied Physics B*, 104(2):297–305, 2011.
- [120] Junyu Mei, Yuxin Zhou, Xiaoqing You, and Chung K Law. Formation of nascent soot during very fuel-rich oxidation of ethylene at low temperatures. *Combustion and Flame*, 226:31–41, 2021.
- [121] Georgios A Kelesidis and Sotiris E Pratsinis. Santoro flame: The volume fraction of soot accounting for its morphology & composition. *Combustion and Flame*, 240:112025, 2022.
- [122] KG Neoh, JB Howard, and AF Sarofim. Soot oxidation in flames. *Particulate carbon: formation during combustion*, pages 261–282, 1981.
- [123] JS Lighty, V Romano, and AF Sarofim. Soot oxidation. In *Combustion generated fine carbonaceous particles (proceedings of an international workshop held in Villa Orlandi, Anacapri, May 13e16, 2007)*. KIT Scientific Publishing, pages 523–36, 2009.
- [124] Charles P Fenimore and George Wallace Jones. Oxidation of soot by hydroxyl radicals. *The Journal of physical chemistry*, 71(3):593–597, 1967.
- [125] KB Lee, MW Thring, and JM Beer. On the rate of combustion of soot in a laminar soot flame. *Combustion and Flame*, 6:137–145, 1962.
- [126] William Bartok and Adel F Sarofim. Fossil fuel combustion: a source book. 1991.

- [127] J Nagle and RF Strickland-Constable. Oxidation of carbon between 1000–2000 c. In *Proceedings of the fifth conference on carbon*, pages 154–164. Elsevier, 1962.
- [128] John PA Neeft, T Xander Nijhuis, Erik Smakman, Michiel Makkee, and Jacob A Moulijn. Kinetics of the oxidation of diesel soot. *Fuel*, 76(12):1129–1136, 1997.
- [129] Georgios A Kelesidis, Nicola Rossi, and Sotiris E Pratsinis. Porosity and crystallinity dynamics of carbon black during internal and surface oxidation. *Carbon*, 197:334–340, 2022.
- [130] Tomoji Ishiguro, Noritomo Suzuki, Yoshiyasu Fujitani, and Hidetake Morimoto. Microstructural changes of diesel soot during oxidation. *Combustion and Flame*, 85(1-2):1–6, 1991.
- [131] Juhun Song, Mahabubul Alam, André L Boehman, and Unjeong Kim. Examination of the oxidation behavior of biodiesel soot. *Combustion and flame*, 146(4):589–604, 2006.
- [132] F Xu, PB Sunderland, and GM Faeth. Soot formation in laminar premixed ethylene/air flames at atmospheric pressure. *Combustion and Flame*, 108(4):471–493, 1997.
- [133] RTFRJRA Puri, TF Richardson, RJ Santoro, and RA Dobbins. Aerosol dynamic processes of soot aggregates in a laminar ethene diffusion flame. *Combustion and flame*, 92(3):320–333, 1993.
- [134] David G. Goodwin, Harry K. Moffat, Ingmar Schoegl, Raymond L. Speth, and Bryan W. Weber. Cantera: An object-oriented software toolkit for chemical kinetics, thermodynamics, and transport processes. <https://www.cantera.org>, 2022. Version 2.6.0.
- [135] Kirk A Jensen, Jill M Suo-Anttila, and Linda G Blevins. Measurement of soot morphology, chemistry, and optical properties in the visible and near-infrared spectrum in the flame zone and overfire region of large jp-8 pool fires. *Combustion science and technology*, 179(12):2453–2487, 2007.
- [136] Bonnie J McBride. *Coefficients for calculating thermodynamic and transport properties of individual species*, volume 4513. National Aeronautics and Space Administration, Office of Management . . . , 1993.
- [137] Robert J Kee, Michael E Coltrin, Peter Glarborg, and Huayang Zhu. *Chemically reacting flow: theory, modeling, and simulation*. John Wiley & Sons, 2017.
- [138] Skjalg E Haaland. Simple and explicit formulas for the friction factor in turbulent pipe flow. 1983.
- [139] George W Mulholland, RJ Samson, RD Mountain, and MH Ernst. Cluster size distribution for free molecular agglomeration. *Energy & Fuels*, 2(4):481–486, 1988.
- [140] RC Ball and R Jullien. Finite size effects in cluster-cluster aggregation. *Journal de Physique Lettres*, 45(21):1031–1035, 1984.
- [141] Jérôme Yon, A Bescond, and F-X Ouf. A simple semi-empirical model for effective density measurements of fractal aggregates. *Journal of Aerosol Science*, 87:28–37, 2015.
- [142] Jenny Rissler, Maria E Messing, Azhar I Malik, Patrik T Nilsson, Erik Z Nordin, Mats Bohgard, Mehri Sanati, and Joakim H Pagels. Effective density characterization of soot agglomerates from various sources and comparison to aggregation theory. *Aerosol Science and Technology*, 47(7):792–805, 2013.
- [143] Anna Ciajolo, Rosalba Barbella, Antonio Tregrossi, and Loretta Bonfanti. Spectroscopic and compositional signatures of pah-loaded mixtures in the soot inception region of a premixed ethylene flame. In *Symposium (International) on Combustion*, volume 27, pages 1481–1487. Elsevier, 1998.

- [144] Christopher Betrancourt, Fengshan Liu, Pascale Desgroux, Xavier Mercier, Alessandro Facinetto, Maurin Salamanca, Lena Ruwe, Katharina Kohse-Höinghaus, Daniel Emmrich, André Beyer, et al. Investigation of the size of the incandescent incipient soot particles in premixed sooting and nucleation flames of n-butane using lii, him, and 1 nm-smps. *Aerosol Science and Technology*, 51(8):916–935, 2017.
- [145] Nikolaj A Fuchs, RE Daisley, Marina Fuchs, CN Davies, and ME Straumanis. The mechanics of aerosols, 1965.
- [146] Jin Jwang Wu and Richard C Flagan. A discrete-sectional solution to the aerosol dynamic equation. *Journal of Colloid and Interface Science*, 123(2):339–352, 1988.
- [147] BS Haynes and H Gg Wagner. The surface growth phenomenon in soot formation. *Zeitschrift für Physikalische Chemie*, 133(2):201–213, 1982.
- [148] Stephen J Harris and Anita M Weiner. Chemical kinetics of soot particle growth. *Annual Review of Physical Chemistry*, 36(1):31–52, 1985.
- [149] KH Homann. Formation of large molecules, particulates and ions in premixed hydrocarbon flames; progress and unresolved questions. In *Symposium (International) on Combustion*, volume 20, pages 857–870. Elsevier, 1985.
- [150] Armin Veshkini. *Understanding Soot Particle Growth Chemistry and Particle Sizing Using a Novel Soot Growth and Formation Model*. University of Toronto (Canada), 2015.
- [151] K Olof Johansson, Tyler Dillstrom, Matteo Monti, Farid El Gabaly, Matthew F Campbell, Paul E Schrader, Denisia M Popolan-Vaida, Nicole K Richards-Henderson, Kevin R Wilson, Angela Violi, et al. Formation and emission of large furans and oxygenated hydrocarbons from flames. *Proceedings of the National Academy of Sciences*, 113(30):8374–8379, 2016.
- [152] J Houston Miller, W Gary Mallard, and Kermit C Smyth. Intermolecular potential calculations for polycyclic aromatic hydrocarbons. *The Journal of Physical Chemistry*, 88(21):4963–4970, 1984.
- [153] Yoichiro Araki, Yoshiya Matsukawa, Yasuhiro Saito, Yohsuke Matsushita, Hideyuki Aoki, Koki Era, and Takayuki Aoki. Effects of carrier gas on the properties of soot produced by ethylene pyrolysis. *Fuel Processing Technology*, 213:106673, 2021.
- [154] Binxuan Sun, Stelios Rigopoulos, and Anxiong Liu. Modelling of soot coalescence and aggregation with a two-population balance equation model and a conservative finite volume method. *Combustion and Flame*, 229:111382, 2021.
- [155] A Tregrossi, A Ciajolo, and R Barbella. The combustion of benzene in rich premixed flames at atmospheric pressure. *Combustion and flame*, 117(3):553–561, 1999.
- [156] Eirini Goudeli, Maximilian L Eggendorfer, and Sotiris E Pratsinis. Coagulation-agglomeration of fractal-like particles: Structure and self-preserving size distribution. *Langmuir*, 31(4):1320–1327, 2015.
- [157] M Reza Kholghy and Georgios A Kelesidis. Surface growth, coagulation and oxidation of soot by a monodisperse population balance model. *Combustion and Flame*, 227:456–463, 2021.
- [158] Srinivas Vemury and Sotiris E Pratsinis. Self-preserving size distributions of agglomerates. *Journal of Aerosol Science*, 26(2):175–185, 1995.
- [159] Laurent Fulcheri, Vandaad-Julien Rohani, Elliott Wyse, Ned Hardman, and Enoch Dames. An energy-efficient plasma methane pyrolysis process for high yields of carbon black and hydrogen. *International Journal of Hydrogen Energy*, 48(8):2920–2928, 2023.

- [160] Yu Wang, Abhijeet Raj, and Suk Ho Chung. A pah growth mechanism and synergistic effect on pah formation in counterflow diffusion flames. *Combustion and flame*, 160(9):1667–1676, 2013.
- [161] Hafiz MF Amin, Anthony Bennett, and William L Roberts. Morphology of soot sampled from n2-diluted methane/air counterflow flames at elevated pressures via tem imaging. *Combustion and Flame*, 216:92–99, 2020.
- [162] Hanson research group shock tubes. <https://hanson.stanford.edu/our-approaches/shock-tubes>. Accessed: 2024-05-24.
- [163] DE Fussey, AJ Gosling, and D Lampard. A shock-tube study of induction times in the formation of carbon particles by pyrolysis of the c2 hydrocarbons. *Combustion and Flame*, 32: 181–192, 1978.
- [164] Nicolas H Pinkowski, Yiming Ding, Sarah E Johnson, Yu Wang, Thomas C Parise, David F Davidson, and Ronald K Hanson. A multi-wavelength speciation framework for high-temperature hydrocarbon pyrolysis. *Journal of Quantitative Spectroscopy and Radiative Transfer*, 225:180–205, 2019.
- [165] Sean J Cassady, Rishav Choudhary, Nicolas H Pinkowski, Jiankun Shao, David F Davidson, and Ronald K Hanson. The thermal decomposition of ethane. *Fuel*, 268:117409, 2020.
- [166] Ivo Stranic and Ronald K Hanson. Laser absorption diagnostic for measuring acetylene concentrations in shock tubes. *Journal of Quantitative Spectroscopy and Radiative Transfer*, 142: 58–65, 2014.
- [167] SC Lee and CL Tien. Optical constants of soot in hydrocarbon flames. In *Symposium (international) on combustion*, volume 18, pages 1159–1166. Elsevier, 1981.
- [168] GL Agafonov, IV Bilera, PA Vlasov, Yu A Kolbanovskii, VN Smirnov, and AM Tereza. Soot formation during the pyrolysis and oxidation of acetylene and ethylene in shock waves. *Kinetics and Catalysis*, 56:12–30, 2015.
- [169] G Blanquart, P Pepiot-Desjardins, and H Pitsch. Chemical mechanism for high temperature combustion of engine relevant fuels with emphasis on soot precursors. *Combustion and Flame*, 156(3):588–607, 2009.
- [170] TA Sipkens and SN Rogak. Using k-means to identify soot aggregates in transmission electron microscopy images. *Journal of Aerosol Science*, 152:105699, 2021.
- [171] Ramin Dastanpour, Jocelyne M Boone, and Steven N Rogak. Automated primary particle sizing of nanoparticle aggregates by tem image analysis. *Powder Technology*, 295:218–224, 2016.
- [172] Jason Olfert and Steven Rogak. Universal relations between soot effective density and primary particle size for common combustion sources. *Aerosol Science and Technology*, 53(5):485–492, 2019.
- [173] Mohsen Kazemimanesh, Ramin Dastanpour, Alberto Baldelli, Alireza Moallemi, Kevin A Thomson, Melina A Jefferson, Matthew R Johnson, Steven N Rogak, and Jason S Olfert. Size, effective density, morphology, and nano-structure of soot particles generated from buoyant turbulent diffusion flames. *Journal of Aerosol Science*, 132:22–31, 2019.
- [174] Ramin Dastanpour, Ali Momenimovahed, Kevin Thomson, Jason Olfert, and Steven Rogak. Variation of the optical properties of soot as a function of particle mass. *Carbon*, 124:201–211, 2017.

- [175] Brian Graves, Jason Olfert, Bronson Patychuk, Ramin Dastanpour, and Steven Rogak. Characterization of particulate matter morphology and volatility from a compression-ignition natural-gas direct-injection engine. *Aerosol Science and Technology*, 49(8):589–598, 2015.
- [176] Marco J Castaldi and SELIM M SENKAW. Pah formation in the premixed flame of ethane. *Combustion science and technology*, 116(1-6):167–181, 1996.
- [177] H Kellerer, A Müller, H-J Bauer, and S Wittig. Soot formation in a shock tube under elevated pressure conditions. *Combustion science and technology*, 113(1):67–80, 1996.
- [178] V Gg Knorre, Dietmar Tanke, Th Thienel, and H Gg Wagner. Soot formation in the pyrolysis of benzene/acetylene and acetylene/hydrogen mixtures at high carbon concentrations. In *Symposium (international) on combustion*, volume 26, pages 2303–2310. Elsevier, 1996.

Appendix A

Derivation of Transport Equations

This chapter explains the derivation of transport equations from first principles for mass, species, energy and soot variables for the reactors employed in omnisooot. The conventional reactor transport equation have been derived for a reacting gas without solid particle [137], so we provide a step by step derivation of equations that describes transport/evolution of mass, species and energy of gas as well as those of soot variables.

A.1 Constant Volume Reactor

A.1.1 Continuity

The rate change of mass of gas mixture is equal to the production rate of soot.

$$\frac{d}{dt} (m) = V (1 - \varphi) \sum_i \dot{s}_i W_i,$$

where V is the reactor volume that stays constant during the process, and gas occupies a fraction of volume reactor without soot, so $m = \rho V(1 - \varphi)$.

$$\begin{aligned} \frac{d}{dt} (\rho V(1 - \varphi)) &= V (1 - \varphi) \sum_i \dot{s}_i W_i \\ &\Downarrow \\ \frac{d}{dt} (\rho(1 - \varphi)) &= (1 - \varphi) \sum_i \dot{s}_i W_i \end{aligned} \tag{A.1}$$

A.1.2 Species

The rate change of mass of each species can be described as:

$$\frac{d}{dt} (m_k) = V (1 - \varphi) (\dot{\omega}_k + \dot{s}_k) W_k$$

The mass of each species is defined as the total gas mass multiplied by the mass fraction as

$$\frac{dY_k}{dt} \rho V(1 - \varphi) + Y_k \frac{d}{dt} (\rho V(1 - \varphi)) = V (1 - \varphi) (\dot{\omega}_k + \dot{s}_k) W_k$$

where the colored term can be substituted from Equation (A.1).

$$\frac{dY_k}{dt} \rho V(1 - \varphi) + Y_k \cancel{V(1 - \varphi)} \sum_i \dot{s}_i W_i = V (1 - \varphi) (\dot{\omega}_k + \dot{s}_k) W_k$$

$$\Downarrow \times \frac{1}{\rho V(1-\varphi)}$$

$$\frac{dY_k}{dt} = \frac{1}{\rho} \left[(\dot{\omega}_k + \dot{s}_k) W_k - Y_k \sum_i \dot{s}_i W_i \right] \quad (\text{A.2})$$

A.1.3 Energy

In the constant volume reactor, the internal energy is favorable since the external boundaries of the control volume are not changed, and the work from soot volume is neglected, so formulating the energy balance based on the internal energy is preferred. The energy passes through the boundaries of the control volume via soot generation and external heat source.

$$\begin{aligned} \frac{dE}{dt} &= -\frac{dE_{soot}}{dt} + \dot{Q} \\ \Downarrow E &= m \sum Y_k e_k \\ \frac{dm}{dt} \sum_k Y_k e_k + m \sum_k \frac{dY_k}{dt} e_k + m \sum_k Y_k \frac{de_k}{dt} &= -\frac{dE_{soot}}{dt} + \dot{Q} \\ \Downarrow \text{from continuity} \\ V(1-\varphi) \sum_i \dot{s}_i W_i \sum_k Y_k e_k + m \sum_k \frac{dY_k}{dt} e_k + m \sum_k Y_k \frac{de_k}{dt} &= -\frac{dE_{soot}}{dt} + \dot{Q} \\ \Downarrow \text{from species} \\ V(1-\varphi) \sum_i \dot{s}_i W_i \sum_k Y_k e_k + m \sum_k \frac{1}{\rho} \left[(\dot{\omega}_k + \dot{s}_k) W_k - Y_k \sum_i \dot{s}_i W_i \right] e_k + m \sum_k Y_k \frac{de_k}{dt} &= -\frac{dE_{soot}}{dt} + \dot{Q} \\ \Downarrow Y_k \frac{de_k}{dt} &= Y_k c_{c,k} \frac{dT}{dt} \\ \Downarrow \sum_k Y_k c_{c,k} &= c_p \\ V(1-\varphi) \sum_i \dot{s}_i W_i \sum_k Y_k e_k + m \sum_k \frac{1}{\rho} \left[(\dot{\omega}_k + \dot{s}_k) W_k - Y_k \sum_i \dot{s}_i W_i \right] e_k + m c_v \frac{dT}{dt} &= -\frac{dE_{soot}}{dt} + \dot{Q} \\ \Downarrow \frac{dE_{soot}}{dt} &= \left(\rho_{soot} c_{v,soot} \varphi \frac{dT}{dt} - (1-\varphi) \sum_i \dot{s}_i W_i e_{soot} \right) V \\ V(1-\varphi) \sum_i \dot{s}_i W_i \sum_k Y_k e_k + m \sum_k \frac{1}{\rho} \left[(\dot{\omega}_k + \dot{s}_k) W_k - Y_k \sum_i \dot{s}_i W_i \right] e_k + m c_v \frac{dT}{dt} &= \\ - \left(\rho_{soot} c_{v,soot} \varphi \frac{dT}{dt} - (1-\varphi) \sum_i \dot{s}_i W_i e_{soot} \right) V + \dot{Q} & \end{aligned}$$

$$\Downarrow m = \rho V(1-\varphi)$$

$$\begin{aligned}
& V(1-\varphi) \sum_i \dot{s}_i W_i \sum_k Y_k e_k + V(1-\varphi) \sum_k (\dot{\omega}_k + \dot{s}_k) W_k e_k - V(1-\varphi) \sum_k Y_k e_k \sum_i \dot{s}_i W_i \\
& + \rho V(1-\varphi) c_v \frac{dT}{dt} = - \left(\rho_{soot} c_{v, soot} \varphi \frac{dT}{dt} - (1-\varphi) \sum_i \dot{s}_i W_i e_{soot} \right) V + \dot{Q} \\
& \Downarrow \text{Eliminating } V(1-\varphi) \sum_i \dot{s}_i W_i \sum_k Y_k e_k \\
& \Downarrow \times 1/V \\
& (1-\varphi) \sum_k (\dot{\omega}_k + \dot{s}_k) W_k e_k + \rho(1-\varphi) c_v \frac{dT}{dt} = - \rho_{soot} c_{v, soot} \varphi \frac{dT}{dt} + \\
& (1-\varphi) \sum_i \dot{s}_i W_i e_{soot} + \dot{Q} \\
& \Downarrow \\
& (\rho(1-\varphi) c_v + \rho_{soot} c_{v, soot} \varphi) \frac{dT}{dt} = - (1-\varphi) \sum_k e_k (\dot{\omega}_k + \dot{s}_k) W_k + (1-\varphi) \sum_i \dot{s}_i W_i e_{soot} + \frac{\dot{Q}}{V} \\
& \Downarrow \\
& \frac{dT}{dt} = \frac{1}{\rho(1-\varphi) c_v + \rho_{soot} c_{v, soot} \varphi} \left[- (1-\varphi) \sum_k e_k (\dot{\omega}_k + \dot{s}_k) W_k + (1-\varphi) \sum_i \dot{s}_i W_i e_{soot} + \frac{\dot{Q}}{V} \right] \quad (\text{A.3})
\end{aligned}$$

A.1.4 Soot Variables

The derivation of equations for soot variables can be accomplished similar to species evolution.

$$\frac{d}{dt}(m\psi) = \rho V(1-\varphi) S_\psi$$

\Downarrow

$$\frac{d}{dt}(\rho V(1-\varphi\psi)) = \rho V(1-\varphi) S_\psi$$

$\Downarrow \times 1/V$

$$\rho(1-\varphi) \frac{d\psi}{dt} + \psi \frac{d}{dt}(\rho(1-\varphi)) = \rho(1-\varphi) S_\psi$$

\Downarrow from continuity

$$\begin{aligned}
\rho(1-\varphi) \frac{d\psi}{dt} + \psi V(1-\varphi) \sum_i \dot{s}_i W_i &= \rho(1-\varphi) S_\psi \\
\Downarrow \times \frac{1}{\rho(1-\varphi)} \\
\frac{d\psi}{dt} &= S_\psi - \frac{1}{\rho} \left[\psi \sum_i \dot{s}_i W_i \right]
\end{aligned} \tag{A.4}$$

A.2 Plug Flow Reactor

A.2.1 Continuity

The gas flow that passes through the cross-section of a differential element along the flow reactor is described as:

$$\begin{aligned}
\rho u A (1-\varphi) |_{z+dz} - \rho u A (1-\varphi) |_z &= Adz(1-\varphi) \sum_i \dot{s}_i W_i \\
\Downarrow \\
\rho u (1-\varphi) A &= Adz(1-\varphi) \sum_i \dot{s}_i W_i \\
\Downarrow \\
\frac{d}{dz} (\rho u (1-\varphi)) &= (1-\varphi) \sum_i \dot{s}_i W_i
\end{aligned} \tag{A.5}$$

A.2.2 Momentum

$$\begin{aligned}
\frac{d}{dz} (\dot{m} u) &= -\frac{d}{dz} (P(1-\varphi)) - \tau_w \frac{P_c}{A} \\
\Downarrow \\
u \frac{d}{dz} (\dot{m}) + \dot{m} \frac{d}{dz} (u) &= -\frac{d}{dz} (P(1-\varphi)) - \tau_w \frac{1}{R_H} \\
\Downarrow \\
u(1-\varphi) \sum_i \dot{s}_i W_i + \rho u (1-\varphi) \frac{d}{dz} (u) &= -\frac{d}{dz} (P(1-\varphi)) - \frac{\tau_w}{R_H}
\end{aligned} \tag{A.6}$$

A.2.3 Species

$$\frac{d}{dz} (m_k) = (1 - \varphi) (\dot{\omega}_k + \dot{s}_k) W_k$$

↓

$$\frac{d}{dz} (\rho u (1 - \varphi) Y_k) = (1 - \varphi) (\dot{\omega}_k + \dot{s}_k) W_k$$

↓

$$\rho u (1 - \varphi) \frac{dY_k}{dz} + Y_k \frac{d}{dz} (\rho u (1 - \varphi)) = (1 - \varphi) (\dot{\omega}_k + \dot{s}_k) W_k$$

↓ from Equation (A.5)

$$\rho u (1 - \varphi) \frac{dY_k}{dz} + Y_k (1 - \varphi) \sum_i \dot{\omega}_i W_i = (1 - \varphi) (\dot{\omega}_k + \dot{s}_k) W_k$$

↓ × 1/(ρ(1 - φ))

$$\frac{dY_k}{dz} = \frac{1}{\rho u (1 - \varphi)} \left[(1 - \varphi) (\dot{\omega}_k + \dot{s}_k) W_k - Y_k (1 - \varphi) \sum_i \dot{s}_i W_i \right] \quad (\text{A.7})$$

A.2.4 Energy

$$\frac{d}{dz} (\rho u (1 - \varphi) h) + \frac{d}{dz} (\rho u \varphi h_{soot}) = \dot{q}'$$

↓

$$\frac{dh}{dz} (\rho u (1 - \varphi)) + h \frac{d}{dz} (\rho u (1 - \varphi)) + \frac{d}{dz} (\rho u \varphi) h_{soot} + \frac{dh_{soot}}{dz} \rho u \varphi = \dot{q}'$$

$$\downarrow h = \sum_k Y_k h_k$$

$$\rho u (1 - \varphi) \frac{d}{dz} \left(\sum_k Y_k h_k \right) + h \frac{d}{dz} (\rho u (1 - \varphi)) + \frac{d}{dz} (\rho u \varphi) h_{soot} + \frac{dh_{soot}}{dz} \rho u \varphi = \dot{q}'$$

↓

$$\rho u (1 - \varphi) \sum_k \frac{dY_k}{dz} h_k + \rho u (1 - \varphi) \sum_k \frac{dh_k}{dz} Y_k + h \frac{d}{dz} (\rho u (1 - \varphi)) + \frac{d}{dz} (\rho u \varphi) h_{soot} + \frac{dh_{soot}}{dz} \rho u \varphi = \dot{q}'$$

\Downarrow from Equation (A.5)&(A.7)

$$\rho u (1 - \varphi) \sum_k \frac{1}{\rho u} \left[(\dot{\omega}_k + \dot{s}_k) W_k - Y_k \sum_i \dot{s}_i W_i \right] h_k + \rho u (1 - \varphi) \sum_k \frac{dh_k}{dz} Y_k + h \frac{d}{dz} \left((1 - \varphi) \sum_i \dot{s}_i W_i \right) + \frac{d}{dz} (\rho u \varphi) h_{soot} + \frac{dh_{soot}}{dz} \rho u \varphi = \dot{q}'$$

$$\Downarrow \frac{dh_k}{dz} = c_{p,k} \frac{dT}{dz}$$

$$\Downarrow \sum_k Y_k c_{p,k} = c_p$$

$$\Downarrow \frac{dh_{soot}}{dz} = c_{p,soot} \frac{dT}{dz}$$

$$(1 - \varphi) \sum_k \left[(\dot{\omega}_k + \dot{s}_k) W_k - Y_k \sum_i \dot{s}_i W_i \right] h_k + \rho u (1 - \varphi) c_p \frac{dT}{dz} + h (1 - \varphi) \sum_i \dot{s}_i W_i + \frac{d}{dz} (\rho u \varphi) h_{soot} + c_{p,soot} \frac{dT}{dz} \rho u \varphi = \dot{q}'$$

\Downarrow

$$(1 - \varphi) \sum_k [(\dot{\omega}_k + \dot{s}_k) W_k] h_k + \rho u (1 - \varphi) c_p \frac{dT}{dz} - (1 - \varphi) \sum_i \dot{s}_i W_i h_{soot} + c_{p,soot} \frac{dT}{dz} \rho u \varphi = \dot{q}'$$

\Downarrow

$$[\rho u (1 - \varphi) c_p + \rho u \varphi c_{p,soot}] \frac{dT}{dz} + (1 - \varphi) \sum_k [(\dot{\omega}_k + \dot{s}_k) W_k] h_k - (1 - \varphi) \sum_i \dot{s}_i W_i h_{soot} = \dot{q}'$$

\Downarrow

$$\frac{dT}{dz} = \frac{1}{\rho u (1 - \varphi) c_p + \rho u \varphi c_{p,soot}} \left[- (1 - \varphi) \sum_k (\dot{\omega}_k + \dot{s}_k) W_k h_k + (1 - \varphi) \sum_i \dot{s}_i W_i h_{soot} + \dot{q}' \right]$$

A.3 Perfectly Stirred Reactor

A.3.1 Continuity

The mass conservation for the partially stirred reactor can be written as:

$$\frac{dm}{dt} = \dot{m}_{in} - \dot{m}_{out} + V (1 - \varphi) \sum_i \dot{s}_i W_i \quad (\text{A.8})$$

A.3.2 Species

$$\frac{d}{dt} (m_k) = \dot{m}_{in} Y_k^* - \dot{m}_{out} Y_k + V (1 - \varphi) (\dot{\omega}_k + \dot{s}_k) W_k$$

$$\Downarrow m_k = m Y_k$$

$$Y_m \frac{dm}{dt} + m (Y_k) = \dot{m}_{in} Y_k^* - \dot{m}_{out} Y_k + V (1 - \varphi) (\dot{\omega}_k + \dot{s}_k) W_k$$

\Downarrow from Equation A.8

$$\left(\dot{m}_{in} - \dot{m}_{out} + V (1 - \varphi) \sum_i \dot{s}_i W_i \right) Y_k + \frac{dY_k}{dt} m = \dot{m}_{in} Y_k^* - \dot{m}_{out} Y_k + V (1 - \varphi) (\dot{\omega}_k + \dot{s}_k) W_k$$

$$\Downarrow$$

$$V (1 - \varphi) Y_k \sum_i \dot{s}_i W_i + \frac{dY_k}{dt} m = \dot{m}_{in} (Y_k^* - Y_k) + V (1 - \varphi) (\dot{\omega}_k + \dot{s}_k) W_k$$

$$\Downarrow$$

$$\frac{dY_k}{dt} \rho V (1 - \varphi) = \dot{m}_{in} (Y_k^* - Y_k) + V (1 - \varphi) (\dot{\omega}_k + \dot{s}_k) W_k - V (1 - \varphi) Y_k \sum_i \dot{s}_i W_i$$

$$\Downarrow$$

$$\frac{dY_k}{dt} = \frac{\dot{m}_{in}}{\rho V (1 - \varphi)} (Y_k^* - Y_k) + \frac{1}{\rho} (\dot{\omega}_k + \dot{s}_k) W_k - \frac{1}{\rho} Y_k \sum_i \dot{s}_i W_i \quad (\text{A.9})$$

A.3.3 Energy

$$\frac{dH}{dt} = \dot{m}_{in} h^* - \dot{m}_{out} h - \frac{dH_{soot}}{dt} + \dot{Q}$$

$$\Downarrow H = mh$$

$$\frac{dm}{dt} h + m \frac{dh}{dt} = \dot{m}_{in} h^* - \dot{m}_{out} h - \frac{dH_{soot}}{dt} + \dot{Q}$$

\Downarrow from Equation A.8

$$\left(\dot{m}_{in} - \dot{m}_{out} + V (1 - \varphi) \sum_i \dot{s}_i W_i \right) h + m \frac{dh}{dt} = \dot{m}_{in} h^* - \dot{m}_{out} h - \frac{dH_{soot}}{dt} + \dot{Q}$$

$$\Downarrow$$

$$V(1-\varphi)h \sum_i \dot{s}_i W_i + m \frac{dh}{dt} = \dot{m}_{in}(h^* - h) - \frac{dH_{soot}}{dt} + \dot{Q}$$

↓

$$m \frac{dh}{dt} = \dot{m}_{in}(h^* - h) - V(1-\varphi)h \sum_i \dot{s}_i W_i - \frac{dH_{soot}}{dt} + \dot{Q}$$

$$\Downarrow h = \sum Y_k h_k$$

$$m \sum \frac{dY_k}{dt} h_k + m \sum \frac{dh_k}{dt} Y_k = \dot{m}_{in}(h^* - h) - V(1-\varphi)h \sum_i \dot{s}_i W_i - \frac{dH_{soot}}{dt} + \dot{Q}$$

↓ from Equation A.9

$$m \sum \left(\frac{\dot{m}_{in}}{\rho V(1-\varphi)} (Y_k^* - Y_k) + \frac{1}{\rho} (\dot{\omega}_k + \dot{s}_k) W_k - \frac{1}{\rho} Y_k \sum_i \dot{s}_i W_i \right) h_k + m \sum c_{p,k} \frac{dT}{dt} Y_k = \\ \dot{m}_{in}(h^* - h) - V(1-\varphi)h \sum_i \dot{s}_i W_i - \frac{dH_{soot}}{dt} + \dot{Q}$$

$$\Downarrow m = \rho V(1-\varphi)$$

$$\dot{m}_{in} \sum (Y_k^* - Y_k) h_k + V(1-\varphi) \sum (\dot{\omega}_k + \dot{s}_k) W_k h_k + mc_p \frac{dT}{dt} = \dot{m}_{in}(h^* - h) - \frac{dH_{soot}}{dt} + \dot{Q}$$

↓

$$\dot{m}_{in} \sum (Y_k^* - Y_k) h_k + V(1-\varphi) \sum (\dot{\omega}_k + \dot{s}_k) W_k h_k + mc_p \frac{dT}{dt} = \dot{m}_{in}(h^* - h) \\ - \left(\rho_{soot} c_{p,soot} \varphi V \frac{dT}{dt} - (1-\varphi) V \sum_i \dot{s}_i W_i h_{soot} \right) + \dot{Q}$$

↓

$$\dot{m}_{in} \sum (Y_k^* - Y_k) h_k + V(1-\varphi) \sum (\dot{\omega}_k + \dot{s}_k) W_k h_k + mc_p \frac{dT}{dt} = \dot{m}_{in}(h^* - h) \\ - \left(\rho_{soot} c_{p,soot} \varphi V \frac{dT}{dt} - (1-\varphi) V \sum_i \dot{s}_i W_i h_{soot} \right) + \dot{Q}$$

$$\Downarrow m = \rho V(1-\varphi)$$

$$\Downarrow \times 1/V$$

$$\begin{aligned}
& \dot{m}_{in} \sum (Y_k^* - Y_k) h_k + V (1 - \varphi) \sum (\dot{\omega}_k + \dot{s}_k) W_k h_k + \rho V (1 - \varphi) c_p \frac{dT}{dt} = \\
& \dot{m}_{in} (h^* - h) - \left(\rho_{soot} c_{p,soot} \varphi V \frac{dT}{dt} - (1 - \varphi) V \sum_i \dot{s}_i W_i h_{soot} \right) + \dot{Q} \\
& \Downarrow \\
& (\rho (1 - \varphi) c_p + \rho_{soot} c_{p,soot} \varphi) \frac{dT}{dt} = \frac{\dot{m}_{in}}{V} (h^* - h) - \frac{\dot{m}_{in}}{V} \sum (Y_k^* - Y_k) h_k \\
& - (1 - \varphi) \sum (\dot{\omega}_k + \dot{s}_k) W_k h_k + (1 - \varphi) \sum_i \dot{s}_i W_i h_{soot} + \frac{\dot{Q}}{V} \\
& \Downarrow \\
& \frac{dT}{dt} = \frac{1}{\rho (1 - \varphi) c_p + \rho_{soot} c_{p,soot} \varphi} \left[\frac{\dot{m}_{in}}{V} (h^* - h) - \frac{\dot{m}_{in}}{V} \sum (Y_k^* - Y_k) h_k - (1 - \varphi) \sum (\dot{\omega}_k + \dot{s}_k) W_k h_k \right. \\
& \quad \left. + (1 - \varphi) \sum_i \dot{s}_i W_i h_{soot} + \frac{\dot{Q}}{V} \right] \tag{A.10}
\end{aligned}$$

Appendix B

Appendix: Additional Results

B.1 Methane pyrolysis data from Hanson Research Group

B.1.1 30% CH_4 dataset

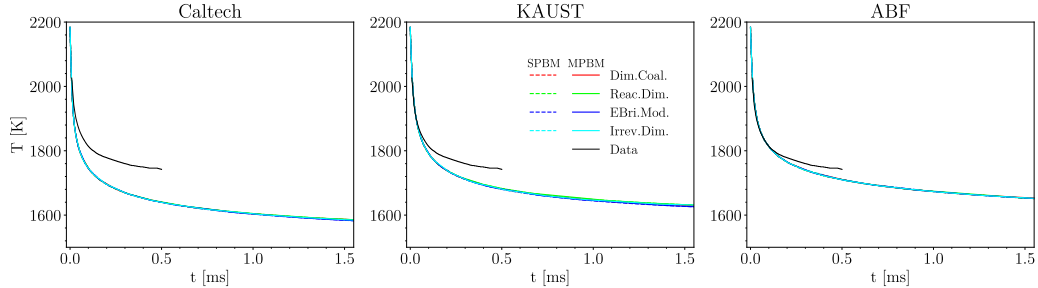


Figure B.1: The time history of temperature of 30% CH_4 pyrolysis at $T=2184$ K and $P=3.62$ atm using Caltech, KAUST, and ABF mechanism and different PAH growth and particle dynamics models compared with the simulation results reported by Hanson Research Group

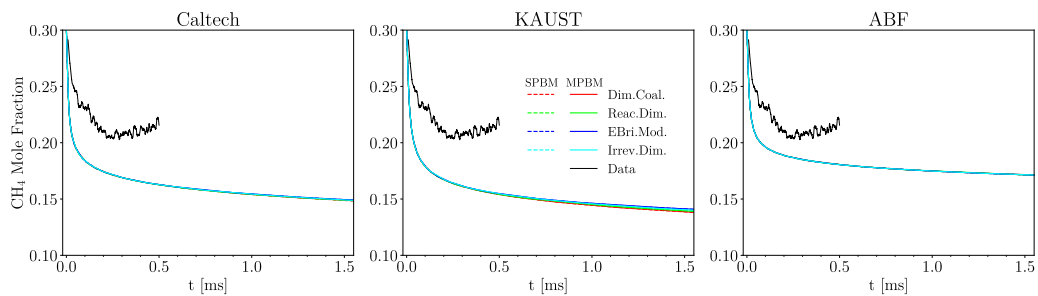


Figure B.2: The time history of CH_4 mole fraction of 30% CH_4 pyrolysis at $T=2184$ K and $P=3.62$ atm using Caltech, KAUST, and ABF mechanism and different PAH growth and particle dynamics models compared with laser diagnostic data

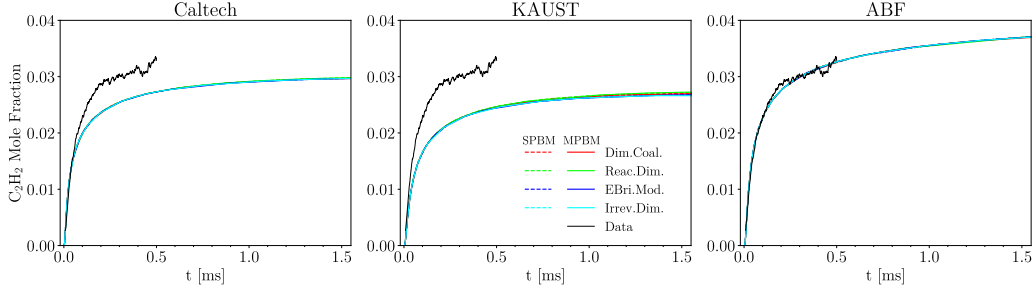


Figure B.3: The time history of C_2H_2 mole fraction of 30% CH_4 pyrolysis at $T=2184$ K and $P=3.62$ atm using Caltech, KAUST, and ABF mechanism and different PAH growth and particle dynamics models compared with laser diagnostic data

B.2 Methane pyrolysis data of Agafonov et al. [1]

The pyrolysis of 5% and 10% CH_4 diluted with Ar is investigated for the post-shock temperature range of 1800-3000 K and the pressure range of 4.7-7.1 bar. We assume the pressure linearly increase by temperature across the simulation cases. The obtained soot yields were compared with the soot yield measured by Agafonov et al. [1] using a dual-beam absorption–emission technique. Agafonov et al. [1] reported yield $\times E(m)$ at $\lambda=632$ nm, and yield data was retrieved using $E(m)=0.37$ suggested therein.

Figure B.4 depicts soot yield (SY) at $t=1.5$ ms for 5% and 10% CH_4 over the temperature range of 1800-3000 K using MPBM and SPBM and different inception model and Caltech [169] mechanism. Note that, the simulations were also performed using ABF [59] and KAUST [160] mechanisms, and the results were included in Appendix ***. The soot yield predictions exhibit a close agreement with measurements [1] considering the uncertainties in residence time from experiments. The model also successfully captures the bell-shape dependence of soot yield on temperature that has been observed in a variety of hydrocarbons in shock tube [177, 178]. The particle dynamics model has minimal effect on the predicted soot yield. In the vicinity of peak soot yield, SPBM results in slightly lower yield than MPBM, but they are indistinguishable in the rest of the temperature range.

In %5 CH_4 , the SY peak temperature obtained from the model is slightly shifted towards higher temperatures ($2300 \text{ K} < T_{peak} < 2400 \text{ K}$) compared to the measurements $T_{peak}=2200$ K. There are noticeable differences in the behavior of PAH growth model depending on the shock-tube initial temperature. When $T < 2100$ K, Reactive Dimerization and EBridge Formation have the highest and lowest soot yield, respectively with Dimer Coalescence predicting soot yields that always falls between Reactive and Irreversible Dimerization. However, The soot yield of EBridge Formation rapidly rises with temperature and exceeds that of Reactive Dimerization and stays higher for the rest of temperature range.

The SY noticeably increases for higher initial CH_4 mole fraction of %10 because more PAH and C_2H_2 are formed leading to stronger carbon conversion rate to soot via inception and surface growth. The peak SY obtained from the model occurs in a higher temperature range 2600-2700 K compared to %5 CH_4 . Soot yield trends can be better understood by examining carbon mass fraction of species directly contributing to soot mass. Figure B.5 depicts the bell-shape distribution of the carbon mass fraction of soot precursors (A2, A2R5, A3, and A4) over the studied temperature range. In low ($T=1800$ K) and high ($T=2300$ K) end of distribution, a low amount of precursors are formed resulting in low inception rates, particle number concentration and surface growth sites that reduces the soot yield. Additionally, %10 CH_4 has a wider spread with peaks at higher temperature compared to %5 CH_4 which explains the shift in peak yield temperature in Figure B.4. The effect of particle dynamics model is only noticeable in Reactive Dimerization where SPBM results in higher precursor CMF (lower consumption) due to its lower PAH adsorption rates.

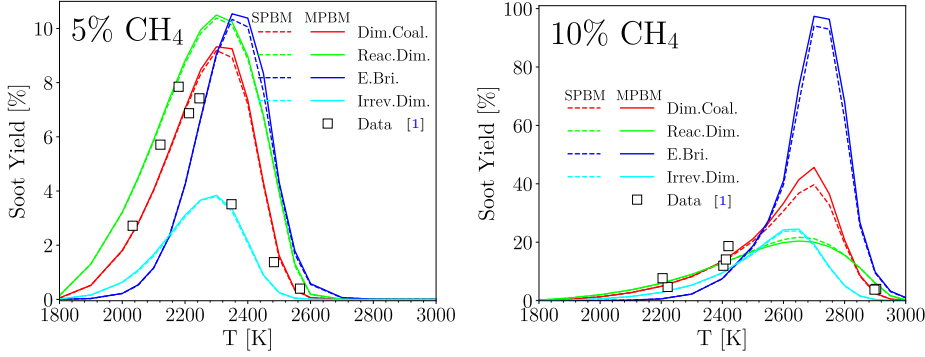


Figure B.4: The temperature dependence of soot yield during pyrolysis of 5% CH₄-Ar (left pane) and 10% CH₄-Ar (right pane) at P = 4.5–6.7 bar obtained using Caltech mechanism and different inception models compared with measurements at 1.5ms [1] where the absorption function of E(m)=0.37 is used to estimate soot yield.

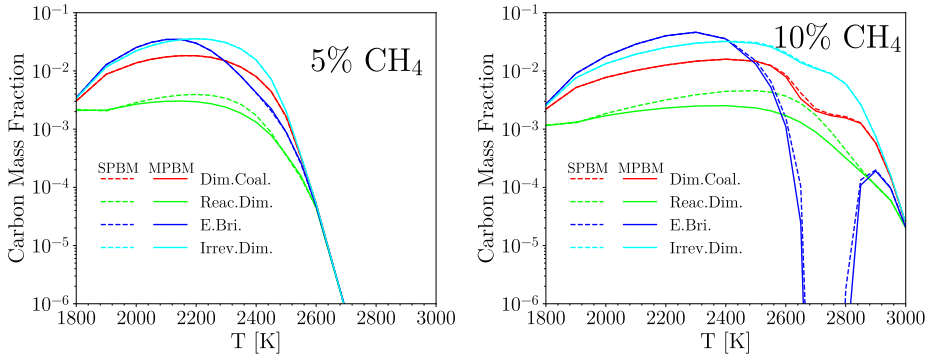


Figure B.5: The temperature dependence of carbon mass fraction of soot precursors (A2, A2R5, A3, and A4) combined during pyrolysis of 5% CH₄-Ar (left pane) and 10% CH₄-Ar (right pane) at P = 4.5–6.7 bar obtained using Caltech mechanism and different inception models at t=1.5 ms

EBridge Formation exhibits a similar behavior in %10 CH₄ simulations where it starts with the lowest SY at T<2500 K and then quickly increases reaching its peak at 100% which is significantly larger than other PAH growth models. The remarkable drop in carbon mass fraction of precursors with EBridge Formation corresponds to %100 yield meaning that all gaseous carbon including the precursors are directed towards soot particles. The higher precursor CMF with Irreversible Dimerization near the peak yield temperature region (2200-2400 K for %5 CH₄ and 2600-2800 K for %10 CH₄) indicates less consumption of precursors via inception and PAH adsorption.

Figure B.6 shows the CMF of C₂H₂ that has an overall increasing trend in the temperature range, but it reaches a plateau for %5 CH₄. There is also a remarkable drop in C₂H₂ CMF in 2600-2800 K due to strong mass growth rate of soot particles that drains C₂H₂ from the gas mixture leading to high soot yield $\approx 100\%$.

Although soot yield, and precursor and acetylene CMF are not sensitive to particle dynamics model, there is a significant difference in agglomerate morphology between SPBM and MPBM predictions. Fig. B.7 shows the average number of primary particles per agglomerate, which is larger for SPBM by the maximum factor of 5 for EBridge Formation and Dimer Coalescence in 10% CH₄. SPBM predicts larger agglomerates due to accounting for polydispersity of particles that results in higher overall collision rate and faster growth by coagulation. n_p follows a bell-shape trend similar to soot yield (Fig. B.4). The n_p values and the difference between the particle dynamics models reaches their maximum in 2200-2400 K for %5 CH₄ and 2600-2800 K for %10 CH₄ because of a stronger inception flux leading to larger number concentration of particles and higher coagulation

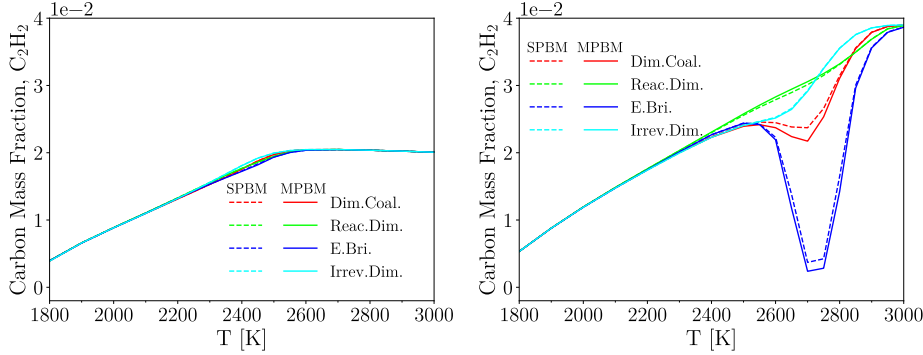


Figure B.6: The temperature dependence of carbon mass fraction of C_2H_2 during pyrolysis of 5% CH_4 -Ar (left pane) and 10% CH_4 -Ar (right pane) at $P = 4.5\text{--}6.7$ bar obtained using Caltech mechanism and different inception models at $t=1.5$ ms

rate. n_p is larger for Dimer Coalescence and EBridge Formation reaching the maximum of nearly 100 and 1000 in %5 and %10 CH_4 , respectively using SPBM. The effect of particle dynamics is minimum for Reactive and Irreversible Dimerization at 5% CH_4 over the whole temperature range.

Fig.B.8 shows the standard geometric deviation of mobility diameter, σ_g obtained by SPBM that reaches the maximum of 5 and 10 for %5 and %10 CH_4 , respectively indicating a significant degree of polydispersity in the generated particles at $t=1.5$ ms.

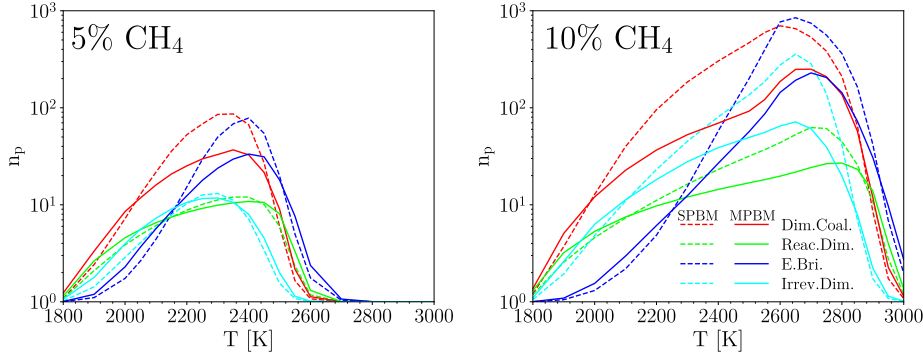


Figure B.7: The temperature dependence of average number of primary particle per agglomerate, n_p during pyrolysis of 5% CH_4 -Ar (left pane) and 10% CH_4 -Ar (right pane) at $P = 4.5\text{--}6.7$ bar obtained using Caltech mechanism and different inception models at $t=1.5$ ms

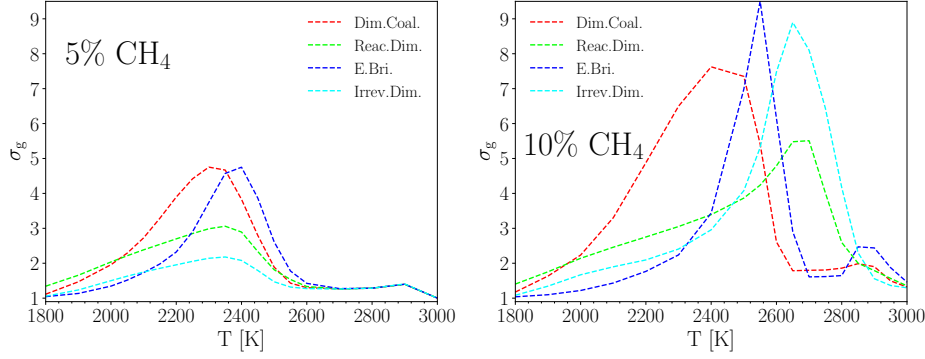


Figure B.8: The time variation of standard geometric deviation of mobility diameter, σ_g during pyrolysis of 5% CH₄-Ar (left pane) and 10% CH₄-Ar (right pane) at P = 4.5–6.7 bar obtained using Caltech mechanism and different inception models at t=1.5 ms

The σ_g values from the SMPS measurements of soot particles at $t \approx 45$ ms in a benchmark burner-stabilized premixed are close to 1.1, which is significantly lower than values observed here. So, the evolution of σ_g in the studied shock tube is examined in an extended time frame up to 4 msf for 10% CH₄ at T=2500 and 2700 K. As shown in Fig.B.9, for all PAH growth models σ_g rises in the beginning due to simultaneous inception and coagulation that increases polydispersity and rapidly drops and approaches 1.5 before t=3ms when coagulation becomes dominant and inception weaken due to consumption of precursors by PAH adsorption and HACA.

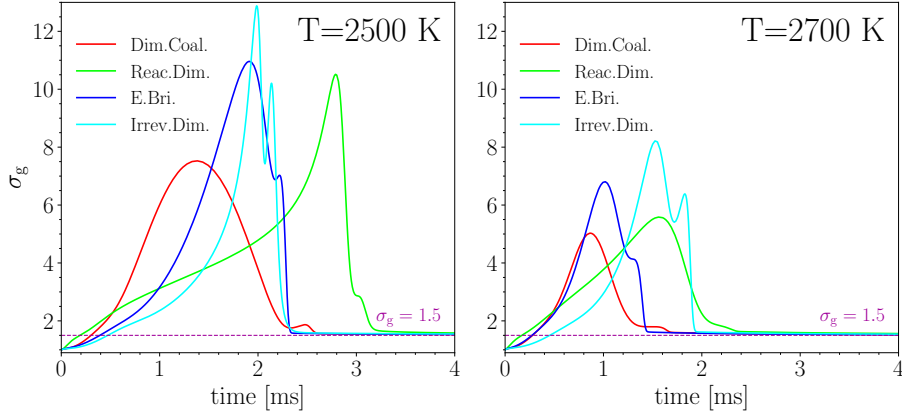


Figure B.9: The temperature dependence of standard geometric deviation of mobility diameter, σ_g during pyrolysis of 10% CH₄-Ar at T=2500 K (left pane) and T=2700 K (right pane)